Structure and Dynamics of Various Micellar Systems Composed of Low Molar Mass and Polymer Surfactants

A Doctoral Thesis

by

Ken Morishima

Submitted to
the Graduate School of Science, Osaka University

February, 2015

Acknowledgement

This thesis work was carried out from 2009 to 2015 under direction of Professors Takahiro Sato and Tadashi Inoue at the Department of Macromolecular Science, Graduate School of Science, Osaka University. First, I would like to express my sincerest gratitude to Professors Takahiro Sato and Tadashi Inoue for their kindest guidance, valuable suggestions and discussions during this work. I also would like to extend my gratitude to Associate Professors Akihito Hashidzume, Ken Terao, Osamu Urakawa (Osaka University), and Professor Toshiyuki Shikata (Tokyo University of Agriculture and Technology) for their helpful advices and valuable discussions.

I would like to express my deep gratitude to Professor Katsumi Imada (Osaka University) for his careful review and valuable comments.

I am grateful to Mr. Rintaro Takahashi in the Sato laboratory for SAXS measurements.

I thank all members of both Sato and Inoue laboratories for their helpful advices and their friendships.

Finally, I express my sincerest thanks to my family members and friends for their constant support and warmest encouragements.

February, 2015

守島健

Ken Morishima

Contents

Chapter I.

General Introduction

I-1. Various Micelles and Their Size Distributions.

Surfactants or amphiphilic molecules have hydrophilic and hydrophobic parts. Since hydrophobic parts associate by their hydrophobic interactions in an aqueous solution, surfactants form various types of micelles spontaneously, for example, (a) spherical micelles, (b) threadlike micelles, and (c) bilayer disklike micelles, as illustrated in Scheme I-1.

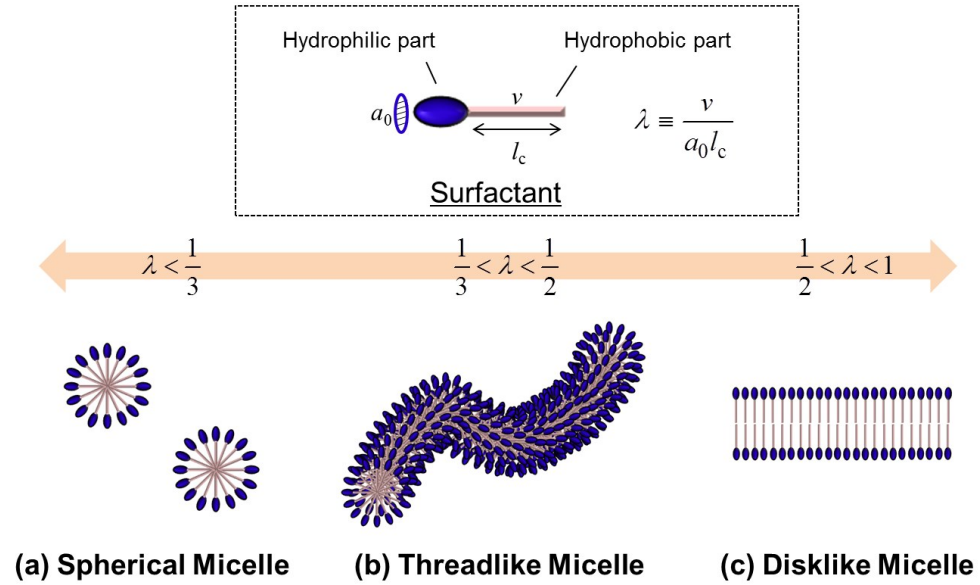

Scheme I-1. Various types of micelles formed by surfactants.

Surfactants are utilized as detergents, surface modifiers, emulsifiers, colloid stabilizers, and so on in various fields of industry. Recently, in the field of nano-technology, researchers are interested in the nanometer-sized hydrophobic domain of micelles (or the hydrophilic domain of reverse micelles) due to its potential applications as nano-carriers and nano-reactors. For these applications, precise characterizations of the micelles are prerequisite, because functions of the micelles strongly depend on their domain size and also morphology.

The morphology of the micelle is determined by the geometry of the surfactant

molecule. As shown in Scheme I-1, the geometry of the surfactant molecule is specified by the length l_c and volume v of the hydrophobic part as well as the cross section a_0 of the hydrophilic part. Israelachvili et al.[1] proposed to argue the micellar morphology in terms of the shape factor λ defined by

$$\lambda \equiv \frac{v}{a_0 l_c} \tag{I-1}$$

According to them, surfactants form spherical, threadlike, and disklike micelles at $\lambda < 1/3$, $1/3 < \lambda < 1/2$, and $1/2 < \lambda < 1$, respectively, and when $\lambda > 1$, the reverse micelle is formed.

The size of the micelle is determined thermodynamically. Let us consider an association-dissociation equilibrium in a micellar solution of the low molar mass amphiphile R, given by

$$\mathrm{R} \overset{K_2}{\rightleftarrows} \frac{1}{2}\mathrm{R}_2 \overset{K_3}{\rightleftarrows} \frac{1}{3}\mathrm{R}_3 \cdots \overset{K_m}{\rightleftarrows} \frac{1}{m}\mathrm{R}_m \cdots \tag{I-2}$$

where R_m represents m-mer, m is its aggregation number, and K_m is the aggregation constant for m-mer. Under the association-dissociation equilibrium, chemical potentials μ_1 and μ_m for R and R_m respectively must obey the following equation.

$$m\mu_1 = \mu_m \tag{I-3}$$

If the surfactant solution is dilute enough, it can be regarded as an ideal solution, and the μ_1 and μ_m are given by

$$\frac{\mu_1}{k_\mathrm{B}T} = \frac{\mu_1^\circ}{k_\mathrm{B}T} + \ln \phi_1 \quad , \qquad \frac{\mu_m}{k_\mathrm{B}T} = \frac{\mu_m^\circ}{k_\mathrm{B}T} + \ln\left(\frac{\phi_m}{m}\right) \tag{I-4}$$

Here, k_B and T are the Boltzmann constant and absolute temperature, respectively, μ_1° and μ_m° are the standard chemical potentials (or the internal free energies), and the ϕ_1 and ϕ_m are the volume fractions for R and R_m, respectively. Combining eqs I-3 and I-4, the K_m defined in terms of the volume fraction is given by.

$$K_m \equiv \frac{\phi_m}{\phi_1^m} = m\exp(-\Delta_m) \tag{I-5}$$

where

$$\Delta_m \equiv \frac{\mu_m^\circ - m\mu_1^\circ}{k_B T} \tag{I-6}$$

Therefore, the aggregation number distribution is determined by the m dependence of Δ_m, which means the change in the standard chemical potential by the micellization. Since the m dependence of Δ_m is governed by the morphology of the micelle, the aggregation number distribution strongly depends on the morphology.

The sum of ϕ_1 and ϕ_m is the total volume fraction ϕ of the surfactant added to the solution. From eq I-5, when m is a large number, and ϕ is low enough, ϕ_m ($\propto \phi_1^m$) is essentially zero, so that the surfactant almost exists as the unimer R, but with increasing ϕ, ϕ_m increases rapidly. The critical micelle concentration (CMC) ϕ^*, where the micelle R_m starts forming in the solution, is given by

$$\phi^* \equiv K_m^{-1/(m-1)} \tag{I-7}$$

The increase of ϕ_m with ϕ becomes sharper for larger m.

I-1-1. Spherical Micelle.

The Δ_m for a spherical micelle is given by[2]

$$\Delta_m = -\lambda m + \sigma m^2 + 4\pi R_c^2 \gamma \tag{I-8}$$

where λ and σ are the free energy coefficients, R_c is the radius of the micelle, and γ is the interfacial tension between the micelle and the solvent. The first term on the right hand side of eq I-8 means the free energy gain when m hydrophobes enter the hydrophobic core of the micelle, the second term means the free energy penalty due to the interaction among hydrophilic parts of the amphiphilic molecules, and the third term means the interfacial free energy between the micelle and the solvent. Using eq I-8, the aggregation number distribution is given by

$$\phi_m \propto m \exp\left[-\sigma(m-m_0)^2\right] \tag{I-9}$$

where m_0 is the optimum aggregation number defined by

$$m_0 \equiv -\frac{\lambda + \ln \phi_1}{2\sigma} \tag{I-10}$$

Furthermore, if the total volume fraction ϕ is much higher than the CMC, the number and weight-average aggregation numbers m_n and m_w are calculated by

$$\sqrt{\sigma} m_n = \sqrt{\sigma} m_0 + \frac{1}{\sqrt{\pi}} \quad , \quad \sqrt{\sigma} m_w = \frac{\sigma m_0^2 + \left(2/\sqrt{\pi}\right)\sqrt{\sigma} m_0 + 1/2}{\sqrt{\sigma} m_0 + 1/\sqrt{\pi}} \tag{I-11}$$

From m_w/m_n calculated by eq I-11, it turns out that the dispersity in m is very sharp, if m_0 is sufficiently large (m_w/m_n = 1.07, 1.01, 1.006 when $\sqrt{\sigma} m_0$ = 1, 3, and 5, respectively), and the optimum aggregation number m_0 is independent of the surfactant concentration. This narrow distribution and concentration independence make the characterization of the spherical micelle easier in solutions with the surfactant concentration much higher than the CMC.

I-1-2. Threadlike Micelle.

The m dependence of Δ_m for a threadlike micelle (cylinder micelle) is given by[2]

$$\Delta_m = -g(m-m_e) - g_e m_e = -gm + m_e(g-g_e) \tag{I-12}$$

where g and g_e are the excess free energy coefficients of the center and end parts of the cylinder, respectively, and m_e is the number of surfactant molecules in the end part. The aggregation number distribution calculated by using eq I-12 is represented as

$$\phi_m = m e^{-g_e} \left(\phi_1 e^{g_e}\right)^m . \tag{I-13}$$

This corresponds to the most probable distribution, originally proposed for polymers obtained by the ideal polycondensation. When $\phi_1 e^{g_e}$ approaches unity, the long threadlike micelle is formed.

Using eq I-13, the m_n and m_w are given by

$$m_{\mathrm{n}} = \frac{1}{1-\phi_1 e^{g_{\mathrm{e}}}} \quad , \quad m_{\mathrm{w}} = \frac{1+\phi_1 e^{g_{\mathrm{e}}}}{1-\phi_1 e^{g_{\mathrm{e}}}} \tag{I-14}$$

and the volume fraction ϕ of surfactant in the solution is also calculated by

$$\phi = \sum_{m=1}^{\infty} \phi_m = \frac{\phi_1}{\left(1-\phi_1 e^{g_{\mathrm{e}}}\right)^2} \tag{I-15}$$

Therefore, when the threadlike micelle is long enough ($\phi_1 e^{g_{\mathrm{e}}} \approx 1$), $m_{\mathrm{w}} = 2m_{\mathrm{n}} \propto \phi^{0.5}$ is satisfied. The distribution of the threadlike micelle is broader than that of spherical micelles as shown in Figure I-1. It is important to consider the distribution and concentration dependence of the micelle size, when one characterizes the threadlike micelle in solution.

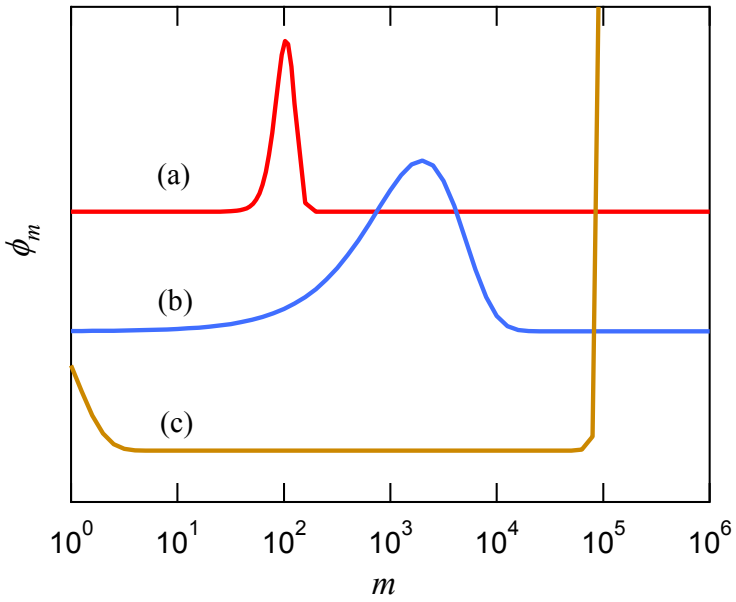

Figure I-1. Aggregation number distribution for various aggregates (a) spherical micelle, (b) threadlike micelle, and (c) disklike micelle.

I-1-3. Disk-like Micelle.

The m dependence of Δ_m for a disk-like micelle is respectively given by[2]

$$\Delta_m = -g'\left(m - m_{\mathrm{e}}\right) - g'_{\mathrm{e}} m_{\mathrm{e}} = -g'm + \left(g' - g'_{\mathrm{e}}\right)\kappa\sqrt{m} \tag{I-16}$$

where g' and g'_e are the excess free energy coefficients of the center and edge parts of the disk-like micelle, respectively, and m_e is the number of surfactant molecules in the edge part, which is related to m by $m_e = \kappa m^{1/2}$ with the proportional constant κ. The above equation, however, does not provide a stable aggregation number distribution, in contrast with the case of the spherical and threadlike micelles. As seen in Figure I-1, the distribution function of the disklike micelle diverges at high m in a solution where the disklike micelle grows sufficiently. Although this thesis does not deal with this disklike micelle, one must be careful to characterize this micelle.

I-1-4. Flower Micelle.

Polymer surfactants can possess many hydrophobes in a molecule (cf. Scheme I-2), and are often referred to as "polysoaps." Borisov and Halperin[3-5] argued theoretically the morphology of polysoaps in aqueous media, and proposed the flower micelle model illustrated in Scheme I-2.

The size distribution of the flower micelle may resemble that for the spherical micelle, because both micelles have a single spherical hydrophobic core. Although the effect of loop chains has not quantitatively discussed yet, the size distribution of the flower micelle should be narrow and independent of the copolymer concentration, if the concentration is much higher than the CMC. Since the CMC of polymer surfactants is usually very low due to the connection of hydrophobes to the polymer chain, the characterization of the flower micelle can be made without considering the distribution and concentration dependence of the aggregation number.

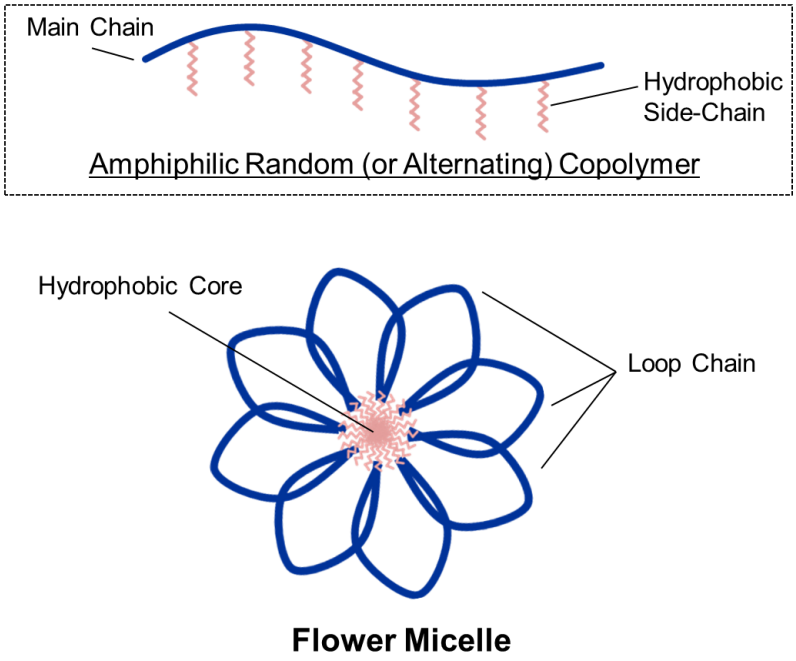

Scheme I-2. Flower micelle composed of amphiphilic random or alternating copolymers.

I-2. Structure and Dynamics of Micelles.

As mentioned above, precise characterizations of micelles are basically important to control various functions of the micelles. Debye[6,7] first proposed to characterize spherical micelles in solution by light scattering. Recently, various microscopic techniques (e.g., electron, atomic force, and scanning tunneling microscopies) are more popular to characterize micelles. However, these techniques need to adsorb on substrates or to quench micelles, and these treatments may change the micellar structure. Moreover, the dynamics of micelles in solution cannot be studied by microscopic techniques. Therefore, *in situ* measurements, like various scattering methods, are still important for precise characterization of micelles in solution.

I-2-1. Spherical Micelles Composed of Low Molar Mass Surfactants.

As already mentioned by Debye[7], special cares are necessary to analyze light

scattering data for micellar solutions near the CMC. He proposed the well-known Debye plot to estimate the molar mass of the spherical micelle. Many low molar mass ionic surfactants which have a long alkyl group and a ionic group, e.g., sodium dodecyl sulfate (SDS), dodecyl trimethyl ammonium bromide (CTAB), and dodecyl trimethyl pyridinium chrolide (DPC), are known to have a CMC near the concentration region where light scattering measurements are carried out. Therefore, one must take the association-dissociation equilibrium into account at analyzing light scattering data.

When the concentration of spherical micellar solutions approaches the CMC, anomalously strong light scattering was often observed.[8-11] According to the result of dynamic light scattering (DLS) measurement for these solutions, two scattering components (a small and a huge component) exist in the solution.[12] The anomalous scattering is owing to a tiny amount of huge aggregates being composed of a hydrophobic impurity. In this case, the weaker light scattering intensity from the major micelle component is difficult to be analyzed. In particular, this anomalous light scattering is significant for hydrophobe-uptake micelles.[10,11]

I-2-2. Flower Micelles Composed of Polymer Surfactants.

Amphiphilic alternating and random copolymers synthesized from hydrophobic and hydrophilic monomers are typical polymer surfactants, and expected to form flower micelles in aqueous media as shown in Scheme I-2. These copolymers have many hydrophobic groups in a molecule, and the hydrophobic core is formed by hydrophobic groups belonging to the same and different polymer chains.[13]

Recently, Kawata et al. and Ueda et al. reported that amphiphilic random and alternating copolymers with dodecyl hydrophobes and vinyl polymer backbone form the flower micelle with minimum-size loops in aqueous solution when the degree of polymerization is less than ca. 300.[14,15] According to this model, not all dodecyl groups

attaching to the copolymer chain are included into the hydrophobic core of the flower micelle, which was not considered for the original flower micelle model proposed theoretically by Borisov and Halperin.[3]

Tominaga et al.[16] performed molecular dynamics simulation for the micelle formed by an amphiphilic random copolymer chain with dodecyl hydrophobes and sulfonate groups on the vinyl polymer backbone in aqueous solution (cf. Figure I-2(a)). From the simulation result, they obtained the radial distribution functions of dodecyl carbon, main-chain carbon, and sulfonate sulfur atoms. While only dodecyl carbon atoms exist in a central domain of the micelle which can be regarded as the hydrophobic core, there is a domain outside the core where dodecyl carbon, main-chain carbon, and sulfonate sulfur atoms are intermingled ($R_{core} < r < R_{micelle}$ in Figure I-2(b)). This intermingled domain may correspond to the dodecyl groups not included in the hydrophobic core of the flower micelle, mentioned above.

Investigation of hydrophobe-uptake behavior is important in terms of applications for nano-carriers and nano-reactors. Although Borisov and Halperin[5] investigated theoretically this behavior of polysoaps, there are little experimental investigations on the hydrophobe uptake behavior, especially on the structure of the hydrophobe uptake flower micelle. Since the structure of this micellar system is expected to be more complex than that of the flower micelle formed only by polysoaps, we need a new method for charactering the micellar structure.

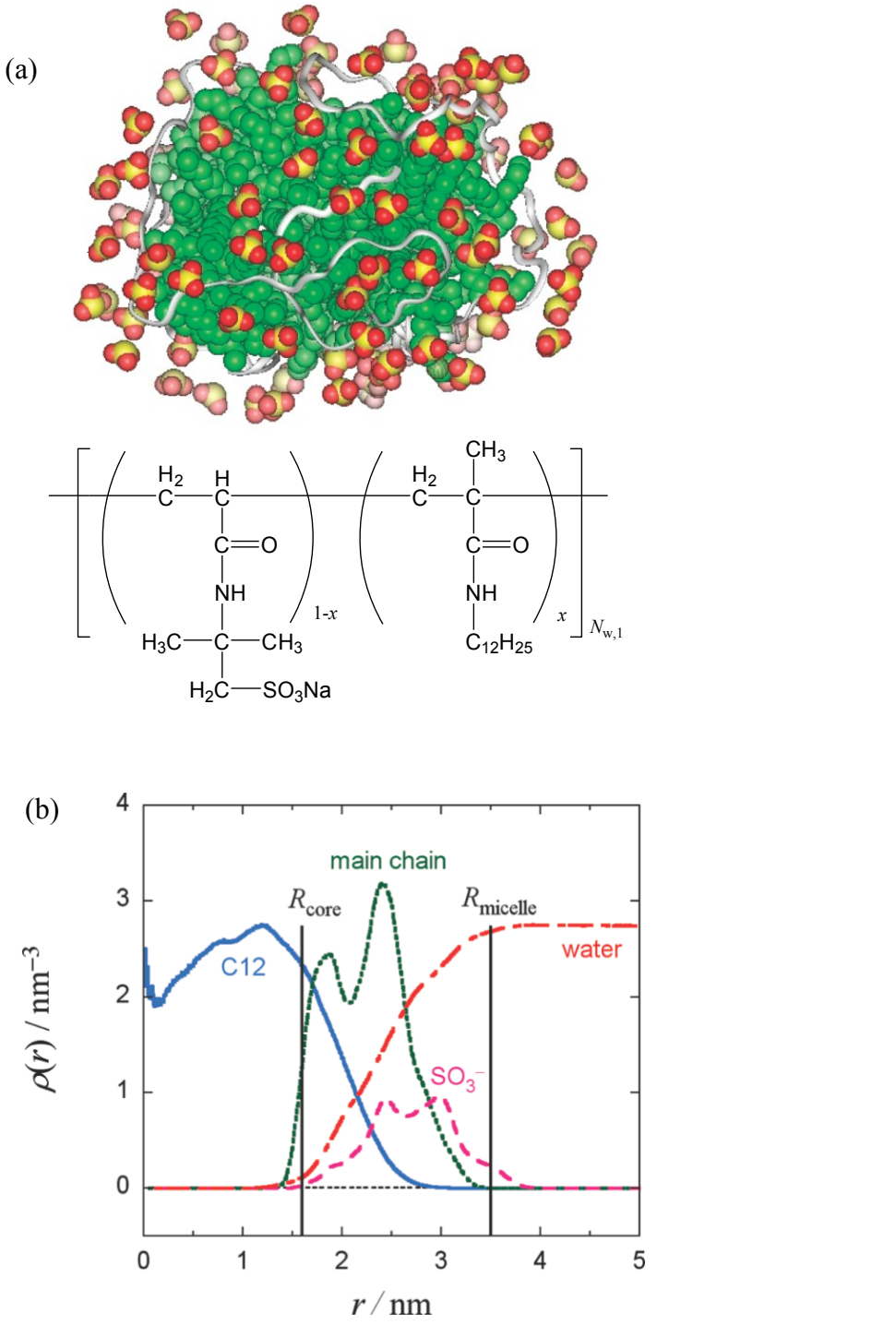

Figure I-2. (a) Snapshot of the flower micelle and Chemical structure of amphiphilic random copolymer, sodium (2-acrylamido)-2-methylpropanesulfonate and *N*-dodecylmethacrylamide p(AMPS/C12). (b) Radial distribution functions of dodecyl carbon, main-chain carbon, and sulfonate sulfur atoms obtained by MD simulation.[16]

I-2-3. Threadlike Micelles Composed of Low Molar Mass Surfactants.

When the added salt concentration increases, the micelle formed by low molar mass ionic surfactants changes from the spherical to threadlike one. This may be due to the reduction of electrostatic repulsion among ionic surfactants in the micelle, which leads to reduce the effective cross section a_0 and to increase the shape factor λ given by eq I-1. For non-ionic surfactants, when the relative length of the hydrophilic moiety becomes shorter, the micelle transforms to threadlike.

The shape of threadlike micelles resembles that of flexible polymer chains. However, the characterization of threadlike micelles is not as easy as that for polymers, because their length depends on the concentration of the surfactant. Threadlike micelles composed of nonionic surfactants have been characterized by light scattering measurement and the analysis considering an inter-micellar interaction and a concentration dependence of the length.[17]

Threadlike micellar solution shows unique viscoelastic properties.[18-27] Figure I-3 shows a typical linear viscoelastic spectrum of an aqueous solution of an ionic surfactant / organic salt mixture at a high salt concentration. The storage modulus G' has rubbery plateau region like polymer systems. However, the modulus G^* in the terminal flow region shows unique behavior unlike polymer systems. The G^* fits to the single Maxwell model represented by

$$G' = \frac{G_N \omega^2 \tau^2}{1+\omega^2\tau^2}, \qquad G'' = \frac{G_N \omega\tau}{1+\omega^2\tau^2} \tag{I-17}$$

where G_N, ω and τ is the plateau modulus, angular frequency, and relaxation time, respectively. Shikata et al. [19] proposed a phantom-crossing model to describe this unique behavior. In this model, the τ corresponds to the life time of a temporary network. Cates et al. [28] described this behavior by using a similar model, and called threadlike micelle as a "living polymer", which means that the dynamics of threadlike micelles are identical with those of polymers in the frequency region higher than the life time of the micelles.

To verify this model, one has to make viscoelastic measurements in a time domain, shorter than the life time of the threadlike micelle. However, linear viscoelastic measurements up to the corresponding high frequency region are difficult by using conventional rheometers which can measure the linear viscoelastic spectrum only in the range of $10^{-2} \leq \omega / \mathrm{s}^{-1} < 10^{2}$. A new methodology is necessary for this task.

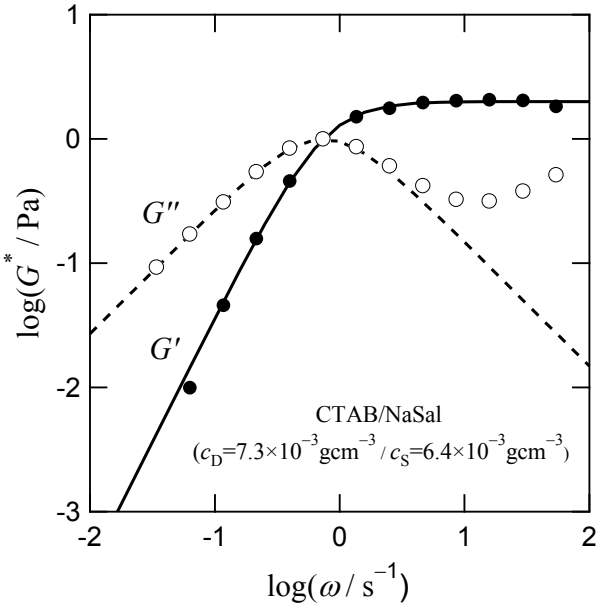

Figure I-3. Linear viscoelastic modulus G^* for an aqueous cetyltrimethyl ammonium bromide (CTAB) and sodium salicylate (NaSal) mixture solution. The solid and broken line represents G' and G'' calculated by eq I-17, respectively.

I-3. Scope of This Doctoral Thesis.

The aim of this thesis work is to develop methodology for characterizing structures and dynamics of various micelles. In spite of a long history of researches in micellar systems, the methodology has not been established yet, as mentioned in the previous section. The first half of this thesis (Chapter II and III), I focus on the characterization of the structures of spherical and flower micelles, and the second half (Chapter IV and V), I focus on the dynamics of threadlike micelles.

Chapter II deals with the characterization of hydrophobe uptake spherical micelles composed of low molar mass surfactant and hydrophobe near the CMC. When the surfactant concentration approaches to the CMC, the number of spherical micelles reduces and not all hydrophobe can be included in the micelles. As the result, the hydrophobe coming out from the micelles forms large particles in the aqueous solution, which induce anomalously strong light scattering. Due to this anomalous light scattering, the conventional analysis of light scattering cannot be used to characterize the major component of the hydrophobe uptake micelle in the solution near the CMC. To escape from this difficulty, I combine static and dynamic light scattering techniques, according to Kanao et al.[29] who studied weakly aggregating polymer solutions. Using this method, I can discuss the association-dissociation equilibrium for hydrophobe-uptake spherical micelles near the CMC.

In Chapter III, I investigate the structure of hydrophobe-uptake micelles composed of an amphiphilic alternating copolymer and hydrophobe. As mentioned in the previous section, the amphiphilic alternating copolymer was found to form the flower micelle in aqueous solution mainly using the light scattering technique. However, the hydrophobe uptake polymer micelle may have more complex structure, so that it may be difficult to characterize the micellar structure only by light scattering, which gives us the information of the molar mass and hydrodynamic radius of the micelle. To supplement light scattering data, small angle X-ray scattering (SAXS) measurements are carried out to obtain information of more local structure of the micelle. I characterize the hydrophobe uptake polymer micelle by combining the results of light scattering and SAXS.

Chapters IV and V deal with a new methodology for measuring the wideband viscoelasticity of aqueous micellar solutions. To characterize the dynamics of the threadlike micelle, linear viscoelastic spectrum up to the high frequency region is necessary. I noticed the microrheology[30-33] which measures the Brownian motion of a micron sized probe particle.

Among various microrheological measurements, the laser particle tracking (LPT) method[34-37] can measure the Brownian motion in the high frequency region. As described in Chapter IV, I refined the LPT method to obtain the linear viscoelastic spectrum accurate enough to make quantitative discussions. The reliability of the LPT method was checked by comparing the viscoelastic spectra obtained by this method and conventional rheometer in the overlapping frequency region.

In Chapter V, the LPT method developed is applied to measure linear viscoelastic spectra for aqueous threadlike micellar solutions of cationic and non-ionic surfactants up to high frequency region. The spectra are compared with theories for non-entangled and entangled polymer systems to discuss the resemblance of the dynamics of threadlike micelles and polymer systems. Furthermore, the viscoelastic spectra obtained for threadlike micelles provide the molar mass of the micelles by analyzing it with the Rouse model.[38,39] This is a new method for estimating the molar mass of threadlike micelles.

Finally, Chapter VI summarizes the main results and conclusions obtained in this doctoral work.

References.

1) Israelachvili, J. N. *Intermolecular and Surface Force* 2nd ed; Academic Press. 1992.
2) Matsushita, Y.; Sato, T.; Kanaya, T,; Ito, K.; Watanabe, H.; Tanaka, K.; Shimomura, T.; Inoue, T. *Structures and Physical Properties of Polymers*; Kodansha. 2013.
3) Borisov, O .V.; Halperin, A. *Langmuir.* **1995**, *11*, 2911.
4) Borisov, O .V.; Halperin, A. *Europhys. Lett.* **1996**, *34*, 657.
5) Borisov, O .V.; Halperin, A. *Phys. Rev. E.* **1998**, *57*, 812.
6) Debye, P. *J. Colloid. Sci.* **1948**, *3*, 407.
7) Debye, P. *Ann. N. Y. Acad. Sci.* **1949**, *51*, 575.

8) Corti, M.; Degiorgio, V. *Chem. Pys. Lett.* **1977**, *49*, 141.

9) Paillet, S.; Grassl, B.; Desbrieres, J. *Anal. Chim. Acta.* **2009**, *636*, 236.

10) Phillips, J. N.; Mysels, K. J. *J. Phys. Chem*. **1955**, *59*, 325.

11) Zhu, Z.; Reed, W. F. *Langmuir*. **2013**, *29*, 10376.

12) Noda, T.; Hashidzume, A.; Morishima, Y. *Langmuir*. **2001**, *17*, 5984.

13) Noda, T.; Hashidzume, A.; Morishima, Y. *Polymer*. **2001**, *42*, 9243.

14) Kawata, T.; Hashidzume, A.; Sato, T. *Macromolecules*. **2007**, *40*, 1174.

15) Ueda, M.; Hashidzume, A.; Sato, T. *Macromolecules*. **2011**, *44*, 2970.

16) Tominaga, Y.; Mizuse, M.; Hashidzume, A.; Morishima, Y.; Sato, T. *J. Phys. Chem. B*. **2010**, *114*, 11403.

17) Sato, T. *Langmuir*. **2004**, *20*, 1095.

18) Shikata, T.; Hirata, H.; Kotaka, T. *Langmuir*. **1987**, *3*, 1081.

19) Shikata, T.; Hirata, H.; Kotaka, T. *Langmuir*. **1988**, *4*, 354.

20) Inoue, T.; Inoue, Y.; Watanabe, H. *Langmuir*. **2005**, *21*, 1201.

21) Shikata, T.; Dahman, S. J.; Pearson, D. S. *Langmuir*. **1994**, *10*, 3470.

22) Takeda, M.; Kusano, T.; Matsunaga, T.; Endo, H. Shibayama, M. Shikata, T. *Langmuir*. **2011**, *27*, 1731.

23) Berret, J. F.; Appell, J.; Porte, G. *Langmuir*. **1993**, *9*, 2851.

24) Khatory, A.; Kern, F.; Lequeux, F.; Appell, J.; Porte, G.; Morie, N.; Ott, A.; Urbach, W. *Langmuir*. **1993**, *9*, 933.

25) Nakamura, K.; Shikata, T. *Macromolecules*. **2003**, *36*, 9698.

26) Cappelaere, E.; Cressely, R. *Rheol. Acta*, **2000**,*39*, 346.

27) Berret, J. F. *Langmuir*. **1997**, *13*, 2227.

28) Cates, M. E. *Macromolecules*. **1987**, *20*, 2289.

29) Kanao, M.; Matsuda, Y.; Sato, T. *Macromolecules*. **2003**, *36*, 2093.

30) Kimura, Y. *J. Phys. Soc. Jpn*. **2009**, *78*, 041005.

31) Mason, T. G.; Weitz, D. A. *Langmuir*. **1995**, *11*, 4256.

32) Crocker, J. C.; Grier, D. G. *J. Colloid Interface. Sci*. **1996**, *179*, 298.

33) Weeks, E. R.; Crocker, J. C.; Levitt, A. C.; Schofield, A.; Weitz, D. A. *Science*. **2000**, *287*, 627.

34) Buchanan, M.; Atakhorrami, M.; Palierne, J. F.; MacKintosh, F. C.; Schmidt, C. F. *Phys. Rev. E*. **2005**, *72*, 011504.

35) Pesce, G.; De Luca, A. C.; Rusciano, G.; Netti, P. A.; Fusco, S.; Sasso, A. *J. Opt. A: Pure Appl. Opt.* **2009**, *11*, 034016.

36) Schnurr, B.; Gittes, F.; MacKintosh, F. C.; Schmidt, C. F. *Macromolecules.* **1997**, *30*, 7781.

37) Yao, A.; Tassieri, M.; Padgett, M.; Cooper, J. *Royal Chem. Soc*. **2009**, *9*, 2568.

38) Pesce, G.; Sasso, A. Fusco, S. *Rev. Sci. Instr.* **2005**, *76*, 115105.

39) Rouse, P. E. *J. Chem. Phys.* **1953**, *21*, 1272.

40) Ferry, J. D. *Viscoelastic Properties of Polymers*, 3rd ed.; Wiley: New York, 1980.

Chapter II.

Light Scattering from Hydrophobe-Uptake Spherical Micelles Composed of Low Molar Mass Surfactants near the Critical Micelle Concentration

II-1. Introduction.

The hydrophobe-uptake micellization has been investigated for many systems,[1-8] because the hydrophobe-uptake behavior is one of the most important problem for developing extensive applications in detergents, paints, and drugs, as well as potential applications to nano-carriers and nano-reactors. Many researches were interested in the micellization at surfactant concentrations much higher than the critical micelle concentration (CMC), and characterized micellar structure in detail by scattering techniques and electron microscopy.[9-13] However, near the CMC, it is difficult to apply these techniques to study the association-dissociation equilibrium behavior of the surfactants.

Near the CMC, the micelle becomes less stable and sensitive to the solution temperature. Thus, it is difficult to prepare samples for cryo-transmission electron microscopy (cryo-TEM) near the CMC. To my best knowledge, the micellization behavior near the CMC has been little studied by cryo-TEM. Moreover, the CMC for conventional surfactants is usually so low that the intensity of small-angle X-ray or neutron scattering is too weak to study the micellization behavior. Therefore, the most suitable technique to study the association−dissociation equilibrium near the CMC may be light scattering. However, this technique has also a difficulty mentioned in the following.

When a hydrophobic substance is added to an ionic low molar mass surfactant in aqueous solution, two kinds of assemblies are formed in the solution.[4] One is the small micelle comprising the surfactant and the hydrophobe included in the hydrophobic core of the micelle. The other is a large colloidal particle consisting of the hydrophobe and stabilized by

the surfactant. On one hand, when the amount of the surfactant is much larger than the amount of the hydrophobe, and the concentration of the surfactant is higher than CMC, the assembly in the solution is the spherical micelle. On the other hand, when the amount of the surfactant is still larger than the amount of the hydrophobe but the surfactant concentration is near the CMC, large colloidal particles of the hydrophobe appear in the solution because of difficulty of the spherical micelle formation. The formation of the large colloidal particles enormously increases light scattering intensity.[1-4,13,14] Even if no hydrophobe is added to the solution, a tiny amount of impurity in the surfactant sample may act as hydrophobe, and light scattering intensity increases unexpectedly near the CMC.[5,15] This strong scattering intensity from the large colloidal particles makes difficult to analyze the association-dissociation equilibrium behavior of the surfactants using the light scattering data.

Similar difficulties have been often encountered at light scattering studies on polymer solutions which contain a small amount of large particles (sometimes dusts or aggregates). Kanao et al.[16] proposed to escape such difficulties in polymer solutions by separating the static light scattering intensity into small and large scattering components using dynamic light scattering data.

I here apply their method to aqueous solutions containing mixtures of a surfactant and a hydrophobe near the CMC in order to study the association−dissociation equilibrium in the solutions using the scattering intensity for the small scattering component separated. In this study, I have chosen dodecylpyridinium chloride (DPC) and sodium dodecylsulfate (SDS) as the cationic and anionic surfactant, respectively. I have chosen 1-dodecanol (DOH) as the hydrophobe. Although the DOH molecule has a hydroxyl group, its amphiphilicity is so weak that its aqueous solution undergoes a liquid-liquid phase separation. Thus, it behaves as a hydrophobe in aqueous solutions.

II-2. Experimental Section.

II-2-1. Materials.

Dodecylpyridinium chloride (DPC) and sodium dodecylsulfate (SDS) were purchased from Sigma Aldrich. Sodium tetraborate decahydrate (Borax) and 1-dodecanol (DOH) were purchased from Wako Pure Chemical Industries, Ltd. Borax were chosen to use as electrolyte and buffer (pH = 9.3) in aqueous solutions. DPC and SDS were recrystallized from acetone and ethanol five times, respectively. DOH was used without further purification. Water was purified with a Millipore Milli-Q system, which was used as solvent of test solutions.

II-2-2. Preparation of Test Solution.

Test solutions were prepared in the following manner. Aqueous Borax solution (40 mM) was used as electrolyte solvent for all sample solution. Purified surfactant (DPC or SDS) and neat DOH were mixed well at weight ratio of DOH to surfactant, c_H/c_R. Then the surfactant–DOH mixture was dissolved in the aqueous Borax solution. Concentrated original solution was prepared at $c_R = 5.0\times10^{-2}$ g cm^{-3}, which is about ten times higher than the CMC for the surfactants. Test solutions were prepared with dilution of original solutions by aqueous Borax solution. In this study, mass concentration of surfactant and DOH are represented by c_R and c_H, respectively. Then total mass concentration is represented by c (= c_R + c_H). The subscripts R and H indicate the surfactant and DOH, respectively.

II-2-3. Specific Refractive Index Increment Measurement.

Specific refractive index increments $\partial n/\partial c$ for sample solutions were measured using a modified Schulz–Cantow type differential refractometer (Shimazu) with 488 and 546 nm wavelength light at 25.0 °C. Values of $\partial n/\partial c$ at λ_0 (wavelength) = 532 nm were obtained by

interpolation of $\partial n/\partial c$ values at $\lambda_0 = 488$ and 546 nm to be 0.172 cm^3g^{-1} for DPC system and 0.120 cm^3g^{-1} for SDS system, respectively at $c_H/c_R = 0$. A value of $\partial n/\partial c$ at any c_H/c_R can be obtained by

$$\frac{\partial n}{\partial c} = \frac{c_R}{c}\left(\frac{\partial n}{\partial c}\right)_R + \frac{c_H}{c}\left(\frac{\partial n}{\partial c}\right)_H \qquad \text{(II-1)}$$

Here, $(\partial n/\partial c)_R$ and $(\partial n/\partial c)_H$ are the value at $c_H/c_R = 0$ and ∞, respectively. $(\partial n/\partial c)_H$ could be determined by eq II-1 using the experimental result (0.169 cm^3g^{-1}) at $c_H/c_R = 0.1$ of DPC system to be $(\partial n/\partial c)_H = 0.140$ cm^3g^{-1}.

II-2-4. Light Scattering Measurements.

Test solutions for light scattering measurements were optically cleaned by filtration through a 0.2 μm pore–size membrane filter before dilution of original solution. Simultaneous static and dynamic light scattering measurements were carried out for aqueous Borax solutions of surfactant–DOH mixtures using ALV/SLS/DLS–5000 light scattering instrument equipped with an ALV–5000 multiple τ digital correlator. Vertically polarized light with the wavelength $\lambda_0 = 532$ nm emitted from an Nd:YAG laser was used as incident light. The light scattering system was calibrated using toluene as the reference material. The Rayleigh ratio of toluene R_{tol} for vertically polarized 532 nm light was taken to be 2.72×10^{-5} cm^{-1} at 25 °C.[17] The excess Rayleigh ratio R_θ at scattering angle θ of each solution over that of the solvent was calculated from the scattering intensity of the solution $I_{\theta,soln}$ and solvent $I_{\theta,solv}$ by the standard procedure.[16] The intensity auto-correlation function $g^{(2)}(t)$ obtained by dynamic light scattering (DLS) was analyzed by CONTIN to obtain the spectrum $A(\tau)$ of the relaxation time τ. All measurement was carried out at 25 °C.

II-2-5. Analysis of Light Scattering Data.

When the relaxation time spectrum $A(\tau)$ obtained by DLS is bimodal, the solution

contains two scattering components of largely different sizes. Using the bimodal $A(\tau)$, the excess Rayleigh ratio R_θ obtained by static light scattering (SLS) is divided into the fast relaxation component $R_{\theta,\mathrm{fast}}$ and the slow relaxation component $R_{\theta,\mathrm{slow}}$ by

$$R_{\theta,\mathrm{fast}} = \frac{\int_{\mathrm{fast}} A(\tau)d\tau}{\int_{\mathrm{all}} A(\tau)d\tau} R_\theta, \qquad R_{\theta,\mathrm{slow}} = \frac{\int_{\mathrm{slow}} A(\tau)d\tau}{\int_{\mathrm{all}} A(\tau)d\tau} R_\theta \tag{II-2}$$

The light scattering power of the slow relaxation component is usually much stronger than that of the fast relaxation component. Therefore, if $R_{\theta,\mathrm{fast}}$ and $R_{\theta,\mathrm{slow}}$ are comparable, the weight fraction of the slow relaxation component may be very small. In such a case, $R_{\theta,\mathrm{fast}}$ and $R_{\theta,\mathrm{slow}}$ for dilute solutions are written as[16,18]

$$\frac{K'c}{R_{\theta,\mathrm{fast}}} = \left(\frac{\partial n}{\partial c}\right)^{-2}_{\mathrm{fast}} \left(\frac{1}{w_{\mathrm{fast}} M_{\mathrm{w,fast}}} + 2A_{2,\mathrm{fast}}c\right) \tag{II-3a}$$

$$\frac{K'c}{R_{\theta,\mathrm{slow}}} = \left(\frac{\partial n}{\partial c}\right)^{-2}_{\mathrm{slow}} \left[w_{\mathrm{slow}} M_{\mathrm{w,slow}} P_{\mathrm{z,slow}}(k)\right]^{-1} \tag{II-3b}$$

where $\partial n/\partial c$, w, M_w, A_2, and $P_\mathrm{z}(k)$ are the refractive index increment, the weight fraction (in the total scattering components), the weight-average molar mass, the second virial coefficient, and the z-average particle scattering function, respectively, and subscripts fast and slow indicate the quantities for the fast and slow relaxation components, respectively. The optical constant K' is defined as

$$K' = \frac{4\pi^2 n_0^2}{N_\mathrm{A}\lambda_0^4} \tag{II-4}$$

with the refractive index of solvent n_0, and the Avogadro constant N_A. The argument k of $P_{\mathrm{z,slow}}(k)$ is the magnitude of the scattering vector. In the above equations, the angular dependence of $R_{\theta,\mathrm{fast}}$ was neglected on the assumption that the size of the fast relaxation component is much smaller than the wavelength of the incident light. The concentration dependence of $R_{\theta,\mathrm{slow}}$ can be neglected in a good approximation[16].

Using the bimodal $A(\tau)$,the first cumulants of the fast and slow relaxation components, Γ_{fast} and Γ_{slow}, can be also calculated by

$$\Gamma_{fast} = \frac{\int_{fast} \tau^{-1} A(\tau) d\tau}{\int_{fast} A(\tau) d\tau}, \qquad \Gamma_{slow} = \frac{\int_{slow} \tau^{-1} A(\tau) d\tau}{\int_{slow} A(\tau) d\tau} \tag{II-5}$$

These first cumulants give us the hydrodynamic radius of each component by

$$R_{H,fast} = \frac{k_B T}{6\pi\eta_0} \left(\lim_{c,k\to 0} \frac{\Gamma_{fast}}{k^2} \right)^{-1}, \; R_{H,slow} = \frac{k_B T}{6\pi\eta_0} \left(\lim_{k\to 0} \frac{\Gamma_{slow}}{k^2} \right)^{-1} \tag{II-6}$$

where $k_B T$ is the Boltzmann constant multiplied by the absolute temperature, and η_0 is the solvent viscosity. In the above equation, the interparticle interaction effect on $R_{H,slow}$ was neglected on the assumption that the slow relaxation component appears only in very dilute solutions.

II-3. Results and Discussion.

II-3-1. Light Scattering Results.

Figure II-1 shows SLS results for aqueous Borax solutions of a DPC–DOH mixture of $c_H/c_R = 0.1$, with different total solute concentrations c (= $c_R + c_H$). The scattering intensity increases drastically between 1.1×10^{-2} g cm^{-3} and 5.5×10^{-3} g cm^{-3}. While $R_\theta/K'c$ exhibits no angular dependence at $c \geq 1.1 \times 10^{-2}$ g cm^{-3}, it exhibits strong angular dependence at $c \leq 5.5 \times 10^{-3}$ g cm^{-3}. Since DPC is known to form a small spherical micelle in aqueous salt solution above the CMC,[19] the angular independence of the scattering function at $c \geq 1.1 \times 10^{-2}$ g cm^{-3} is normal, but the strong angular dependence of $R_\theta/K'c$ demonstrates the existence of large colloidal particles, probably comprising DOH, in the solution with $c \leq 5.5 \times 10^{-3}$ g cm^{-3}.

The anomalous light scattering starts occurring at the concentration close to the CMC for DPC in aqueous solutions with a similar ionic strength,[19,20] and such light scattering

behavior was observed for many aqueous surfactant solutions.[1-5,13,14] Similar behavior is observed for aqueous Borax solutions of DPC–DOH mixtures with $c_H/c_R < 0.1$ and SDS–DOH mixtures with $c_H/c_R < 0.05$ also near the CMC of aqueous DPC and SDS.

As shown in Figure II-2, the similar strong angular dependence of $R_\theta/K'c$ is observed even for aqueous Borax solutions of DPC and SDS ($c_H/c_R = 0$) with $c = c_R \leq 3.0 \times 10^{-3}$ g cm^{-3}. The large scattering component in surfactant solutions may consist of a tiny amount of some hydrophobic impurity including in the surfactant sample.

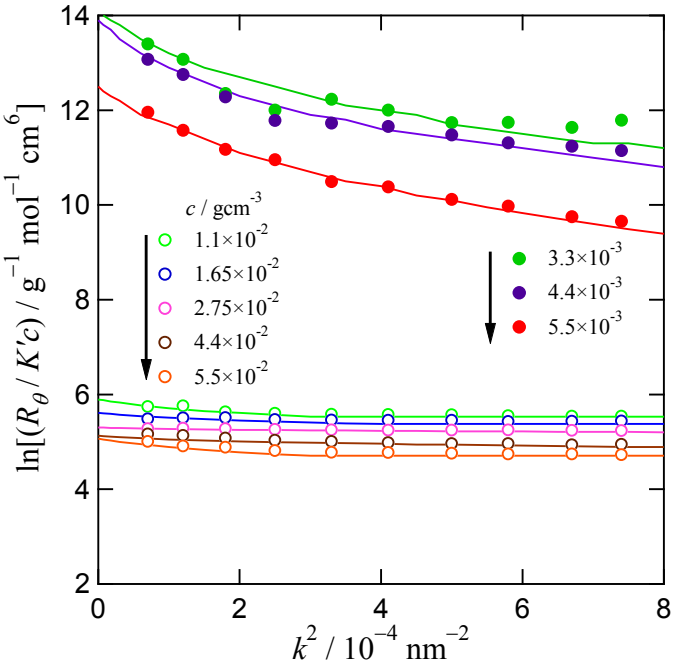

Figure II-1. Angular dependence of $\ln(R_\theta/K'c)$ for aqueous Borax solutions of a DPC–DOH mixture of $c_H/c_R = 0.1$ with different total solute concentrations $c = c_R + c_H$. Solid lines are eye guides.

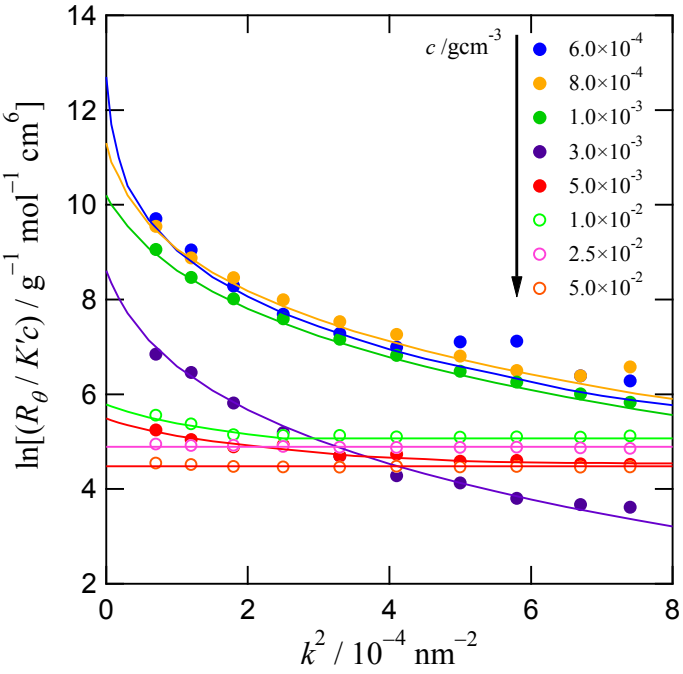

Figure II-2. Angular dependence of $\ln(R_\theta/K'c)$ for aqueous Borax solutions of DPC (c_H/c_R = 0) with different total solute concentrations $c = c_R + c_H$. Solid lines are eye guides.

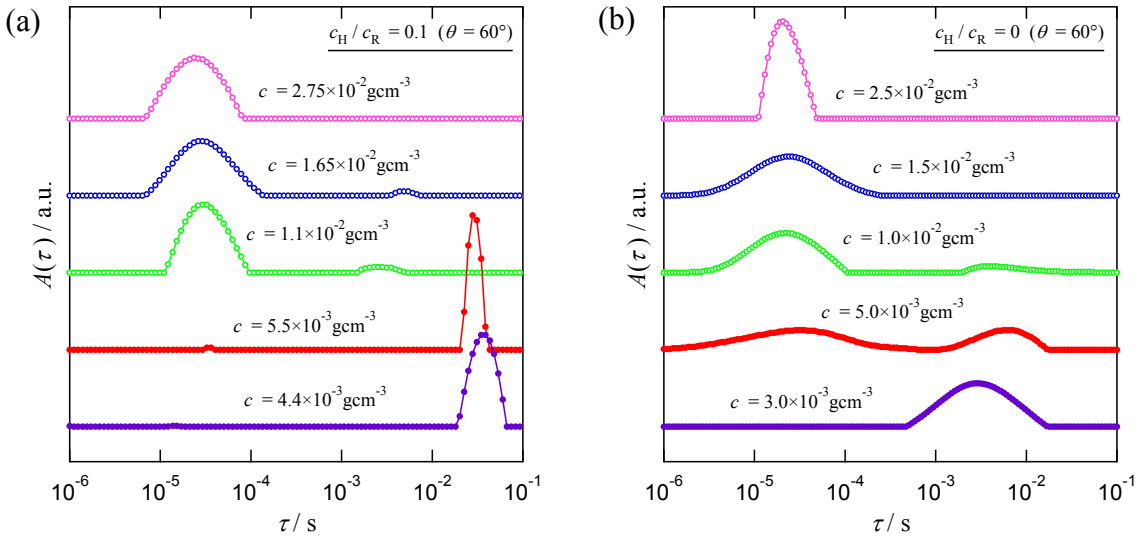

Figure II-3. Relaxation time spectra of the intensity autocorrelation function at scattering angle $\theta = 60°$ for aqueous Borax solutions of and (a) DPC–DOH mixture of c_H/c_R = 0.1 and (b) DPC (c_H/c_R = 0) with different c.

Figure II-3 shows the concentration dependence of the relaxation time spectra $A(\tau)$ of the intensity autocorrelation function $g^{(2)}(t)$ for aqueous Borax solutions of DPC ($c_H/c_R = 0$) and the DPC–DOH mixture of $c_H/c_R = 0.1$ at scattering angle $\theta = 60°$. While $A(\tau)$ is unimodal at the highest concentration ($c = 2.75\times10^{-2}$ gcm^{-3}), it becomes bimodal with decreasing c. At low concentrations ($c \leq 5.5\times10^{-3}$ gcm^{-3}), $A(\tau)$ becomes unimodal again. Similar c dependence of $A(\tau)$ was also observed for the solutions having other c_H/c_R and for the solutions of SDS and SDS–DOH mixture.

According to the procedure described in the Experimental section, I divided R_θ, as shown in Figure II-1 and II-2, into the fast and slow relaxation components ($R_{\theta,\mathrm{fast}}$ and $R_{\theta,\mathrm{slow}}$), and also estimated the first cumulants of the fast and slow relaxation components (Γ_{fast} and Γ_{slow}), using the bimodal $A(\tau)$ as shown in Figure II-3. In what follows, I will discuss those fast and slow relaxation components separately. Occasionally, spectra for the slow relaxation component became multi-modal, but I did not make further mode-separation of the slow relaxation component, because the appearance of the multi-modes was not systematic. It is noted that the CONTIN analysis is sometimes affected by noise of the scattering intensity.

II-3-2. Slow Relaxation Component.

Figure II-4 shows the Guinier plots for the slow relaxation component in aqueous Borax solutions of the DPC–DOH mixture of $c_H/c_R = 0.1$ and of DPC ($c_H/c_R = 0$), with different c. All the scattering functions exhibit strong k dependence, indicating that the slow relaxation component have a large size which is comparable to the wavelength of the incident light.

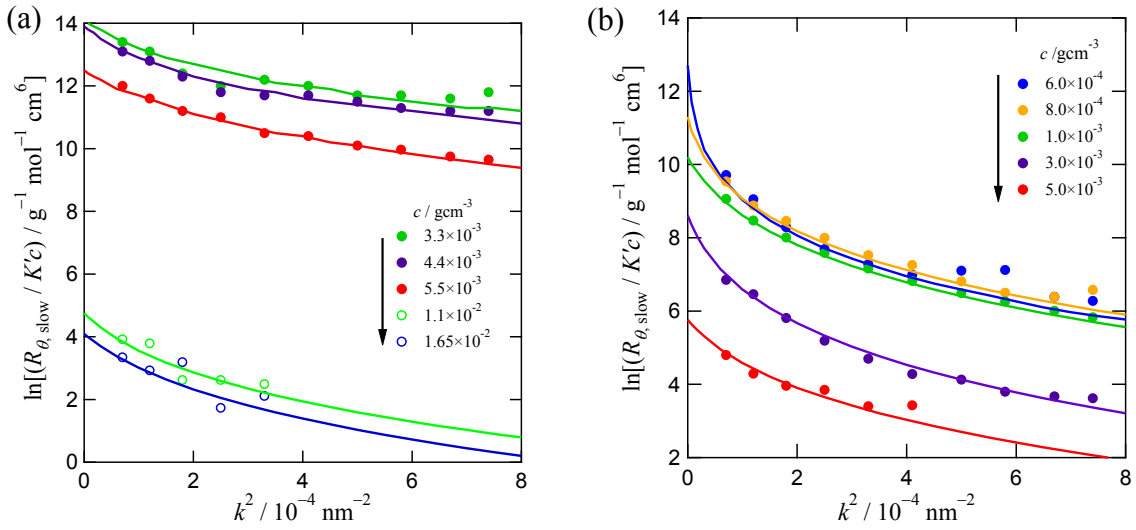

Figure II-4. Angular dependence of $\ln(R_{\theta,\mathrm{slow}}/K'c)$ for the slow relaxation component in aqueous Borax solutions of (a) a DPC–DOH mixture of c_H/c_R = 0.1 and of (b) DPC (c_H/c_R = 0), with different c.

I assume that the slow relaxation component in aqueous solutions of surfactant–DOH mixtures is colloidal particles composed of DOH, which are regarded as polydisperse spheres. Thus, in eq II-3b, $(\partial n/\partial c)_{\mathrm{slow}} = (\partial n/\partial c)_H$ (= 0.140 cm^{3}g^{-1}), and $M_{w,\mathrm{slow}}P_{z,\mathrm{slow}}(k)$ is given by

$$M_{w,\mathrm{slow}}P_{z,\mathrm{slow}}(k) = \int w(M)MP_{\mathrm{sphere},M}(k)dM \qquad \text{(II-7)}$$

where $w(M)$ is the weight fraction of the sphere with the molar mass M. $P_{\mathrm{sphere},M}(k)$ is the particle scattering function for the sphere with M given by

$$P_{\mathrm{sphere},M}(k) = \left[3\frac{\sin kR_M - kR_M\cos kR_M}{(kR_M)^3}\right]^2 \qquad \text{(II-8)}$$

with the radius of the sphere R_M calculated using the specific volume $\bar{\upsilon}_H$ of DOH (= 1.2 cm^3 g^{-1}) by

$$R_M = \left(\frac{3M\bar{\upsilon}_H}{4\pi N_A}\right)^{1/3} \qquad \text{(II-9)}$$

I further assume that the size distribution of the DOH spheres is represented by the

log-normal distribution defined as follows.

$$w(M)dM = \frac{1}{\sqrt{\pi}}\exp\left(-x^2\right)dx \tag{II-10}$$

$$x \equiv \frac{\ln\left(M/\sqrt{M_{\mathrm{w,slow}}M_{\mathrm{n,slow}}}\right)}{2\ln\left(M_{\mathrm{w,slow}}/M_{\mathrm{n,slow}}\right)} \tag{II-11}$$

As shown by solid curves in Figure II-4, the above equations fit the experimental $R_{\theta,\mathrm{slow}}/K'c$ satisfactorily, and w_{slow}, $M_{\mathrm{w,slow}}$, and $M_{\mathrm{w,slow}}/M_{\mathrm{n,slow}}$ is determined by the fitting. Although colloidal particles in aqueous solutions of $c_{\mathrm{H}}/c_{\mathrm{R}} = 0$ does not comprise DOH, probably some hydrophobic impurity in the surfactant sample. I carried out the same fitting as $c_{\mathrm{H}}/c_{\mathrm{R}} = 0.1$ for the solutions of $c_{\mathrm{H}}/c_{\mathrm{R}} = 0$ by assuming that the specific volume of the impurity is close to that of DOH.

The same fitting was made successfully for also SDS system. Table II-1 summarizes the fitting results, along with the weight average radius $R_{\mathrm{w,slow}}$ of the colloid, calculated by

$$R_{\mathrm{w,slow}} = \left(\frac{3M_{\mathrm{w,slow}}\bar{\upsilon}_{\mathrm{H}}}{4\pi N_{\mathrm{A}}}\right)^{1/3}\left(\frac{M_{\mathrm{n,slow}}}{M_{\mathrm{w,slow}}}\right)^{1/9}, \tag{II-12}$$

and the hydrodynamic radius $R_{\mathrm{H,slow}}$ of the slow relaxation component determined by the result of DLS.

It can be seen from Table II-1 that the weight average molar masses $M_{\mathrm{w,slow}}$ are very large, the dispersities $M_{\mathrm{w,slow}}/M_{\mathrm{n,slow}}$ are considerably large, and the weight fractions w_{slow} are very small in all the solutions. Because the light scattering power is proportional to $w_{\mathrm{slow}}M_{\mathrm{w,slow}}$, such tiny amounts of the scattering component are detectable. In the solutions of $c_{\mathrm{H}}/c_{\mathrm{R}} = 0$, w_{slow} are at most in order of 10^{-5}, which indicates high purity of the surfactant samples were used. The anomalous light scattering behavior in aqueous surfactant solutions near the CMC can occur even for highly purified surfactant samples.

It is sometimes pointed out that the appearance of the slow relaxation component in these systems near the CMC resembles the transition from the spherical micelle to the bilayer

vesicle in aqueous solutions of mixtures of two surfactants. Two kinds of mixtures have been studied previously about the micelle-bilayer transition: one is the mixture of single-tailed and double-tailed surfactants,[21,22] and the other is the mixture of oppositely charged surfactants.[23,24] However, DOH is not a surfactant but a hydrophobe not dispersed as a micelle in water by itself. Therefore, the appearance of the slow relaxation component in my systems near the CMC may have nothing to do with the micelle-bilayer transition reported previously for aqueous solutions containing two surfactants.

Although the slow component in this study may not resemble with the two surfactants systems as mentioned above, the other shapes for slow component should be discussed. Here, I tried to fit the $R_{\theta,\mathrm{slow}}/K'c$ data of DPC system by the scattering function for the vesicle (cf. Appendix). The fitting was also good, and it was difficult to distinguish the uniform density sphere from the vesicle by light scattering. (I have failed to distinguish them also from the ratio of the radius of gyration and hydrodynamic radius; cf. Appendix.) Sato et al.[25] distinguished spherical particles formed by a thermosensitive block copolymer in hot water from the vesicle by using small angle X-ray scattering (SAXS). However, the present low molar mass surfactant solutions close to the CMC were too dilute to obtain enough scattering intensity by SAXS (using the beamline 40B2 of SPring-8, Hyogo, Japan). Therefore, we cannot specify the shape of the slow relaxation component at present.

As shown in Table II-1a (in the parentheses), even if I assume that the slow relaxation component is the vesicle, the weight fraction w_{slow} of the slow relaxation component is also very small for solutions with detectable fast relaxation component. Therefore, in the following discussion of the fast relaxation component, we can neglect the amounts of surfactants and DOH in the slow relaxation component.

Table II-1. Characteristics of the slow relaxation component.

(a) Aqueous DPC-DOH mixture solutions

c_H/c_R	c / 10^{-3}g cm^{-3}	$M_{w,slow}$ / 10^8g mol^{-1}	$M_{w,slow}/M_{n,slow}$	w_{slow}	$R_{w,slow}$/nm	$R_{H,slow}$/nm
0.1	17*	100 (3.0)	10 (3)	3.0×10^{-7} (1.0×10^{-5})	130 (110)	130
	11*	110 (3.5)	15 (2)	5.4×10^{-7} (1.4×10^{-5})	130 (120)	140
	5.5	50 (3.0)	15 (3)	2.6×10^{-3} (5.2×10^{-2})	100 (110)	1600
	4.4	50 (4.0)	80 (20)	1.1×10^{-2} (2.0×10^{-1})	80 (100)	2200
	3.3	40 (5.0)	100 (30)	1.7×10^{-2} (2.9×10^{-1})	70 (110)	2100
0.05	11*	500 (20)	30 (3)	9.0×10^{-7} (2.5×10^{-5})	200 (280)	320
	5.3*	100 (4.0)	20 (2)	1.5×10^{-6} (3.0×10^{-5})	120 (130)	130
	4.2*	40 (2.0)	50 (3)	1.5×10^{-5} (2.5×10^{-4})	80 (90)	120
	3.2	80 (4.5)	300 (10)	3.8×10^{-3} (8.0×10^{-2})	80 (120)	1700
	2.1	60 (3.5)	200 (5)	5.0×10^{-3} (9.0×10^{-2})	80 (110)	5800
	1.05	150 (6.0)	500 (5)	2.3×10^{-3} (5.5×10^{-2})	90 (150)	4700
0.001	6.0*	400 (10)	3 (5)	4.3×10^{-6} (1.5×10^{-4})	240 (190)	370
	4.0	900 (9.0)	8 (3)	5.5×10^{-5} (2.5×10^{-3})	280 (190)	200
	3.0	250 (5.5)	100 (3)	1.9×10^{-5} (5.0×10^{-4})	140 (150)	160
	2.0	60 (2.0)	20 (5)	1.2×10^{-5} (2.8×10^{-4})	100 (80)	270
	1.0	100 (3.0)	20 (2)	7.0×10^{-5} (1.8×10^{-3})	120 (120)	800
	0.60	650 (10)	20 (3)	1.3×10^{-4} (5.0×10^{-3})	230 (200)	230
0	5.0*	100 (2.5)	20 (2)	1.7×10^{-6} (4.0×10^{-5})	120 (110)	190
	3.0	350 (5.0)	20 (1.5)	8.0×10^{-6} (2.0×10^{-4})	180 (150)	250
	1.0	200 (5.0)	20 (1.8)	7.0×10^{-5} (2.0×10^{-3})	150 (150)	200
	0.80	400 (5.0)	50 (1.7)	1.0×10^{-4} (3.0×10^{-3})	170 (150)	200
	0.60	2000 (8.0)	500 (1.7)	8.0×10^{-5} (3.5×10^{-3})	230 (190)	230

* Concentration where the fast relaxation component is observable by dynamic light scattering. Numbers in the parentheses, fitting results by using the scattering function for the vesicle (cf. Appendix).

(b) Aqueous SDS-DOH mixture solutions

c_H/c_R	c / 10^{-3}g cm^{-3}	$M_{w,slow}$ / 10^9g mol^{-1}	$M_{w,slow}/M_{n,slow}$	w_{slow}	$R_{w,slow}$/nm	$R_{H,slow}$/nm
0.05	5.3*	3.2	10	2.9×10^{-6}	90	110
	3.2*	3.2	15	4.9×10^{-6}	90	100
	2.1*	3.0	5	3.3×10^{-6}	100	90
	1.1	2.5	10	2.6×10^{-3}	80	130
	0.53	1.0	10	9.9×10^{-5}	60	60
0.03	5.2*	9.0	10	1.7×10^{-6}	130	100
	3.1*	4.0	40	5.3×10^{-6}	80	110
	2.6*	4.0	20	9.2×10^{-6}	90	120
	1.0*	3.0	100	2.0×10^{-5}	70	70
0.01	5.1*	3.0	5	3.6×10^{-6}	90	120
	3.0*	2.0	25	9.2×10^{-6}	70	110
	2.0*	2.0	30	1.3×10^{-5}	70	100
	1.0*	4.0	100	1.9×10^{-5}	70	90
0	5.0*	2.0	5	5.3×10^{-6}	80	100
	3.0*	1.5	15	1.7×10^{-5}	70	90
	2.0*	1.2	15	2.1×10^{-5}	60	90
	1.0*	2.4	20	3.1×10^{-5}	80	90
	0.5*	1.3	5	5.7×10^{-5}	70	80

* Concentration where the fast relaxation component is observable by dynamic light scattering.

II-3-3. Fast Relaxation Component.

Figure II-5 shows the Guinier plots for the fast relaxation component in aqueous Borax solutions of the DPC–DOH mixture of $c_H/c_R = 0.1$, with various c. All the scattering functions exhibit no angular dependence, indicating that the fast relaxation component have a size much smaller than the wavelength of the incident light. For each c, I estimated $R_{0,fast}$ at

the zero k by averaging $R_{\theta,\mathrm{fast}}$ at all measured k. Figure II-6 (the upper portion of each graph) shows the concentration dependence of $\ln(R_{0,\mathrm{fast}}/K'c)$ for four different c_H/c_R. For all c_H/c_R, $\ln(R_{0,\mathrm{fast}}/K'c)$ exhibits a maximum at concentrations slightly higher than the CMC.

There are three scattering components in the aqueous Borax solution containing the surfactant–DOH mixture; the dissociated surfactant molecule R, the spherical micelle R_m, and the colloidal particle. While the last component is regarded as the slow relaxation component, the first and second scattering components are considered as the fast relaxation component; it should be noted that I do not define the fast relaxation component as the only micellar component. The micelle R_m can be characterized by the aggregation number m of R and the molar mass $M_{m,H}$ of hydrophobe included in the micelle. Here, I assumed that the R_m is spherical micelle. According to the micellization theory,[26] spherical micelle formed by low molar mass surfactants has some optimum aggregation number, which is independent of concentration. Therefore, the value of m is assumed to be independent of concentration.

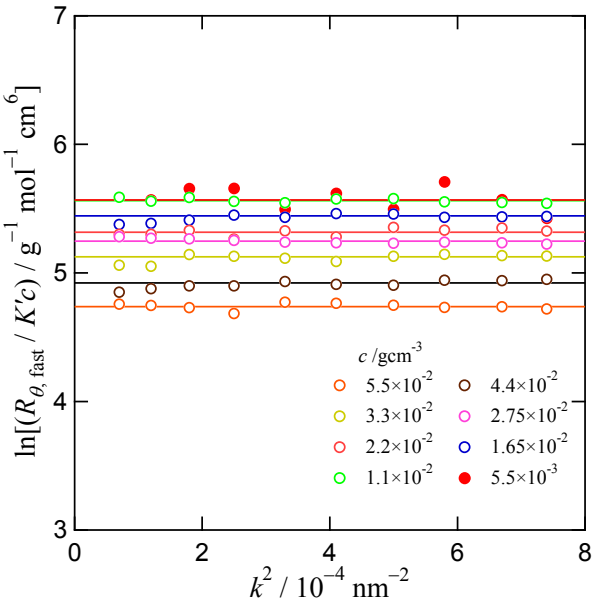

Figure II-5. Angular dependence of $\ln(R_{\theta,\mathrm{fast}}/K'c)$ for DPC-DOH solutions with c_H/c_R = 0.1.

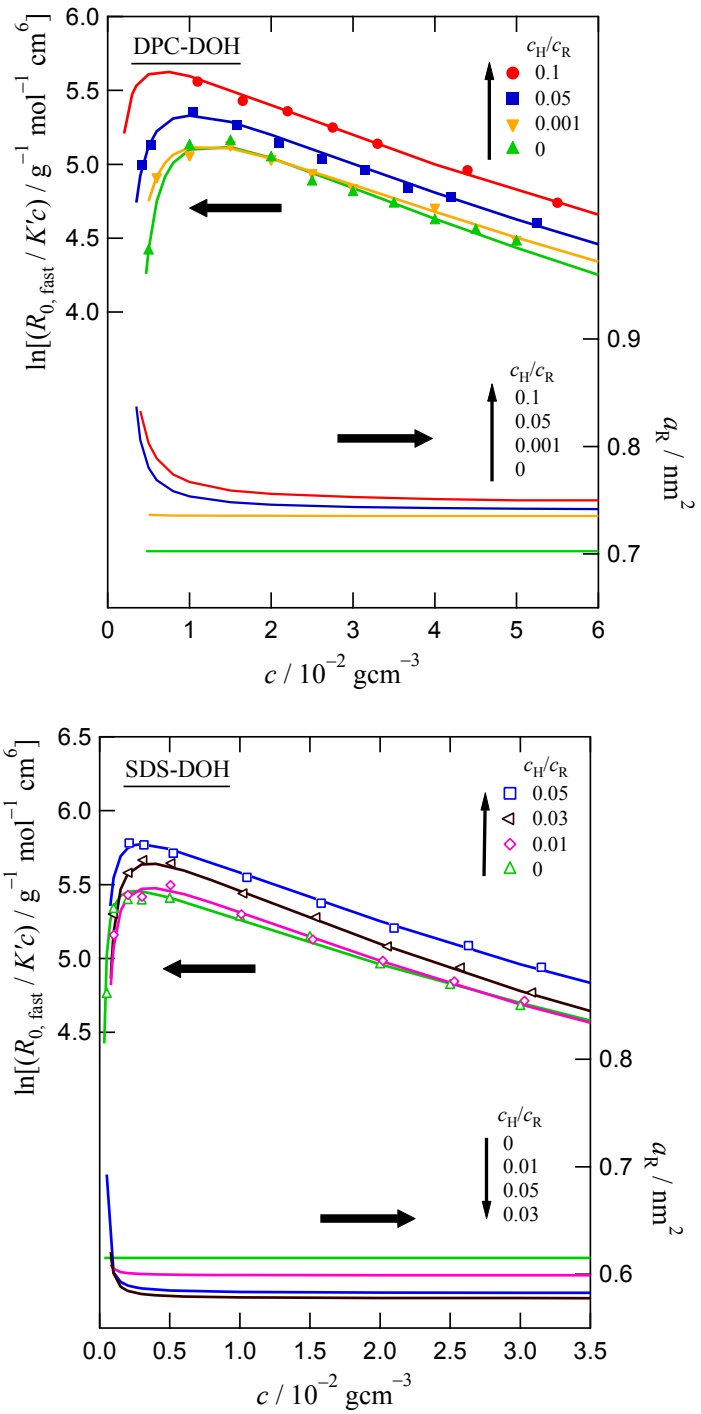

Figure II-6. Fitting results of $R_{0,fast}/K'c$ for DPC-DOH and SDS-DOH solutions by eq II-3a along with eqs II-13, II-14, II-17 – II 20, using m, K_m, and $A_{2,fast}$ as adjustable parameters, and calculated a_R by eqs II-15 and II-16 using the adjustable parameters determined.

The molar mass M_m of the spherical micelle is given by

$$M_m = mM_{\mathrm{R}} + M_{m,\mathrm{H}} \tag{II-13}$$

where M_{R} is the molar mass of R, and the refractive index increment $(\partial n/\partial c)_m$ of the micelle is given by

$$\left(\frac{\partial n}{\partial c}\right)_m = \frac{mM_{\mathrm{R}}}{M_m}\left(\frac{\partial n}{\partial c}\right)_{\mathrm{R}} + \frac{M_{m,\mathrm{H}}}{M_m}\left(\frac{\partial n}{\partial c}\right)_{\mathrm{H}} \tag{II-14}$$

The hydrophobic core of the micelle R_m comprises H and the hydrophobic tail of R. Thus, the volume of the core V_{core} is written as

$$V_{\mathrm{core}} = \bar{\upsilon}_{\mathrm{H}}\left(M_{m,\mathrm{H}}/N_{\mathrm{A}}\right) + \upsilon_{\mathrm{Rh}}m \tag{II-15}$$

where υ_{Rh} is the volume of the hydrophobic tail of R. The area a_{R} on the interface of the core occupied by each R molecule is calculated by

$$ma_{\mathrm{R}} = \left(3\sqrt{4\pi}V_{\mathrm{core}}\right)^{2/3} \tag{II-16}$$

Because the total amount of R on the interface of colloidal particles is negligibly small (cf. w_{slow} in Table II-1), the molar concentrations of the micelle $[\mathrm{R}_m]$ and of the free molecule [R] are related by

$$c_{\mathrm{R}}/M_{\mathrm{R}} = m[\mathrm{R}_m] + [\mathrm{R}] \tag{II-17}$$

Moreover, using the association constant K_m, $[\mathrm{R}_m]$ and [R] are related by

$$K_m = [\mathrm{R}_m]/[\mathrm{R}]^m \tag{II-18}$$

For given values of m and K_m, we can calculate $[\mathrm{R}_m]$ and [R] from eqs II-17 and II-18. Because the amount of DOH in the colloidal particle component is also negligibly small in comparison with the total H in the solution, $M_{m,\mathrm{H}}$ is calculated from $[\mathrm{R}_m]$ by

$$M_{m,\mathrm{H}} = c_{\mathrm{H}}/[\mathrm{R}_m] \tag{II-19}$$

The weight average molar mass of the fast relaxation component $M_{\mathrm{w,fast}}$ is calculated by

$$M_{\mathrm{w,fast}} = \frac{[\mathrm{R}]M_{\mathrm{R}}{}^2 + [\mathrm{R}_m]M_m{}^2}{[\mathrm{R}]M_{\mathrm{R}} + [\mathrm{R}_m]M_m} \qquad \text{(II-20)}$$

and the weight fraction of the fast relaxation component w_{fast} can be approximated to be unity, because of negligibly small w_{slow}. Although the refractive index increment of the free R is slightly different from $(\partial n/\partial c)_m$, I approximate $(\partial n/\partial c)_{\mathrm{fast}}$ in eq II-3a by $(\partial n/\partial c)_m$ (eq II-14), because the contribution of the free R to $R_{\theta,\mathrm{fast}}$ is small. Thus, $K'c/R_{\theta,\mathrm{fast}}$ can be calculated by eq II-3a along eqs II-13, II-14, II-17 – II-20, using m, K_m, and $A_{2,\mathrm{fast}}$ as adjustable parameters.

In the upper portion of each graph of Figure II-6, solid curves indicate fitting results of $R_{0,\mathrm{fast}}/K'c$ for DPC-DOH and SDS-DOH solutions in the Guinier plot by choosing suitable values for m, K_m, and $A_{2,\mathrm{fast}}$, which are listed in Table II-2. The fitting is satisfactorily good for all $c_{\mathrm{H}}/c_{\mathrm{R}}$ of both systems, demonstrating the appropriateness of the spherical model for the fast relaxation component. With increasing $c_{\mathrm{H}}/c_{\mathrm{R}}$, m and K_m seem to increase, and $A_{2,\mathrm{fast}}$ decreases, although the order is reversal for m and K_m at $c_{\mathrm{H}}/c_{\mathrm{R}}$ = 0 and 0.001 of the DPC system.

Figure II-6 also shows the area a_{R} on the interface of the hydrophobic core occupied by each R molecule (in the lower portion of each graph), calculated by eqs II-15 and II-16 using m and K_m determined for DPC-DOH and SDS-DOH systems. For the DPC-DOH system, a_{R} is constant at $c_{\mathrm{H}}/c_{\mathrm{R}}$ = 0 and 0.001 in the c range examined by light scattering, but at $c_{\mathrm{H}}/c_{\mathrm{R}}$ = 0.05 and 0.1, it increases rapidly with approaching c where the fast relaxation component disappears. Similar results are obtained for the SDS-DOH system. The decrease in the area density of the hydrophilic moiety of R leads to penalty of the interfacial energy, and this instability makes the spherical micelle destroy and the hydrophobe release.

Figure II-7 shows the concentration dependence of the first cumulant of the fast relaxation component in DPC-DOH solutions. As explained the reason below, I have determined the hydrodynamic radius $R_{\mathrm{H,fast}}$ by extrapolating $\Gamma_{\mathrm{fast}}k^{-2}$ (determined from the

result of DLS) to the infinite dilution using the data of $c > 0.02$ g cm^{-3}.

The hydrodynamic radius $R_{\mathrm{H,fast}}$ is given by

$$R_{\mathrm{H,fast}}^{-1} = \frac{[\mathrm{R}]M_{\mathrm{R}} R_{\mathrm{H,R}}^{-1} + [\mathrm{R}_m]M_m R_{\mathrm{H},m}^{-1}}{[\mathrm{R}]M_{\mathrm{R}} + [\mathrm{R}_m]M_m} \tag{II-21}$$

where $R_{\mathrm{H,R}}$ and $R_{\mathrm{H},m}$ are the hydrodynamic radii of the free R and the micelle R_m, respectively. As mentioned above, when $c > 0.02$ g cm^{-3}, a_{R} and then m of R_m are almost constant for all $c_{\mathrm{H}}/c_{\mathrm{R}}$, so that $\Gamma_{\mathrm{fast}}k^{-2}$ can be extrapolated to the infinite dilution without changing $R_{\mathrm{H},m}$. In Figure II-7, I have made such extrapolations to obtain $R_{\mathrm{H,fast}}$. We can also roughly estimate $R_{\mathrm{H,R}}$ of the free DPC; the root-mean-square end-to-end distance of *n*-dodecane is ca. 1 nm, and the size of the pyridine ring is about 0.3 nm, so that $R_{\mathrm{H,R}} \sim 1.5$ nm. Using $R_{\mathrm{H,fast}}$ and $R_{\mathrm{H,R}}$ along with m and K_m determined above, we can calculate $R_{\mathrm{H},m}$ from eq II-21. The results are also listed in Table II-2.

If the spherical micelle R_m is regarded as the hard sphere, $R_{\mathrm{H},m}$ and its second virial coefficient $A_{2,m}$ may be approximately calculated by

$$R_{\mathrm{H},m} = \left(\frac{3\bar{\upsilon}_{\mathrm{H}} M_m}{4\pi N_{\mathrm{A}}} \right)^{1/3}, \quad A_{2,m} = \frac{4\bar{\upsilon}_{\mathrm{H}}}{M_m} \tag{II-22}$$

At the fitting of $R_{0,\mathrm{fast}}/K'c$ shown in Figure II-6, the second virial coefficient is important only in a high c region where the scattering from R_m is predominant in $R_{0,\mathrm{fast}}$, so that $A_{2,\mathrm{fast}}$ determined by the fitting may be approximately equal to $A_{2,m}$. Figure II-8 compares experimental $R_{\mathrm{H},m}$ and $A_{2,\mathrm{fast}}$ for hydrophobe-uptake micelles of DPC-DOH and SDS-DOH mixtures with eqs II-22. I have used $\bar{\upsilon}_{\mathrm{H}}$ for DOH (= 1.2 cm^3 g^{-1}) to obtain the solid curves in the figure, but the results did not so much change even if I use $\bar{\upsilon}_{\mathrm{H}}$ for *n*-dodecane (= 1.3 cm^3 g^{-1}). The agreement between the experiment and theory for $R_{\mathrm{H},m}$ is reasonably good, demonstrating that DPC and SDS form the spherical micelle containing DOH inside the core in aqueous Borax solution. However, the magnitude of $A_{2,\mathrm{fast}}$ is higher than $A_{2,m}$ calculated by

eq II-22, although they show the similar concentration dependence ($\propto 1/M_m$). The latter disagreement is owing to the electrostatic repulsion between micelles, which is not considered in eq II-22.

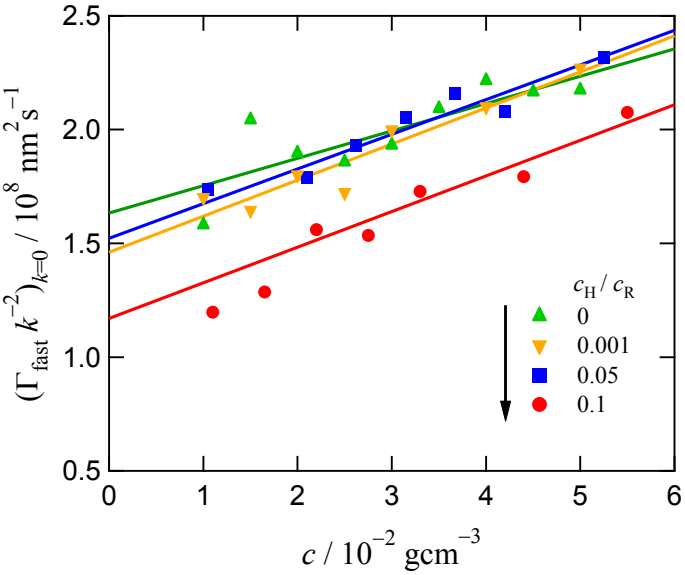

Figure II-7. Concentration dependence of $(\Gamma_{fast}\, k^{-2})_{k=0}$ for DPC-DOH solutions with four different c_H/c_R.

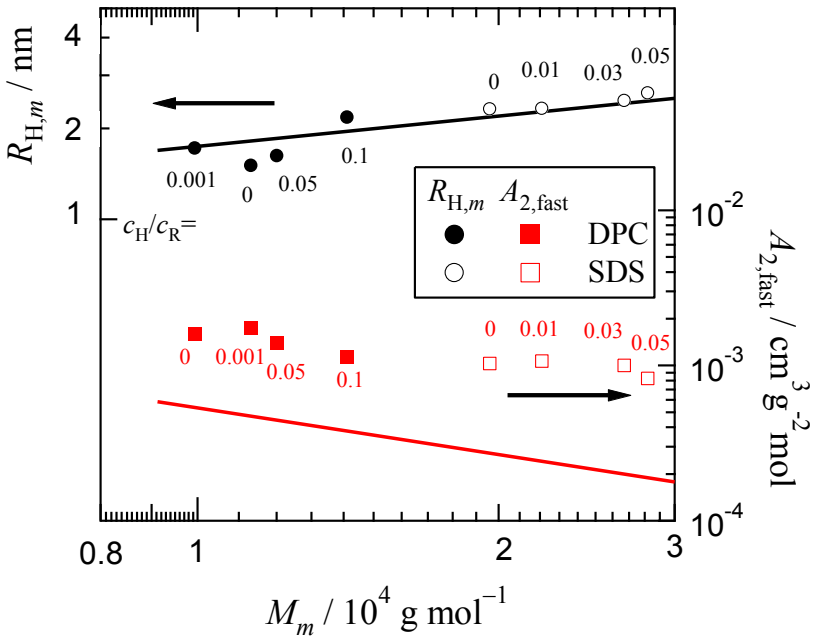

Figure II-8. Comparison of experimental $R_{H,m}$ and $A_{2,fast}$ for hydrophobe-uptake micelles of DPC-DOH and SDS-DOH mixtures with those for the hard sphere calculated by eqs II-22.

Table II-2. Characteristics of the spherical micelle R_m.

(a) Aqueous DPC-DOH mixture solutions

c_H/c_R	m	log (K_m/M^{1-m})	$A_{2,fast}$ / 10^{-3}cm^{3}g^{-2}mol	$R_{H,m}$ / nm
0.1	44	101	1.13	2.2
0.05	40	78.5	1.40	1.6
0.001	35	65.5	1.60	1.7
0	40	71.0	1.75	1.5

(b) Aqueous SDS-DOH mixture solutions

c_H/c_R	m	log (K_m/M^{1-m})	$A_{2,fast}$ / 10^{-3}cm^{3}g^{-2}mol	$R_{H,m}$ / nm
0.05	93	262	0.825	2.6
0.03	90	239	1.00	2.5
0.01	76	205	1.08	2.3
0	68	205	1.03	2.3

II-4. Conclusion.

I have investigated the light scattering peak phenomenon in hydrophobe-uptake micellar solutions near the critical micelle concentration (CMC) by separating the scattering intensity into the fast and slow relaxation components using dynamic light scattering results. There are three scattering components in the solutions: the free surfactant molecule R, the spherical micelle R_m consisting of m surfactant molecules and a small amount of the hydrophobe in the hydrophobic core, and the large colloidal particle of the hydrophobe stabilized by the surfactant. The fast relaxation component corresponds to the scattering from the first and second scattering components R and R_m, and I analyzed the association−dissociation equilibrium of the hydrophobe-uptake micelle even near the CMC by

using this scattering component extracted. The size and the aggregation number m of R_m increase only slightly with increasing the mixing ratio c_H/c_R, and little depend on the total solute concentration c (= $c_R + c_H$) at fixed c_H/c_R, except near the CMC.

The slow relaxation component gave us the information about the large colloidal particle component. Although it could not be judged whether this component is the uniform density sphere or vesicle from the light scattering data alone, it turned out that the amount of this component is very tiny in the solution. Due to its small amount, the droplet component hardly affects the association–dissociation equilibrium of the hydrophobe-uptake micelle.

Appendix.

Characterization of the Slow Relaxation Component.

Scattering intensities $R_{\theta,\mathrm{slow}}/K'c$ of the slow relaxation component shown in Figure II-4 were fitted by the scattering function for the polydisperse uniform density sphere given by eqs II-3b and II-7 – II-11. The fitting results are shown by solid curves in Figure II-4 and the parameters used in the fitting are listed in Table II-1.

If the slow relaxation component is regarded as polydisperse vesicle, the scattering function may be calculated similarly from eqs II-3b and II-7 – II-11, and

$$P_{\mathrm{vesicle},M}(k) = \left(\frac{\sin kR_M}{kR_M}\right)^2 \qquad \text{(II-8')}$$

$$R_M = \left(\frac{M\bar{\upsilon}_\mathrm{H}}{4\pi N_\mathrm{A} d}\right)^{1/2} \qquad \text{(II-9')}$$

instead of eqs II-8 and II-9, where d is the thickness of the hydrophobic layer of the vesicle. Furthermore, the weight average radius R_w of the vesicle may be calculated by

$$R_{\mathrm{w,slow}} = \left(\frac{M_{\mathrm{w,slow}}\bar{\upsilon}_\mathrm{H}}{4\pi N_\mathrm{A} d}\right)^{1/2}\left(\frac{M_{\mathrm{n,slow}}}{M_{\mathrm{w,slow}}}\right)^{1/8} \qquad \text{(II-12')}$$

I tried to fit $R_{\theta,\mathrm{slow}}/K'c$ data by the scattering function for the vesicle with $d << R_{\mathrm{w,slow}}$, which is much different from the uniform density sphere in shape. Even choosing d = 3 nm, I obtained fitting results similar to the fitting by the uniform density sphere, and Table II-1 summarizes parameter values used at the fitting (numbers in the parentheses). Therefore, it was difficult to distinguish the sphere and vesicle by the fitting of light scattering data.

The slow relaxation component is also characterized by the hydrodynamic radius $R_{\mathrm{H,slow}}$, estimated from dynamic light scattering data. Figure II-A1 shows the k^2 dependence of $\Gamma_{\mathrm{slow}}k^{-2}$ for aqueous Borax solutions of the DPC–DOH mixture of $c_{\mathrm{H}}/c_{\mathrm{R}}$ = 0.1 and of DPC, with different c. From the intercept of each plot, I have determined the hydrodynamic radius $R_{\mathrm{H,slow}}$ of the slow relaxation component using eq II-6. The results are also listed in Table II-1. When c is considerably higher than the CMC, $R_{\mathrm{H,slow}}$ is close to $R_{\mathrm{w,slow}}$, but for solutions with $c_{\mathrm{H}}/c_{\mathrm{R}}$ = 0.1 and 0.05, $R_{\mathrm{H,slow}}$ is much larger than $R_{\mathrm{w,slow}}$, when c approaches to the CMC, or w_{slow} becomes larger. At present, the reason for these discrepancies between $R_{\mathrm{H,slow}}$ and $R_{\mathrm{w,slow}}$ is not clear.

The radius of gyration $\langle S^2\rangle_{\mathrm{slow}}^{1/2}$ of the slow relaxation component may be obtained from the initial slope of the plot of $R_{\theta,\mathrm{slow}}/K'c$ vs. k^2, although the strong k^2 dependence shown in Figure II-4 makes difficult to estimate the accurate initial slope. It is known that the ratio of the radius of gyration to the hydrodynamic radius depends on the shape of the scatterer; the ratio is 0.775 for uniform density sphere and 1 for the vesicle with a thin hydrophobic layer. However, the ratio also depends on the size distribution of the scattering component. Unfortunately, the polydispersity effect is stronger for the vesicle than the sphere, so that the difference in the ratio between the vesicle and the sphere may become smaller for polydisperse systems. Taking into account the experimental uncertainties in $\langle S^2\rangle_{\mathrm{slow}}^{1/2}$ and $R_{\mathrm{H,slow}}$, I gave up to distinguish the sphere and vesicle by the ratio.

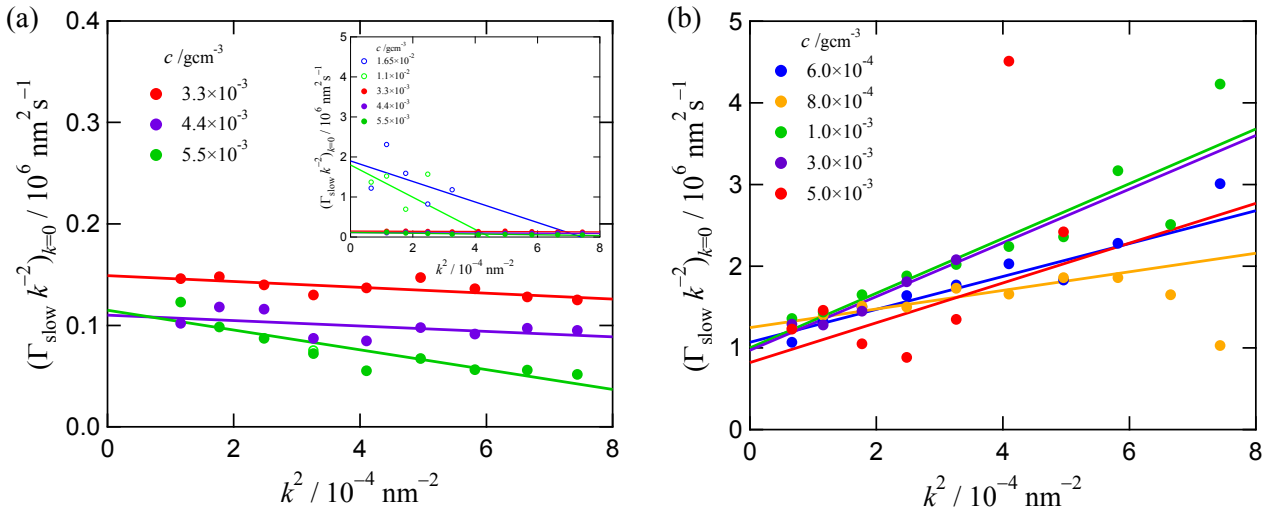

Figure II-A1. Plots of $\Gamma_{slow}k^{-2}$ against k^2 for aqueous Borax solutions of (a) the DPC–DOH mixture of $c_H/c_R = 0.1$ and of (b) DPC ($c_H/c_R = 0$), with different c.

References.

1) Phillips, J. N.; Mysels, K. J. *J. Phys. Chem*. **1955**, *59*, 325.

2) Princen, L. H.; Mysels, K. D. *J. Phys. Chem*. **1959**, *63*, 1781.

3) Zhu, Z.; Reed, W. F. *Langmuir*. **2013**, *29*, 10376.

4) Corti, M.; Degiorgio, V. *Chem. Pys. Lett.* **1977**, *49*, 141.

5) Konev, S. A.; Nikitin, V. V.; Olefirenko, G. I.; Yudin, I. K.; Zhuravleva, E. V. *Mol. Cryst. Liquid Cryst.* **1991**, *200*, 19.

6) Matsumura, S.; Kataoka, K. *Cancer Sci*. **2009**, *100*, 572.

7) Kataoka, K.; Harada, A.; Nagasaki, Y. *Adv. Drug. Deliv. Rev*. **2001**, *47*, 113.

8) Yang, Y. Q.; Zheng, L. S.; Guo, X. D.; Qian, Y.; Zhang, L. J. *Biomacromolecules*. **2011**, *12*, 116.

9) Sanada, Y.; Akiba, I.; Sakurai, K.; Shiraishi, K.; Yokoyama, M.; Mylonas, E.; Ohta, N.; Yagi, N.; Shinohara, Y.; Amemiya, Y. *J. Am. Chem. Soc*. **2013**, *135*, 2574.

10) Bae, Y.; Nishiyama, N.; Fukushima, S.; Koyama, H.; Matsumura, Y.; Kataoka, K. *Bioconjugate Chem*. **2005**, *16*, 122.

11) Wassenius, H.; Nyden, M.; Vincent, B. *J. Colloid. Interface. Science*. **2003**, *264*, 538.

12) Miyake, M.; Asano, A.; Einaga, Y. *J. Phys. Chem. B*. **2008**, *112*, 4648.

13) Ochi, M.; Matsue S.; Einaga, Y. *Polym. J*. **2008**, *40*, 442.

14) Paillet, S.; Grassl, B.; Desbrieres, J. *Anal. Chim. Acta.* **2009**, *636*, 236.

15) Sorci, G. A.; Walker, T. D. *Langmuir.* **2005**, *21*, 803.

16) Kanao, M.; Matsuda, Y.; Sato, T. *Macromolecules*. **2003**, *36*, 2093.

17) Dezelic, G.; Vevra, J. *Croat. Chem. Acta*. **1966**, 38, 35.

18) Hashidzume, A.; Kawaguchi, A.; Tagawa, A.; Hyoda, K.; Sato, T. *Macromolecules*. **2006**, *39*, 1135.

19) Fujio, K.; Ikeda, S. *Bull. Chem. Soc. Jpn*. **1992**, *65*, 1406.

20) van Os, N. M.; Haak, J. R.; Rupert, L. A. M. *Physico-Chemical Properties of Selected Anionic, Cationic and Nonionic Surfactants*; Elsevie. **1993**.

21) Grillo, I.; Penfold, J. *Langmuir*. **2011**, *27*, 7453.

22) Bergström, L. M.; Skoglund, S.; Danerlöv, K.; Garamus, V. M.; Pedersen, J. S. *Soft Matter.* **2011**, *7*, 10935.

23) Kaler, E. W.; Herrington, K. L.; Murthy, A. K.; Zasadzinski, J. A. N. *J. Phys. Chem.* **1992**, *96*, 6698.

24) Bergström, L. M.; Skoglund, S.; Edwards, K.; Eriksson, J.; Grillo, I. *Langmuir.* **2013**, *29*, 11834.

25) Sato, T.; Tanaka, K.; Toyokura, A.; Mori, R.; Takahashi, R.; Terao, K.; Yusa, S. *Macromolecules*. **2013**, *46*, 226.

26) Israelachvili, J. N. *Intermolecular and Surface Force* 2nd ed; Academic Press. **1992**

Chapter III.

Structure of Hydrophobe-Uptake Micelles Composed of an Amphiphilic Alternating Copolymer in Aqueous Solution

III-1. Introduction.

As demonstrated by Kawata et al.[1], Tominaga et al.[2], and Ueda et al.[3], polymer micelles formed in aqueous solutions of amphiphilic random and alternating copolymers have a much more complex structure than the spherical micelle formed by low molar mass surfactants. In particular, the polymer micelles have hydrophobic groups outside the hydrophobic core, which construct an intermingled domain with the main-chain and electrolyte groups.

The aim of this Chapter is to elucidate how the above difference in the structure between the low molar mass and polymer micelles affect the hydrophobe-uptake behavior. The preceding chapter demonstrated that spherical micelles composed of low molar mass surfactants include hydrophobes in the hydrophobic core of the micelles. Since the structure of the polymer micelle is much more complex, the hydrophobe may be included in the domain outside the hydrophobic core. I investigated the structure of the hydrophobe-uptake polymer micelle by static and dynamic light scattering as well as small angle X-ray scattering.

III-2. Experimental Section.

III-2-1. Materials.

Maleic anhydride was recrystallized from chloroform. Dodecyl vinyl ether was distilled under reduced pressure. Tetrahydrofuran (THF) for polymerization solvent was distilled over calcium hydride under ordinary pressure. Sodium tetraborate decahydrate (Borax) and 1-dodecanol (DOH) were purchased from Wako Pure Chemical Industries, Ltd,

and used without further purification. Water was purified with a Millipore Milli-Q system, which was used as solvent of test solutions.

III-2-2. Polymerization of MAL/C12 Copolymer.

Alternating copolymer sodium maleate and dodecyl vinyl ether (MAL/C12, Scheme III-1) was polymerized by same manner with previous researches[3-5]. Maleic anhydride, dodecyl vinyl ether, and 2,2′-azobis(isobutyronitrile) were dissolved in THF under argon atmosphere in a flask equipped with a three-way stopcock. The flask was immersed in an oil bath thermostate at 56 ºC with stirring for 36 hour. The reaction mixture was poured into a large excess of methanol to precipitate the copolymer.

Obtained copolymer sample was divided into five fractions by successive fractional precipitation using acetone and acetonitrile as the solvent and precipitant, respectively. Three fractions except the first and the last one in the five fractions were selected as useful sample for this research. In this Chapter, I report the result for only the middle fraction in the selected three fractions. The weight-average molar mass and the ratio of weight and number-average molar mass $M_{w,1}/M_{n,1}$ for this fraction were determined by size exclusion chromatography equipped a multi-angle light scattering detector (SEC-MALS) in THF solution. Because this fraction was in anhydride form here, the weight-average molar mass $M_{w,1}$ of MAL/C12 copolymer (hydrolyzed form) was calculated using the obtained value by the SEC-MALS measurement. The polymerization degree $N_{w,1}$ is calculated by $N_{w,1} = M_{w,1}/M_0$, where the molar mass M_0 of a monomer is an averaged value (= 186 g mol^{-1}).

This fraction was then hydrolyzed with 1.0 M aqueous NaOH in THF. Finally, the hydrolyzed MAL/C12 copolymer was purified by dialysis against water for seven days, and recovered by freeze-drying.

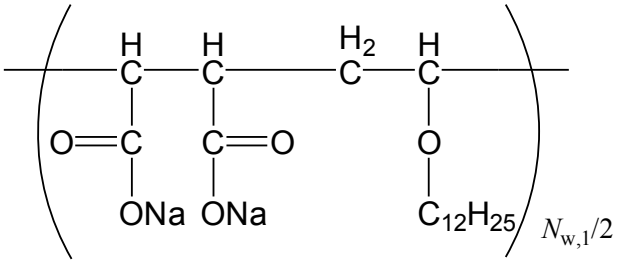

Scheme III-1. Chemical structure of the MAL/C12 copolymer

Table III-1. Molecular characterization of MAL/C12 copolymer used in this thesis.

$M_{w,1}$ / g mol^{-1}	$N_{w,1}$	$M_{w,1}$ / $M_{n,1}$
4.5×10^4	240	1.1

*Determined by SEC-MALS measurement for anhydride form in THF solution with the specific refractive index increment $\partial n/\partial c$ = 0.081 cm^{3}g^{-1} (at 633nm).

III-2-3. Preparation of Test Solution.

Test solutions were prepared in the following manner. MAL/C12 copolymer and neat DOH were mixed at the weight ratio of DOH to MAL/C12, c_H/c_R. The MAL/C12–DOH mixture was dissolved in pure water at 90 ºC for 15 minutes. This solution was then mixed with 50 mM aqueous Borax solution by 1:1 volume ratio to prepare the MAL/C12–DOH solution with 25 mM Borax, and stirred overnight after heated at 90 ºC for 5 minutes. Original solutions were prepared at $c_R = 5.0\times10^{-3}$ g cm^{-3} for each c_H/c_R, and then diluted with 25mM aqueous Borax to prepare test solutions of different concentrations. An upper limitation of DOH content was $c_H/c_R = 0.3$ in this study, because the solution was insoluble at the higher c_H/c_R than 0.3. In this study, the mass concentrations of MAL/C12 and of DOH are represented by c_R and c_H, respectively, and the total mass concentration is represented by c (= $c_R + c_H$). The subscripts R and H indicate the MAL/C12 and DOH, respectively.

III-2-4. Light Scattering Measurements.

Simultaneous static and dynamic light scattering (SLS and DLS) measurement was carried out for the test solutions in the same manner with that of Chapter II (cf. II-2-3 and II-2-4). An analysis of the light scattering measurement also followed the same manner with that of Chapter II (cf. II-2-5).

III-2-5. Small Angle X-ray Scattering (SAXS) Measurement.

SAXS measurement was carried out for the aqueous MAL/C12–DOH solutions (c_R = 1.0×10^{-3} g cm^{-3}) of c_H/c_R = 0, 0.1, 0.2, 0.3 at 25°C, using the BL-10C beamline in KEK-PF (Ibaraki, Japan). The wavelength, the camera length and accumulation time were chosen to be 0.15 nm, 2050 mm and 180 s, respectively. The intensity of the scattered X-ray was measured using an imaging plate detector.

The excess scattering intensity $I(k)$ was determined by using intensity of each solution was calculated by subtracting solvent intensity from the solution one.

III-3. Results.

III-3-1. Light Scattering Results.

Figure III-1 displays relaxation time spectra $A(\tau)$ of the intensity autocorrelation function $g^{(2)}(t)$ obtained by DLS measurements for MAL/C12-DOH solutions having various c_H/c_R at $c_R = 3.0\times10^{-3}$ g cm^{-3}. Unfilled and filled symbols represent the $A(\tau)$ at 30° and 60°, respectively. The fast and slow mode peaks are observed at $k^2\tau \sim 10^{-10}$ m^{-2}s and $k^2\tau \sim 2\times10^{-11}$ m^{-2}s for all c_H/c_R, indicating that the size of the slow relaxation component is much larger than that of the fast one. The magnitude ratios of the fast to the slow mode depend on the scattering angle, and the slow modes at $c_H/c_R \leq 0.1$ are disappeared at $\theta \geq 60°$. Similar spectra were observed for all c_R examined in this study ($1.0\times10^{-3} \leq c_R$ / g cm$^{-3} \leq 5.0\times10^{-3}$). This

concentration independence is a contrast to the case of the low molar mass surfactants - DOH mixture solutions argued in the previous Chapter (cf. Figure II-3). Because the CMC of amphiphilic polymers may be much lower than those of low molar mass surfactants, the anomalous scattering mentioned in Chapter II may not be observed in this system.

Using eq II-5, the first cumulants Γ for the fast and slow relaxation components were determined from $A(\tau)$. For $c_H/c_R \leq 0.1$, the slow component is not considered, because the slow modes are observed at a few data points in the low angle region. In Figure III-2, Γk^{-2} extrapolated to the magnitude of scattering vector $k = 0$ for both components are plotted against concentration c. Although data points for $\Gamma_{slow}k^{-2}$ are slightly scattered, all c dependences of $\Gamma_{fast}k^{-2}$ and $\Gamma_{slow}k^{-2}$ are so weak, that the hydrodynamic radii of the fast and slow relaxation components, $R_{H,fast}$ and $R_{H,slow}$ were estimated by extrapolation to $c = 0$ without difficulty. Table III-2 and III-3 lists the results of $R_{H,slow}$ and $R_{H,fast}$ respectively at various c_H/c_R.

Figure III-3 shows k^2 dependences of $(Kc/R_\theta)^{1/2}$ for MAL/C12-DOH solutions of $c_H/c_R = 0$ and 0.2 with different c. The angular dependence for the solutions of $c_H/c_R = 0.2$ is quite strong especially at low k, which come from the slow relaxation component appearing in $A(\tau)$ in Figure III-1. Using $A(\tau)$ shown in Figure III-1, I divided the excess Rayleigh ratio R_θ into the fast and slow components ($R_{\theta,fast}$ and $R_{\theta,slow}$; cf. eq II-2). For $c_H/c_R \leq 0.1$, $R_{\theta,slow}$ was not considered because of the negligibly small contribution of the slow relaxation component. The results of $R_{\theta,fast}$ and $R_{\theta,slow}$ for $c_H/c_R = 0$ and 0.2 are shown in Figure III-4.

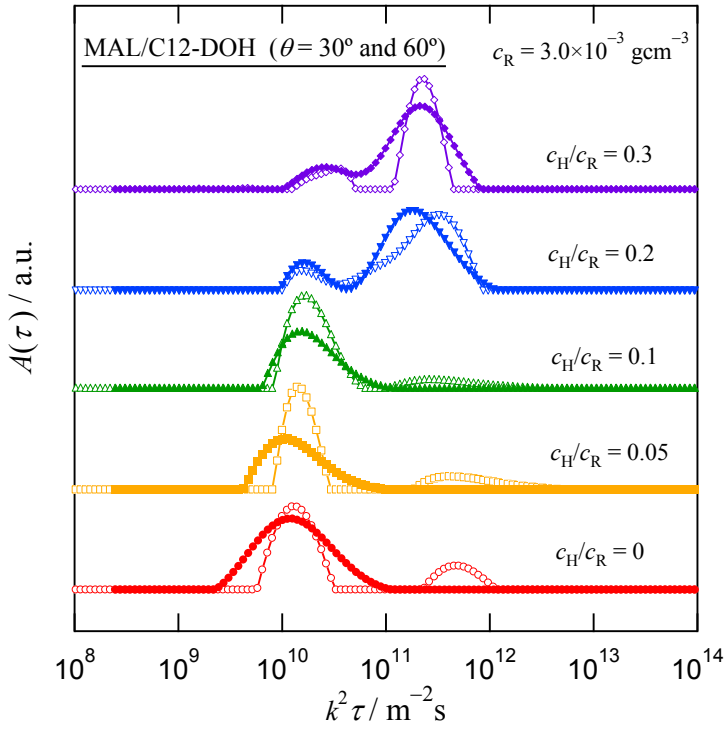

Figure III-1. Relaxation time spectra $A(\tau)$ of the intensity autocorrelation function $g^{(2)}(t)$ obtained by DLS measurements for aqueous Borax solution of MAL/C12-DOH mixtures. Unfilled and filled symbols represent $A(\tau)$ at 30° and 60°, respectively.

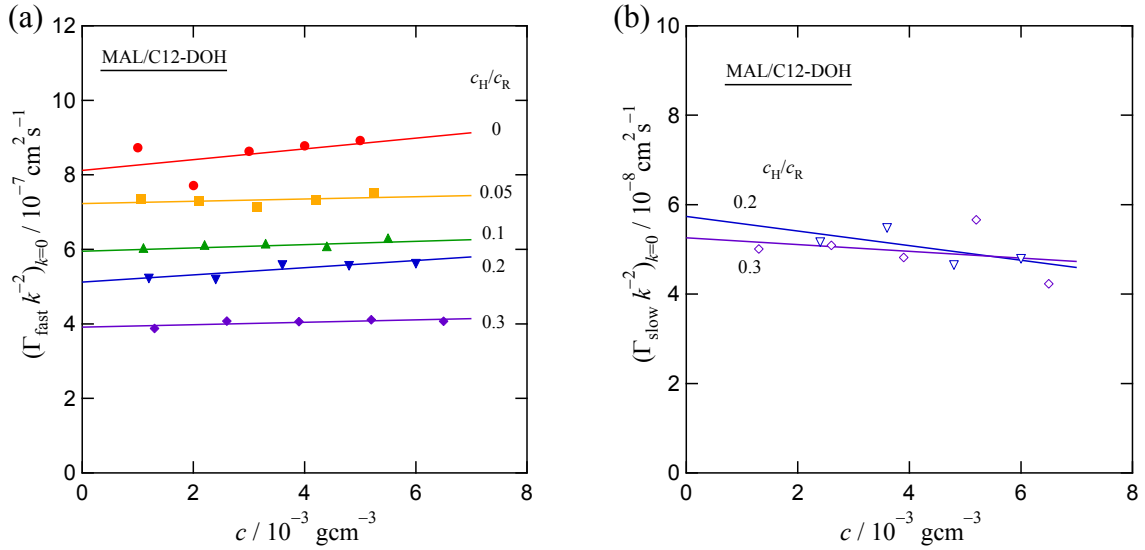

Figure III-2. Concentration dependence of the first cumulants Γ extrapolated to $k = 0$ for (a) the fast and (b) the slow relaxation components.

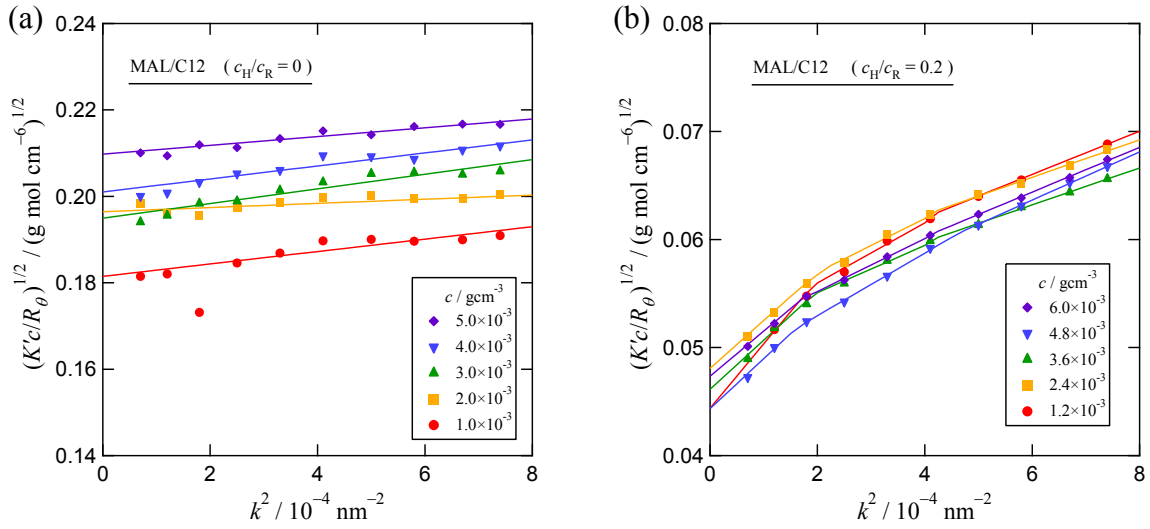

Figure III-3. Angular dependence of the excess Rayleigh ratio R_θ obtained by SLS measurement for (a) aqueous MAL/C12 Borax solution ($c_H/c_R = 0$), and (b) aqueous MAL/C12-DOH mixture Borax solution ($c_H/c_R = 0.2$).

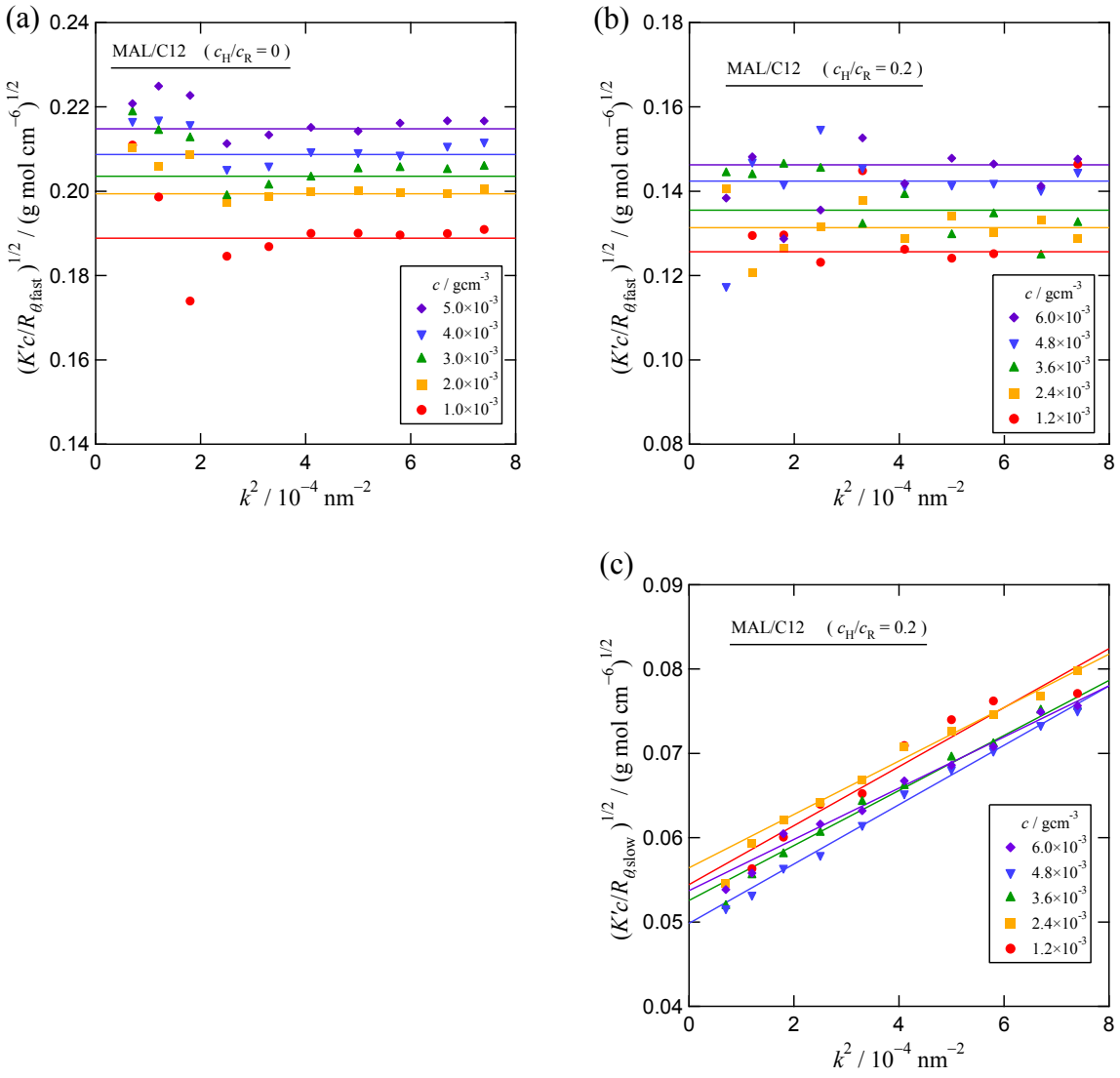

Figure III-4. Angular dependence of the $R_{\theta,fast}$ and $R_{\theta,slow}$. (a) $R_{\theta,fast}$ for aqueous Borax solutions of MAL/C12 (c_H/c_R = 0), (b) $R_{\theta,fast}$ for the aqueous Borax solutions of the MAL/C12-DOH mixture with c_H/c_R = 0.2, and (c) $R_{\theta,slow}$ for aqueous Borax solutions of the MAL/C12-DOH mixture with c_H/c_R = 0.2.

III-3-2. Slow Relaxation Component.

Hydrodynamic radii for the slow relaxation component $R_{H,slow}$ obtained from $\Gamma_{slow}k^{-2}$ shown in Figure III-2 are 43 and 47 nm for c_H/c_R = 0.2 and 0.3, respectively. If the micelle of

MAL/C12 could not include all DOH added, DOH may be dispersed as spherical colloidal particles in the solution. Assuming that the slow relaxation component is this spherical colloid of DOH, the molar mass of the slow relaxation component M_{slow} is estimated to be 1.7×10^8 and 2.2×10^8 g mol^{-1} by using the following equation when $R_{H,slow}$ = 43 nm and 47 nm, respectively.

$$M_{slow} = \frac{4\pi R_{H,slow}^3 N_A}{3\bar{\upsilon}_H} \qquad \text{(III-1)}$$

Here, $\bar{\upsilon}_H$ is the specific volume of DOH (=1.2 cm^{-3} g^{-1}). On the other hand, $w_{slow}M_{w,slow}$ is determined by extrapolating $(K'c/R_{\theta,slow})^{0.5}$ to k and c = 0 in Figure III-4(c) (cf. eq II-3(b)). Therefore, the weight fraction of the slow component is estimated to be $w_{slow} = 3.9\times10^{-3}$ and 8.6×10^{-3}, respectively. This means that the almost all DOH is included in the fast relaxation component. In the following discussion, I neglect the slow component, assuming w_{fast} (= 1 – w_{slow}) = 1.

Table III-2. Characteristics of the slow relaxation component in MAL/C12-DOH mixture solutions.

c_H/c_R	$R_{H,slow}$ / nm	$w_{slow}M_{w,slow}$ / g mol^{-1}
0.2	43	6.6×10^5
0.3	47	1.9×10^6

III-3-3. Fast Relaxation Component.

Angular dependences of $(K'c/R_{\theta,fast})^{0.5}$ shown in Figure III-4(a) and (b) are so weak that the extrapolation to the zero scattering angle can be made without difficulty. Figure III-5 shows concentration dependence of $(K'c/R_{0,fast})^{0.5}$ at k = 0 for different c_H/c_R. Because the CMC must be very low for polymer micelles, the c dependence may not be owing to changing

the average aggregation number but to the second virial term. I determined the weight-average molar mass $M_{w,fast}$ and the second virial coefficient A_2 of the fast component by using eq II-3(a). The weight average number of monomer units of MAL/C12 per micelle (N_w), the aggregation numbers of the MAL/C12 chains (m), and of DOH (n) can be determined from $M_{w,fast}$. The determined values and $R_{H,fast}$ are summarized in Table III-3. Both m and $R_{H,fast}$ increase, but A_2 decreases remarkably with increasing c_H/c_R. When A_2 is plotted against $M_{w,fast}$, one obtains a power law dependence of $A_2 \propto M_{w,fast}^{-1.7}$. The absolute value of the exponent is larger than those expected for the sphere (1), random flight chain (0.5), and rod (0), which indicates that the intermicellar interaction of the DOH uptake micelle becomes more attractive with increasing the DOH content.

In Figure III-6(a), $R_{H,fast}$ obtained for the hydrophobe-uptake micelles of MAL/C12-DOH in 0.025 M aqueous Borax are plotted against N_w (filled circles). With increasing c_H/c_R, both $R_{H,fast}$ and N_w increase, and the N_w dependence is stronger than that expected for the flower micelle model proposed previously (dashed line; see below). The data point at the smallest N_w for $c_H/c_R = 0$ deviates slightly downward from those of micelles composed of MAL/C12 and amphiphilic random copolymers of *N*-acryloyl-amino acids and *N*-dodecylmethacrylamide in 0.05 M aqueous NaCl, obtained previously.[1,3] This may be owing to the difference of the solvent condition.

Figure III-6(b) plots $R_{H,fast}$ for the DOH-uptake micelles of MAL/C12, DPC, and SDS against c_H/c_R (cf. Chapter II). While all the c_H/c_R dependences are similar, the micelle of MAL/C12 can include DOH more than those of the low molar mass surfactants. At $c_H/c_R >$ 0.1, DOH precipitates in the micellar solutions of the DPC-DOH and SDS-DOH mixtures, but the MAL/C12 micelle can still include DOH.

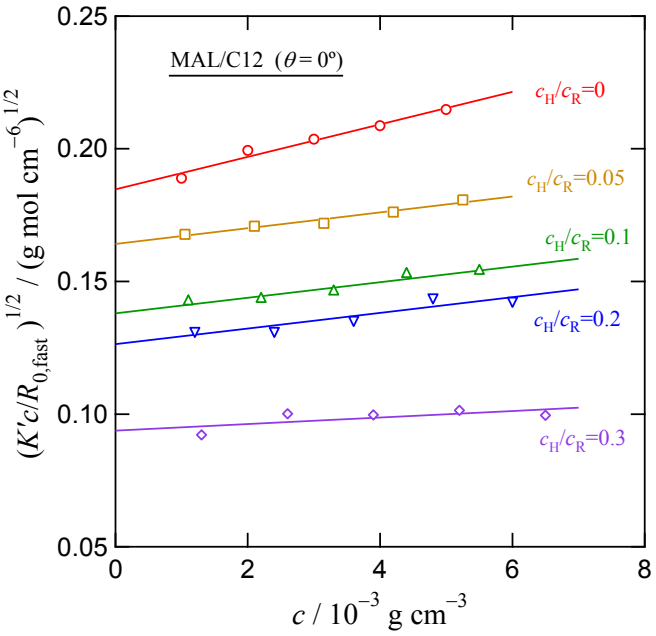

Figure III-5. Concentration dependence of $(K'c/R_{0,\mathrm{fast}})^{0.5}$ which is extrapolated to k = 0 for each c_H/c_R solutions.

Table III-3. Characteristics of the fast relaxation component in MAL/C12-DOH mixture solutions.

c_H/c_R	$M_{w,fast}$ / 10^4 g mol^{-1}	N_w	A_2 / 10^{-4} cm^3 g^{-2} mol	$R_{H,fast}$ / nm	m	n
0	5.9	317	5.6	3.0	1.3	0
0.05	9.6	384	2.4	3.4	1.6	19
0.1	11	523	2.0	4.1	2.2	52
0.2	13	578	1.8	4.8	2.4	120
0.3	24	980	0.53	6.3	4.1	290

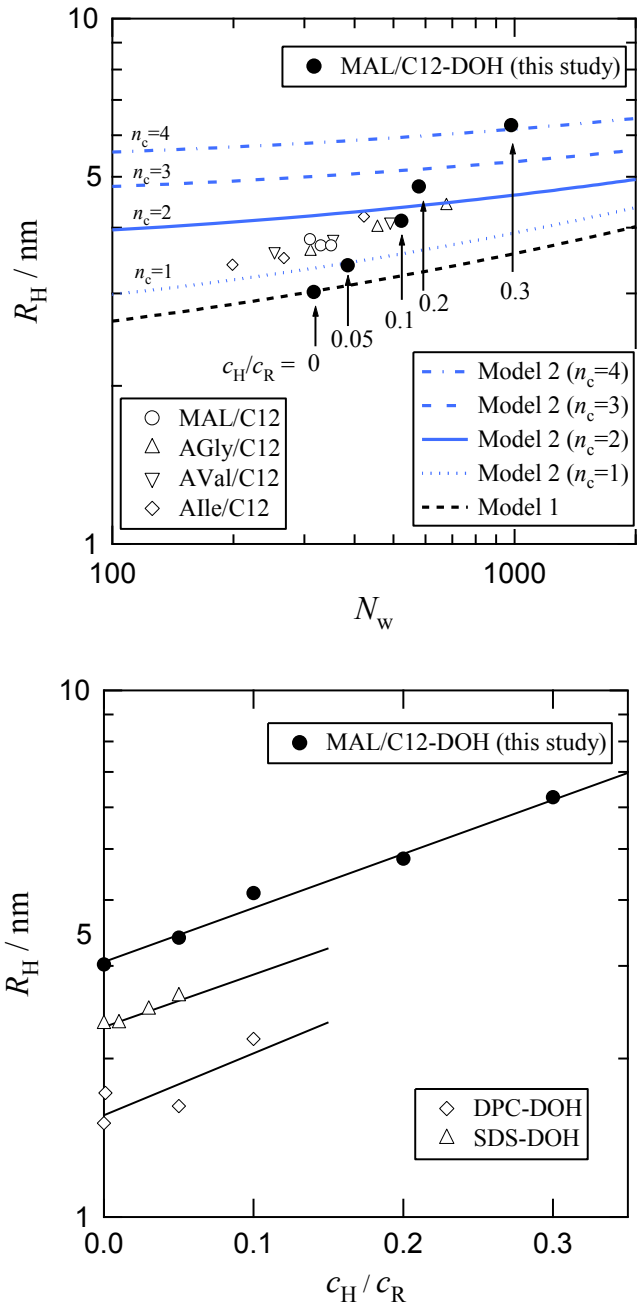

Figure III-6. (a) Plots of $R_{H,fast}$ vs. N_w for micelles composed of MAL/C12-DOH in 0.025 M aqueous Borax and of MAL/C12 and amphiphilic random copolymers of *N*-acryloyl-amino acids and *N*-dodecylmethacrylamide in 0.05 M aqueous NaCl.[1,3] The lines represent the theoretical values calculated for flower micelle models discussed later. (b) Plots of $R_{H,fast}$ vs. c_H/c_R for the hydrophobe-uptake micelles of MAL/C12, DPC and SDS in 0.025 M aqueous Borax.

III-3-4. SAXS Profiles.

SAXS profiles of the aqueous MAL/C12-DOH mixture solutions having various c_H/c_R at $c_R = 1.0\times10^{-3}$ g cm^{-3} are shown in Figure III-7. All profiles have a minimum and a maximum at ca. k = 1nm^{-1} and 1.5 nm^{-1}, respectively. These profiles resemble those for spherical micelles formed by low molar mass surfactants bearing a long alkyl group such as SDS, which have a hydrophobic core with a low electron density[6,7]. With increasing c_H/c_R, the magnitude of the scattering vector k at the minimum (pointed by arrows) slightly decreases, and the slope of the curves at the low k region increases. This indicates that the size of the micelle increases with increasing c_H/c_R, being consistent with $R_{H,fast}$ data mentioned above

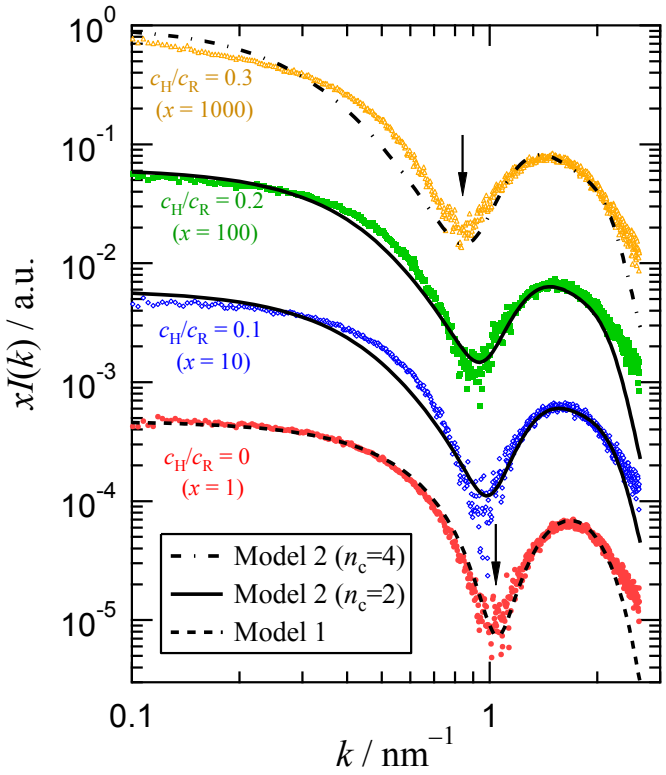

Figure III-7. SAXS profiles for 0.025 M aqueous Borax solutions of MAL/C12-DOH mixtures having various c_H/c_R at $c_R = 1.0\times10^{-3}$ g cm^{-3}. Broken, Solid, and dash-dot curves represent theoretical results calculated by Model 1 for c_H/c_R = 0, Model 2 with n_c = 2 for c_H/c_R = 0.1 and 0.2, and Model 2 with n_c = 4 for c_H/c_R = 0.3, respectively, which are explained in the Discussion section. Arrows point the minimums for the profiles at c_H/c_R = 0 and 0.3.

III-4. Discussion

III-4-1. Flower Micelle Model for the Micelle without the Hydrophobe-Uptake.

Kawata et al.[1] proposed the flower micelle model for random copolymers. Their model is composed a hydrophobic core and minimum-size loop chains (cf. Scheme I-2). The radius a of the hydrophobic core is calculated by

$$\frac{4}{3}\pi a^3 = m\lambda\upsilon\left(\frac{N_u h}{l_{loop}}+1\right). \qquad \text{(III-2)}$$

where m is the aggregation number of MAL/C12, λ is the number of hydrophobic side-chain induced in the core at each root of the loop, υ is the volume of the hydrophobe (= 0.35 nm^3 for the dodecyl group), N_u is the number of monomer units per unit flower, and h is the contour length per monomer unit (= 0.25 nm for vinyl polymers). The l_{loop} is the contour length of the minimum size loop of which ring closure probability abruptly increases. According to the wormlike chain statistics, l_{loop} and the distance d_{loop} from the root to top of the minimum loop are determined by the persistence length q of the main-chain

$$l_{loop} = 1.6q \qquad \text{(III-3)}$$

$$d_{loop} = 0.62q \qquad \text{(III-4)}$$

For polyelectrolytes of vinyl polymers, q was estimated to be ca. 3 nm at 0.05 mM of ionic strength.[3] The radius R_u of the flower micelle can be calculated from a and d_{loop} by

$$R_u = a + d_{loop}. \qquad \text{(III-5)}$$

A broken curve (Model 1) in Figure III-6(a) shows the N_u dependence of R_u calculated by eqs III-2 – III-5. When the experimental data of $R_{H,fast}$ for micelles formed in MAL/C12-DOH solutions are plotted against N_w in the same figure, it can be seen that the data point for c_H/c_R = 0 corresponds to the theoretical line for the flower micelle, but other c_H/c_R data points deviate upward from the broken curve.

Recently, Uramoto et al.[5,8] compared the scattering function obtained by SAXS for MAL/C12 in 25 mM aqueous Borax with that for the flower micelle. The scattering function for the flower micelle model can be calculated as follows.

The particle scattering function $P_u(k)$ of the flower micelle may be approximated to that of a concentric sphere where the inner and outer spheres correspond to the hydrophobic core and loop chains region, respectively. The scattering function $P_u(k)$ of the concentric sphere is calculated as

$$P_u(k) = \left[3 \frac{\tilde{\rho}_c (\sin ka - ka\cos ka) + \sin kR_u - kR_u \cos kR_u}{\tilde{\rho}_c (ka)^3 + (kR_u)^3} \right]^2 \qquad \text{(III-6)}$$

where

$$\tilde{\rho}_c = \frac{\rho_c - \rho_l}{\rho_l} \qquad \text{(III-7)}$$

with ρ_c and ρ_l being the excess electron densities of the core and loop regions, respectively. In eq III-6, $\tilde{\rho}_c$ in the inner and outer spheres are assumed to be independent of the radial distance as shown in the left part of Figure III-8.

The function $P_u(k)$ given by eq III-7 has sharp minima and the sharpness strongly depends on the dispersity of N_u. In order to taking the dispersity of N_u into account in the scattering function, I assume that this dispersity obeys the log-normal distribution, writing the weight fraction $w(N_u)$ of the micelle component.

$$w(x)dx = \frac{1}{\sqrt{\pi}} \exp(-x^2) dx$$
$$x \equiv \frac{\ln\left(N_u / \sqrt{N_{u,w} N_{u,n}}\right)}{2\ln\left(N_{u,w} / N_{u,n}\right)} \qquad \text{(III-8)}$$

Here, $N_{u,w}$ and $N_{u,n}$ are weight-average and number-average N_u, respectively. The z-average scattering function $P_{u,z}(k)$ is calculated as

$$P_{\mathrm{u,z}}(k) = \frac{\int w(N_{\mathrm{u}}) N_{\mathrm{u}} P_{\mathrm{u}}(k; N_{\mathrm{u}}) \mathrm{d}N_{\mathrm{u}}}{N_{\mathrm{u,w}}} \qquad \text{(III-9)}$$

where $P_{\mathrm{u,z}}(k;N_{\mathrm{u}})$ means $P_{\mathrm{u,z}}(k)$ at N_{u} calculated from eq III-6.

At last, the excess scattering intensity $I(k)$ is calculated by

$$I(k) \propto \frac{M_{\mathrm{w,fast}} P_{\mathrm{u,z}}(k)}{1 + 2A_{2,\mathrm{fast}} M_{\mathrm{w,fast}} P_{\mathrm{u,z}}(k) c}. \qquad \text{(III-10)}$$

The theoretical curve of $I(k)$ calculated using eqs III-2 – III-10 (Model 1) is shown in Figure III-7 for $c_{\mathrm{H}}/c_{\mathrm{R}} = 0$. Here, $N_{\mathrm{u,w}}$ was calculated from the result of the light scattering measurement ($N_{\mathrm{u,w}} = M_{\mathrm{w,fast}}/M_0$), and the same value of λ used in Figure III-6(a) ($\lambda = 1.2$) was selected. Therefore the fitting parameters are $\tilde{\rho}_{\mathrm{c}}$ and $N_{\mathrm{u,w}}/N_{\mathrm{u,n}}$. The Model 1 reproduces the experimental result of $c_{\mathrm{H}}/c_{\mathrm{R}} = 0$, which is same with the report of Uramoto et al.[5,8] Since the chosen $N_{\mathrm{u,w}}/N_{\mathrm{u,n}}$ are close to unity, the dispersity in N_{u} may not affect the calculation of R_{u} in Figure III-6(a). Therefore, both results of $R_{\mathrm{H,fast}}$ obtained by DLS and R_{u} by SAXS for $c_{\mathrm{H}}/c_{\mathrm{R}} = 0$ are consistently explained by the flower micelle model proposed by Ueda et al.[3]

III-4-2. Model for the Hydrophobe-Uptake Micelle.

If the hydrophobic core includes all additional hydrophobic molecules, the core size should be rewritten as follows, instead of eq III-2.

$$\frac{4}{3}\pi a^3 = m\lambda\upsilon\left(\frac{N_{\mathrm{u}} h}{l_{\mathrm{loop}}} + 1\right) + n_{\mathrm{u,H}}\upsilon_{\mathrm{H}} \qquad \text{(III-11)}$$

Here, $n_{\mathrm{u,H}}$ is the number of additional hydrophobic molecules per unit flower, υ_{H} is the molecular volume of the hydrophobic molecule. Using this equation instead of eq III-2 along with the other above equations and the parameter values of λ, $\tilde{\rho}_{\mathrm{c}}$ and $N_{\mathrm{u,w}}/N_{\mathrm{u,n}}$ chosen above, I calculated I(k) for $c_{\mathrm{H}}/c_{\mathrm{R}} = 0.2$, which is indicated by the thin broken curve in Figure III-9 (Model 1). The minimum of I(k) locates at k much lower than the experimental result. This

indicates that all DOH added to the MAL/C12 micellar solution are not included in the hydrophobic core of the micelle.

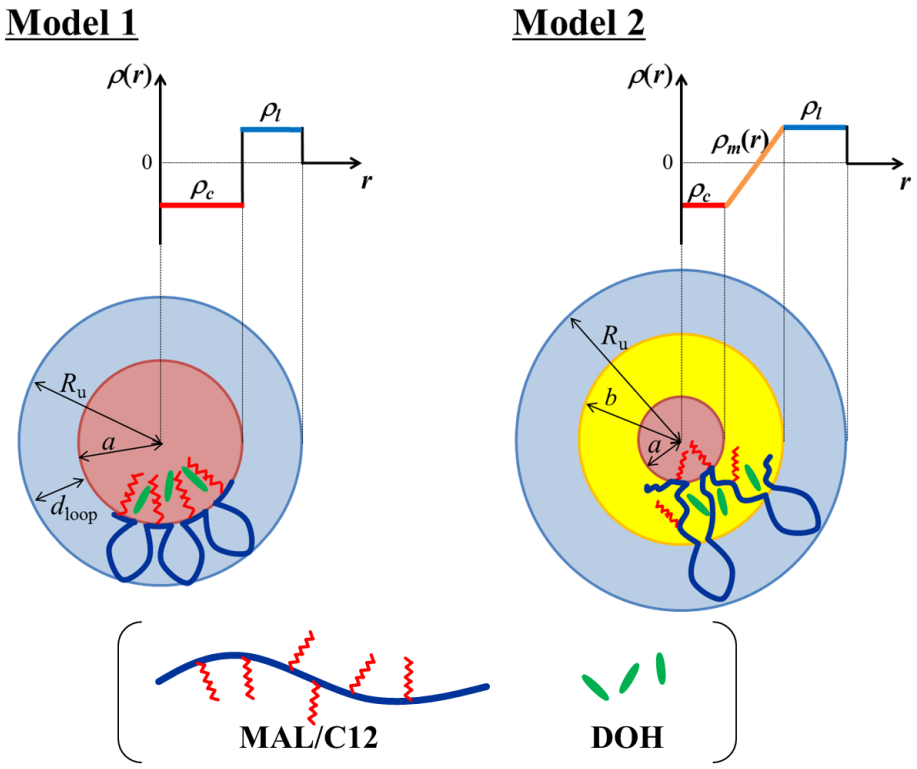

Figure III-8. Schematic description of the structure and the excess electron density of unit flower for each model. Here, $\rho(r)$ means the excess electron density at the radial distance r.

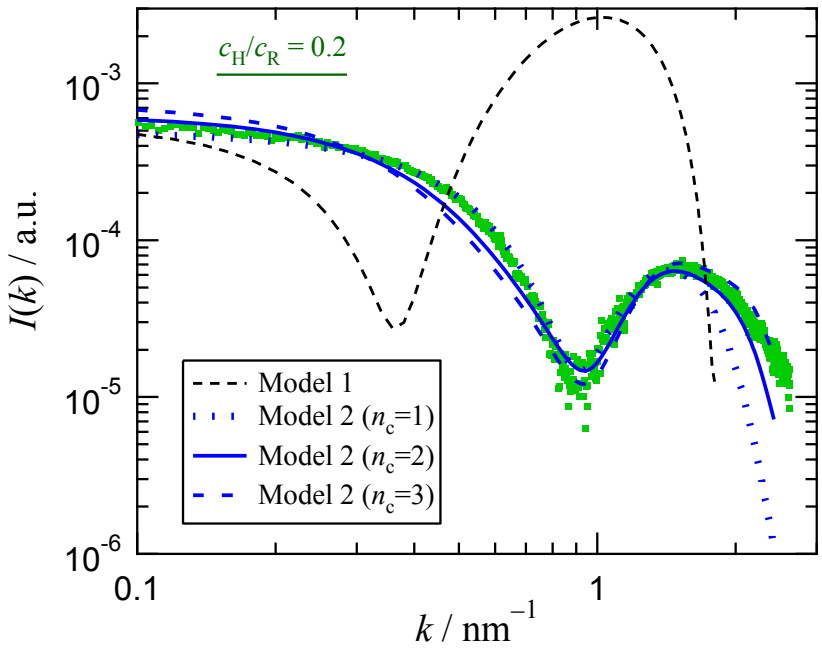

Figure III-9. SAXS profile of the DOH uptake micelle of MAL/C12 in 0.025 M aqueous Borax solution at c_H/c_R = 0.2 (c_R = 1.0×10^{-3} g cm^{-3}). The black broken curve represents theoretical value calculated by the theory of Models 1. The blue dotted, solid, and broken curves represent theoretical values calculated by the theories of Models 2 with n_c = 1, 2, and 3, respectively.

Tominaga et al.[2] made a molecular dynamics simulation for a flower micellar system for an amphiphilic random copolymer chain (cf. Figure I-2). According to their results, not all dodecyl groups distribute in the hydrophobic core region, but some dodecyl groups are outside the core, being intermingled with the main-chain and electrolyte groups, although such an intermingled domain was not necessary to consider to calculate $P_u(k)$ for the MAL/C12 micelle without DOH.

If DOH added to the MAL/C12 micellar solution is located in the intermingled domain of the micelle, this domain may have to be explicitly taken into account to calculate $P_u(k)$. Here, I utilize the following electron density profile.

$$\rho(r)=\begin{cases}\rho_{\mathrm{c}} & (0<r\le a)\\ \dfrac{\rho_l-\rho_{\mathrm{c}}}{b-a}r+\dfrac{\rho_{\mathrm{c}}b-\rho_l a}{b-a} & (a<r\le b)\\ \rho_l & (b<r\le R_{\mathrm{u}})\\ 0 & (r>R_{\mathrm{u}})\end{cases} \qquad \text{(III-12)}$$

which is depicted in Figure III-8. The scattering function $P_{\mathrm{u}}(k)$ for this electron density profile is given by

$$P_{\mathrm{u}}(k)\propto\left[\frac{\tilde{\rho}_{\mathrm{c}}}{k^3(b-a)}\left\{a\left(\sin ka+\frac{2\cos ka}{ka}\right)-b\left(\sin kb+\frac{2\cos kb}{kb}\right)\right\}+\frac{\sin kR_{\mathrm{u}}-kR_{\mathrm{u}}\cos kR_{\mathrm{u}}}{k^3}\right]^2 \qquad \text{(III-13)}$$

and the radius of the micelle R_{u} may be given by

$$R_{\mathrm{u}}=a+(b-a)+d_{\mathrm{loop}}=b+d_{\mathrm{loop}}. \qquad \text{(III-14)}$$

If suitable values for $b-a$, $\lambda, \tilde{\rho}_{\mathrm{c}}$, and $N_{\mathrm{u,w}}/N_{\mathrm{u,n}}$ were chosen for each $c_{\mathrm{H}}/c_{\mathrm{R}}$, it was possible to agree the minimum and maximum of $P_{\mathrm{u}}(k)$ calculated by eq III-13 with the experimental results, as shown in Figure III-9 by the dotted curve (Model 2, $n_{\mathrm{c}}=1$). However, R_{u} calculated by eq III-14 using the value of $b-a$ chosen was appreciably smaller than the experimental R_{H}, as shown in Figure III-6(a) by the dotted curve. To explain both the SAXS profile and R_{H} consistently, I utilized the multi-core flower necklace micelle model.

For the multi-core flower necklace with n_{c} hydrophobic cores, the scattering function may be calculated as follows, instead of eq III-10.

$$I(k)\propto\frac{M_{\mathrm{w,fast}}P_{\mathrm{u,z}}(k)P_{\mathrm{chain}}(k)}{1+2A_{2,\mathrm{fast}}M_{\mathrm{w,fast}}P_{\mathrm{u,z}}(k)P_{\mathrm{chain}}(k)c} \qquad \text{(III-15)}$$

Here, $P_{\mathrm{u,z}}(k)$ is the scattering function for the unit flower micelle, calculated from eq III-9 with $P_{\mathrm{u}}(k)$ from eq III-13, where a is determined by eq III-2 with $N_{\mathrm{u}}=N_{\mathrm{w}}/n_{\mathrm{c}}$. Then, $P_{\mathrm{chain}}(k)$ is the scattering function of the necklace chain. Approximating $P_{\mathrm{chain}}(k)$ by that for random flight chain,[9] I use the following equation.

$$P_{\text{chain}}(k) = \frac{n_c - 2\sigma - n_c\sigma^2 + 2\sigma^{n_c+1}}{[n_c(1-\sigma)]^2}$$
$$\sigma \equiv \frac{\sin(2kR_u)}{2kR_u} \qquad \text{(III-16)}$$

where R_u is estimated by eq III-14. For the touched bead model,[10] the bond angle must be larger than 60°, which is different from the random flight model, but this bond angle restriction may affect $P_{\text{chain}}(k)$ only in a low k region. The solid and dash-dotted curves in Figure III-9 indicate $I(k)$ for $c_H/c_R = 0.2$, calculated for the flower necklace models with $n_c = 2$ and 3, respectively. The adjustable parameters $b - a$, λ, $\tilde{\rho}_c$, and $N_{u,w}/N_{u,n}$ are listed in Table III-4. Both theoretical curves have minimum and maximum reasonably agreeing with the experimental result. Similar favorable fittings were obtained also for $I(k)$ at $c_H/c_R = 0.1$ and 0.3, and the fitting parameters selected are also listed in Table III-4. Thus, it is difficult to judge the number of hydrophobic cores n_c only from the SAXS results.

Ueda et al.[3] calculated the hydrodynamic radius R_H for the flower necklace model using the touched-bead wormlike chain model[10]. If n_c is equal to 2 or 3, meaning that the necklace is a dumbbell or trumbbell, R_H can be more easily calculated from the Kirkwood formula given by

$$R_H = n_c R_u \left[1 + \frac{2}{n_c} \sum_{i=1}^{n_c-1} (n_c - i) R_u \left\langle R^{-1}(2iR_u) \right\rangle \right]^{-1} \qquad \text{(III-17)}$$

where $\langle R^{-1}(L) \rangle$ is the mean reciprocal of the end-to-end distance of the chain with the contour length L. When n_c is equal to 4, the R_H is calculated by using the touched-bead wormlike chain model at persistence length q = 15 nm. The results are given by

$$R_H = \begin{cases} 1.33R_u & (n_c = 2) \\ 1.50R_u & (n_c = 3) \\ 1.80R_u & (n_c = 4) \end{cases} \qquad \text{(III-18)}$$

Here, the branch structure was not taken into account at $n_c = 4$.

The solid, broken and dash-dot curves in Figure III-6(a) indicate theoretical R_H for

the flower necklaces with n_c = 2, 3 and 4. The adjustable parameters n_c, $b - a$, λ, $\tilde{\rho}_c$, and $N_{u,w}/N_{u,n}$ are listed in Table III-4. The solid curve for n_c = 2 is close to the experimental data points for c_H/c_R = 0.1 and 0.2, and the dash-dot curve for n_c = 4 is close to that at c_H/c_R = 0.3. The theoretical $I(k)$ for c_H/c_R = 0.1 and 0.2 calculated with n_c = 2 and for c_H/c_R = 0.3 calculated with n_c = 4 are shown by solid and dash-dot curves in Figure III-7. From those fitting results shown in Figures III-7 and III-9, the flower necklace model is suitable to explain both experimental results of $I(k)$ and R_H consistently.

The values of $b - a$, λ, $\tilde{\rho}_c$, and $N_{u,w}/N_{u,n}$ selected to fit both $I(k)$ and R_H consistently are plotted against DOH content in Figure III-10. The thickness of the intermingled domain $b - a$ increases with increasing c_H/c_R. When a large amount of DOH ($c_H/c_R > 0.1$) is added to the solution, the micelle of MAL/C12 can include DOH in the intermingled domain, while the low molar mass surfactant micelle cannot include it so that DOH precipitates from the solution. The value of λ decreases with increasing c_H/c_R, indicating that more dodecyl groups of MAL/C12 move from the hydrophobic core to the intermingle domain with increasing the DOH content. With increasing c_H/c_R, $N_{u,w}/N_{u,n}$ increases remarkably, and $\tilde{\rho}_c$ decreases sharply, i.e., the size distribution of the hydrophobic core becomes broader, and the SAXS contrast of the core weaker.

The $N_{u,w}$ values calculated from experimental $M_{w,fast}$ and selected n_c are almost independent of c_H/c_R (Figure III-11). This means that the unit flower in the DOH uptake micelle has an optimum number of MAL/C12 monomer units.

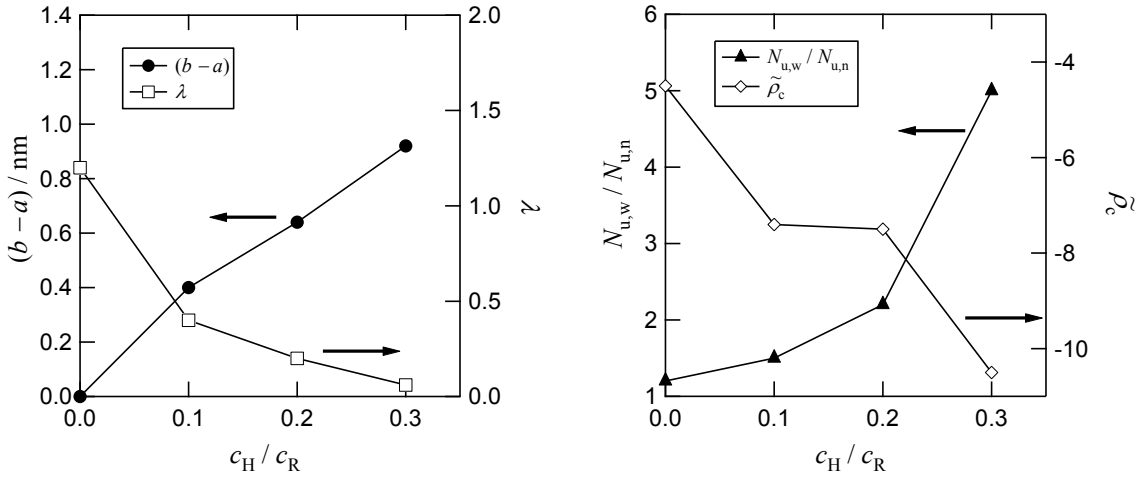

Figure III-10. DOH content dependence of the values of $b - a$, λ, $\tilde{\rho}_c$, and $N_{u,w}/N_{u,n}$ selected to fit both $I(k)$ and R_H consistently. These values are determined by Model 1 for $c_H/c_R = 0$, Model 2 ($n_c = 2$) for $c_H/c_R = 0.1$ and 0.2, and Model 2 ($n_c = 4$) for $c_H/c_R = 0.3$

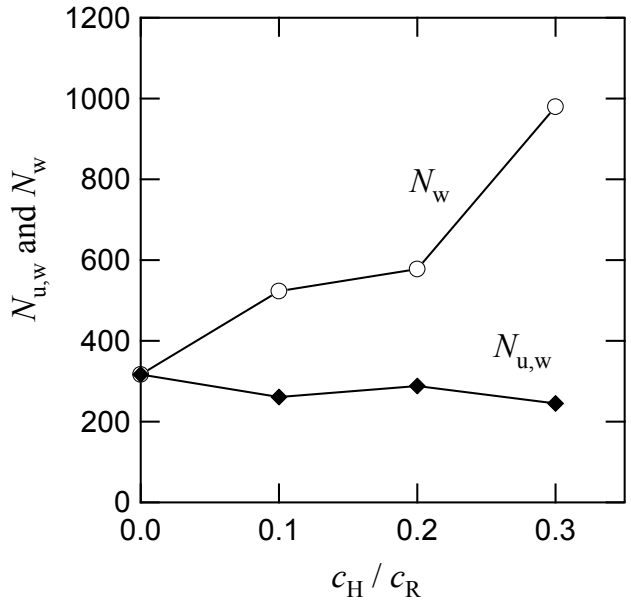

Figure III-11. DOH content dependence of the values of $N_{u,w}$ and N_w.

Table III-4. Values of parameters selected at fitting by the Model 1 for $c_H/c_R = 0$ and Model 2 for $c_H/c_R = 0.1 - 0.3$, respectively.

c_H/c_R	n_c	λ	$\tilde{\rho}_c$	$b - a$ / nm	$N_{u,w}/N_{u,n}$	R_H / nm
0	**1**	**1.2**	**–4.5**	**–**	**1.2**	**3.1**
0.1	1	0.50	–4.5	0.42	1.2	3.4
	2	**0.40**	**–7.4**	**0.40**	**1.5**	**4.2**
	3	0.30	–9.0	0.50	2.0	4.6
0.2	1	0.30	–4.5	0.65	1.7	3.6
	2	**0.20**	**–7.5**	**0.64**	**2.2**	**4.4**
	3	0.50	–6.0	0.75	1.7	5.2
0.3	1	0.15	–4.3	1.00	2.0	3.9
	2	0.1	–7.0	0.70	3.5	4.5
	3	0.085	–7.2	0.98	6.0	5.3
	4	**0.060**	**–10.5**	**0.92**	**5.0**	**6.0**

*When the parameters represented as dark columns are selected, the magnitude of R_H is consistent with the result of DLS, $R_{H,fast}$.

III-5. Conclusion.

I have investigated the structure of the DOH-uptake micelle composed of the alternating amphiphilic copolymer MAL/C12 in 0.025 M aqueous Borax solution, by SLS and DLS as well as SAXS. The flower micelle model which has the single core and the minimum-loop (Model 1) did not describe the SAXS profiles of solutions containing DOH. Then, I proposed the modified flower micelle model which has intermingled domain between the core and the loops (Model 2). This model reproduced the SAXS profiles. However, the calculated radius R_u of the uni-core micelle was considerably smaller than the hydrodynamic

radius R_H determined by DLS. Therefore, I utilized the multi-core flower necklace model. This model explained both R_H and SAXS results consistently. The DOH may be included in the intermingled domain of the unit flower. The spherical micelle of low molar mass surfactants, SDS and DPC, could include much less DOH than the micelle of MAL/C12. This may be due to that the spherical micelles of SDS and DPC do not possess the intermingled domain unlike the MAL/C12 micelle.

References.

1) Kawata, T.; Hashidzume, A.; Sato, T. *Macromolecules*. **2007**, *40*, 1174.
2) Tominaga, Y.; Mizuse, M.; Hashidzume, A.; Morishima, Y.; Sato, T. *J. Phys. Chem. B*. **2010**, *114*, 11403.
3) Ueda, M.; Hashidzume, A.; Sato, T. *Macromolecules*. **2011**, *44*, 2970.
4) Taura, D, Hashidzume, A.; Harada, A. *Macromol. Rapid. Commun*. **2007**, *28*, 2306.
5) Uramoto, K. *Master's Thesis of Osaka University*. 2013.
6) Zemb, T.; Charpin, P. *J. Physique*. **1985**, *46*, 249.
7) Barbosa, A. M.; Santos, I. J. B.; Ferreira, G. M. D.; Silva, M. C. H.; Teixeira, A. V. N. C.; Silva, L. H. M. *J. Phys. Chem. B.* **2010**, *114*, 11967.
8) Uramoto, K.; Terao, K.; Hashidzume, A.; Sato, T. to be submitted.
9) Kajiwara, K.; Burchard, W.; Gordon, M. *Br. Polym. J*. **1970**, *2*, 110.
10) Yamakawa, H. *Helical Wormlike Chain in Polymer Solutions*, Springer-Verlag, Berlin and Heidelberg. 1997

Chapter IV.

Laser Particle Tracking Rheometry to Measure High Frequency Linear Viscoelasticity

IV-1. Introduction.

It is difficult to measure high frequency linear viscoelasticity by conventional rheometry. To complement wideband linear viscoelastic data, microrheology is utilized recently. Data sampling rate is important factor for microrheology, and various methods for detection of Brownian motion of a particle have been proposed. Among them, the method using laser light can obtain linear viscoelastic data with high sampling rate, which is about 10^5 -10^6 Hz at most, depending on the performance of detector.[1-4] This method is called the Laser Particle Tracking (LPT) method. The LPT method tracks displacement of a probe particle. If Gaussian beam is used for the LPT measurement, the laser works as also optical tweezers. The optical tweezers trap a probe particle, and make it possible to measure for a long time.

The LPT rheometry were tried by several groups recently.[5-9] Although they succeeded to obtain high frequency data, their results were not accurate enough. Some viscoelastic results reported disagreed with the result from conventional rheometer,[5-7] and some reports used an inadequate equation for deriving viscoelastic modulus.[8,9] Their unsuccessful measurements were owing to underdevelopment of methodology for deriving viscoelastic function from the time dependence of the particle displacement. Considering their results, it is important to calibrate apparatus in an appropriate manner in order to obtain accurate viscoelastic data.

In this study, an appropriate methodology for calibration of the apparatus was developed considering a fluctuation of laser in addition to the theory of Brownian motion. This method was carried out by using standard pure viscose liquid. Furthermore, the accuracy

of the result of viscoelastic measurement for a viscoelastic sample was confirmed by comparison with results of conventional viscoelastic and birefringence measurements. Birefringence data, which is less affected by the mechanical resonance at high frequencies,[10] can be compared with viscoelastic data using stress optical rule (SOR).[11,12]

IV-2. Theoretical Background.

On the LPT rheometry, viscoelastic shear modulus $G^*(\omega) = G'(\omega) + iG''(\omega)$ is calculated by measuring displacement x of a particle embedded in a sample solution. First, a power spectrum density (PSD) $S(\omega)$ was calculated by the measured time dependence of displacement $x(t)$ via a autocorrelation function $C(\tau)$ of the displacement $x(t)$.

$$C(\tau) = \langle x(t)x(t+\tau) \rangle_t \tag{IV-1}$$

$$S(\omega) = 2\int_0^\infty C(\tau) e^{-i\omega\tau} d\tau \tag{IV-2}$$

Here, the imaginary part of $S(\omega)$ vanishes because $C(\tau)$ is an even function. According to the fluctuation-dissipation theorem,[13] the $S(\omega)$ is related to the response function $\alpha^*(\omega)$ [$= \alpha'(\omega) - i\alpha''(\omega)$] by the following equations.

$$\alpha''(\omega) = \frac{\omega}{2k_B T} S(\omega) \tag{IV-3}$$

$$\alpha'(\omega) = \frac{2}{\pi}\int_0^\infty \frac{\xi\alpha''(\omega)}{\xi^2 - \omega^2} d\xi \tag{IV-4}$$

Eq IV-4 was obtained from the Kramers-Kronig relation.[13,14]. The response function $\alpha^*(\omega)$ relates the complex Fourier transform $x(\omega)$ of $x(t)$ to the complex Fourier transform $f(\omega)$ of Brownian force $f(t)$ by

$$x(\omega) = \alpha^*(\omega) f(\omega). \tag{IV-5}$$

This eq IV-5 corresponds to the relation of the strain and stress for viscoelastic materials, and $\alpha^*(\omega)$ calculated by eqs IV-1–IV-4 is related to the complex modulus $G^*(\omega)$ for viscoelastic materials by the generalized Stokes-Einstein equation.[7]

$$G^*(\omega) = \frac{1}{6\pi r \alpha^*(\omega)} - G'_{\mathrm{trap}} \qquad \text{(IV-6)}$$

where r and G'_{trap} are the radius of a probe particle and the modulus of the optical trapping force, respectively. From eq IV-6, the real and imaginary parts of $G^*(\omega)$ [$=G'(\omega) + \mathrm{i}G''(\omega)$] are given by

$$G'(\omega) = \frac{1}{6\pi r}\left(\frac{\alpha'(\omega)}{\alpha'(\omega)^2 + \alpha''(\omega)^2}\right) - G'_{\mathrm{trap}} \qquad \text{(IV-7)}$$

$$G''(\omega) = \frac{1}{6\pi r}\left(\frac{\alpha''(\omega)}{\alpha'(\omega)^2 + \alpha''(\omega)^2}\right) \qquad \text{(IV-8)}$$

Thus, G^* can be determined by using eqs IV-1 – II-8 except for eq IV-5.

To avoid troublesome numerical calculations of IV-4, I applied the following method which is equivalent with calculations via eq IV-4. On one hand, experimental $S(\omega)$ is calculated from measured $x(t)$ using eqs IV-1 and IV-2. On the other hand, theoretical $S(\omega)$ is calculated from eq IV-3 with $\alpha''(\omega)$ which is estimated from eqs IV-7 and IV-8 by assuming appropriate G^*. If one use the generalized Maxwell model of which $G^*(\omega)$ is given by

$$G^*(\omega) = \sum_{j=1}^{k} \frac{G_j \tau_j \omega}{1 + i\tau_j \omega} + i\omega\eta_{\mathrm{s}} \qquad \text{(IV-9)}$$

(η_{s}: the solvent viscosity), the theoretical $S(\omega)$ can be calculated using k sets of the modulus G_j and the relaxation time τ_j (j = 1, 2, ⋯, k). The k sets of G_j and τ_j are determined by fitting the theoretical $S(\omega)$ to the experimental one. Inserting the sets of G_j and τ_j obtained into eq IV-9, one can determine G^* of the viscoelastic material where the probe particle is immersed.

IV-3. Experimental Section.

IV-3-1. Apparatus for LPT Measurements.

The block diagram of the custom-built apparatus for LPT measurements is illustrated

in Figure IV-1. An inversed optical microscope (IX71, Olympus, Ltd) was used to observe a probe particle. An infrared laser beam of the wavekength λ = 1064 nm (emitted from Compass 1064-4000M, Coherent, Inc) was illuminated on the probe particle via the microscope objective lens (UPLSAPO 100XO, N.A. = 1.40, Olympus, Ltd). The laser power was 500 mW. This laser worked as optical tweezers due to Gaussian beam.[15] The laser beam was condensed by the lens to trap the probe particle. Trapping of the particle enabled to measure the position of the particle during a long time. In this study, the laser beam was focused at 0.15 mm from the bottom surface of the sample cell, and the probe particle was trapped at this point, where the hydrodynamic effect from the bottom surface can be neglected.[16]

The laser beam also worked for tracing the position of a probe particle.[17] The motion of the particle changes the transmitted laser light intensity detected by a position-sensitive photodiode (s5990-01, Hamamatsu Photonics, Ltd). This system has dual detectors along x axis, and output the difference of intensity $I_1 - I_2$ detected by these detectors. The difference voltage $V(t)$ ($\sim I_1 - I_2$) was converted into digital data by A/D converter (WE7000, Yokogawa Electric Co.). The voltage $V(t)$ as a function of time t is proportional to the displacement x of the probe particle, [17] i.e.,

$$x(t) = \beta V(t) \tag{IV-10}$$

And the PSD $S(\omega)$ for $x(t)$ defined by eq IV-2 is expressed by

$$S(\omega) = \beta^2 S_0(\omega) = 2\beta^2 \int_0^\infty \langle V(t)V(t+\tau)\rangle_t \, \mathrm{e}^{-i\omega\tau} d\tau \tag{IV-11}$$

where β is a proportional constant which was determined using pure viscose liquids, water (purified by a Millipore Elix system) and ethylene glycol (Wako Pure Chemical Industries, Ltd.). The data of $V(t)$ were acquired at intervals of 0.1, 1, and 10 ms independently, and the final $S(\omega)$ was obtained by combining the data of the three intervals.

A viscoelastic solution containing polystyrene probe particles was placed on a

microscope slide with a hole and covered with a cover glass. This prepared slide was put upside-down on the stage of the microscope with a rubbery heater connected to a temperature controller. The measurements of $V(t)$ was carried out at 25 °C.

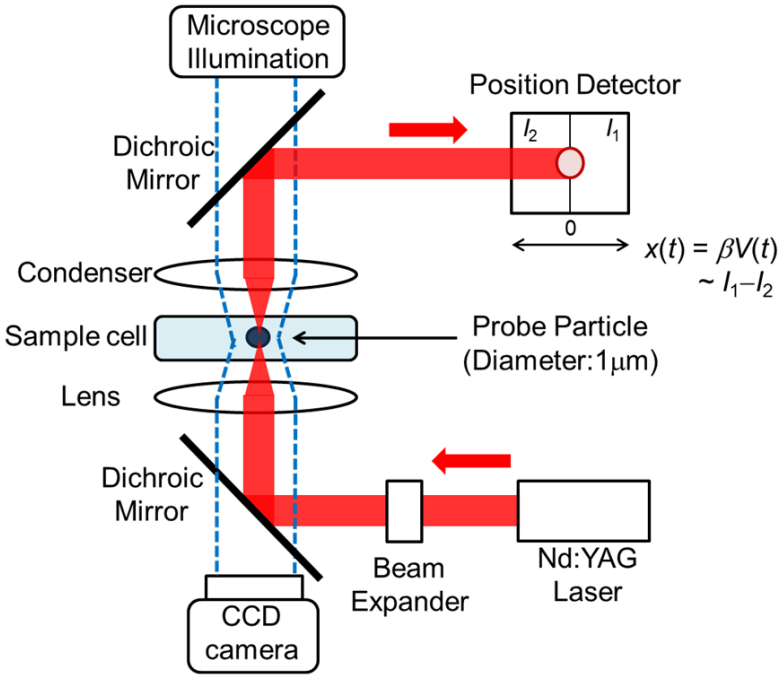

Figure IV-1. Block diagram of the apparatus for LPT rheometry

IV-3-2. Test Solution.

An aqueous solution of a mixture of cetyltrimethyl ammonium bromide (CTAB, Wako Pure Chemical Industries, Ltd.) and sodium salicylate (NaSal, Wako Pure Chemical Industries, Ltd.) was used as the standard viscoelastic sample CTAB was purified by the recrystallization method with acetone/methanol. NaSal was used without further purification after purchase. The mass concentrations of CTAB and NaSal were $c_D = 7.3\times10^{-3}$ g cm^{-3} and $c_S = 6.4\times10^{-3}$ g cm^{-3}, respectively. A tiny quantity, below 10^{-3} wt%, of carboxylate-modified polystyrene probe particles (diameter: 1.0μm, Molecular Probes, F8821) were dispersed in all the sample solutions for LPT measurement.

IV-3-3. Dynamic Viscoelastic and Shear Birefringence Measurements.

In order to confirm the validity of results of LPT measurements, linear viscoelastic and shear birefringence measurements were carried out on the same aqueous CTAB/NaSal solution without probe particles at 25 °C. The former and latter measurements were made with a conventional rheometer (MCR301, Anton Paar) equipped with a cone plate fixture having 25 mm diameter and a custom-built apparatus[10], respectively.

IV-4. Results and Discussion.

IV-4-1. PSD for Pure Viscose Liquids.

Figure IV-2 displays the result of t dependence of the output voltage $V(t)$, which is proportional to the displacement $x(t)$ of the probe particle. From these data, I obtained the PSD $S_0(\omega)$ for $V(t)$ (cf. eq IV-10 and IV-11). The results for H_2O and ethylene glycol are shown in Figure IV-3.

In pure viscose liquid, the Langevin equation for the probe particle is represented as

$$m\frac{d^2x(t)}{dt^2} = f(t) - \zeta\frac{dx(t)}{dt} - Kx(t) \qquad \text{(IV-12)}$$

where m and ζ are the mass and the friction coefficient of the particle, respectively, $f(t)$ is Brownian force, and K is the force constant of the optical tweezers (= $6\pi r G'_{\mathrm{trap}}$). The inertia term on the left hand side and $f(t)$ disappear after the time average. Hence this differential equation is solved as

$$\langle x(t+\tau)\rangle = \langle x(t)\rangle e^{-\tau/\lambda_{\mathrm{K}}} \qquad \text{(IV-13)}$$

where $\lambda_{\mathrm{K}} = \zeta/K$. Substituting eq IV-13 into eqs IV-1 and IV-2, $S(\omega)$ for pure viscose liquid is given by

$$S(\omega) = 2\left\langle x^2(t)\right\rangle_t \frac{\lambda_{\mathrm{K}}}{1+(\omega\lambda_{\mathrm{K}})^2} = \frac{2k_{\mathrm{B}}T\zeta}{K^2}\frac{1}{1+(\omega\lambda_{\mathrm{K}})^2} \qquad \text{(IV-14)}$$

The following law of equipartition of energy was used to obtain the last equation:

$$\frac{1}{2}k_{\mathrm{B}}T = \frac{1}{2}K\left\langle x^2(t)\right\rangle_t \qquad \text{(IV-15)}$$

Using eqs IV-11and IV-14, theoretical curves of $S_0(\omega)$ were drawn in Figure IV-3 (broken lines). This theoretical curve fits the experimental result well in $\omega > 10^2$ s^{-1}. However, the theoretical $S_0(\omega)$ deviates from experimental result in $\omega \leq 10^2$ s^{-1}.

I assumed that this deviation in the low frequency region was caused by fluctuation of the laser beam. In order to consider this effect, the equilibrium voltage $V_{\mathrm{F}}(t)$ is assumed to fluctuate with time. The origin of fluctuation $V_{\mathrm{F}}(t)$ may be the fluctuation of lase position or its power. In this case, experimentally detected voltage $V_{\mathrm{exp}}(t)$ can be written as

$$V_{\mathrm{exp}}(t) = V(t) + V_{\mathrm{F}}(t)\,. \qquad \text{(IV-16)}$$

Here, I assumed $<V_{\mathrm{F}}(t)> = <V(t)> = 0$. The experimentally observed PSD for voltage $S_{0,\mathrm{exp}}(\omega)$ can be calculated as follows using eq IV-16.

$$\begin{aligned} S_{0,\mathrm{exp}}(\omega) &= 2\int_0^\infty \left\langle V_{\mathrm{exp}}(t)V_{\mathrm{exp}}(t+\tau)\right\rangle_t \mathrm{e}^{-i\omega\tau}d\tau \\ &= 2\int_0^\infty \left\langle V(t)V(t+\tau)\right\rangle_t \mathrm{e}^{-i\omega\tau}d\tau + 2\int_0^\infty \left\langle V_{\mathrm{F}}(t)V_{\mathrm{F}}(t+\tau)\right\rangle_t \mathrm{e}^{-i\omega\tau}d\tau \\ &= S(\omega)/\beta^2 + S_{0,\mathrm{F}}(\omega) \end{aligned} \qquad \text{(IV-17)}$$

Here, The cross term is $<V(t)V_{\mathrm{F}}(t+\tau)> = 0$ because the fluctuation of laser beam has not correlation with thermal motion of a probe particle. Eq IV-17 means that the experimentally observed PSD $S_{0,\mathrm{exp}}(\omega)$ can be divided into PSD due to thermal motion $S_0(\omega)$ and fluctuation of laser $S_{0,\mathrm{F}}(\omega)$. If I assumes the $<V_{\mathrm{F}}(t)V_{\mathrm{F}}(t+\tau)>$ can be written with a single relaxation function, the $S_{0,\mathrm{F}}$ is calculated as follow.

$$\begin{aligned} S_{0,\mathrm{F}}(\omega) &= 2\int_0^\infty \left\langle V_{\mathrm{F}}(t)V_{\mathrm{F}}(t+\tau)\right\rangle_t \mathrm{e}^{-i\omega\tau}d\tau \equiv 2\int_0^\infty A\mathrm{e}^{-\tau/\lambda_{\mathrm{F}}}\mathrm{e}^{-i\omega\tau}d\tau \\ &= \frac{2A\lambda_{\mathrm{F}}}{1+\left(\omega\lambda_{\mathrm{F}}\right)^2} \end{aligned} \qquad \text{(IV-18)}$$

In Figure IV-3, the theoretical PSD $S_{0,\mathrm{exp}}(\omega)$ obtained by eqs IV-14, IV-17 and IV-18 is

displayed by solid curves. Selecting appropriate values for the parameters β, K, A and λ_F, I can fit the theoretical curves to the experimental result. Assuming that A and λ_F are same for H_2O and ethylene glycol, I determined the apparatus constant β and spring constant K of optical tweezers for each solvent by the fitting.

At $10^3 \leq \omega / s^{-1} \leq 10^4$, the experimental data disperses a little, and this does not reproduced by the theoretical curve. This phenomenon observed for all solutions equally. Although this reason is not obvious, this disperse was judged as a systematic error (such as intrinsic vibration of apparatus), which can be negligible because almost all data point was on the theoretical curve.

The determined β, K, A and λ_F for H_2O and ethylene glycol were summarized in Table IV-1. These values of β and K were different between H_2O and ethylene glycol. Trapping force of optical tweezers depends on refractive indexes for solution n_s and probe particles n_p, respectively.[17]

$$K \propto \frac{n_s\left(n_p^2 - n_s^2\right)}{n_p^2 + 2n_s^2} \qquad \text{(IV-19)}$$

According to this relation, a ratio of K for ethylene glycol to that for H_2O (K_{eth}/K_{H2O}) is estimated at $K_{eth}/K_{H2O} = 0.64$. This value almost agree with experimental value $K_{eth}/K_{H2O} = 0.60$. β depends on a beam width w_0 at trapping point, which is determined by refractive index of solvent n_s. Due to difficulty to obtain of the w_0 for this apparatus, I could not compare the value of experimental β with theoretical value.[17] However, the magnitude relation between H_2O and ethylene glycol is consistent.

As describe above, the determinations of β and K need the refractive indexes n_s and n_p. Therefore the values for dilute solutions can be determined by measurement for each solvent, because refractive index corresponds to that of solvent for dilute solutions. Furthermore, the fluctuation parameters A and λ_F of the laser beam are independent of

solvents. Hence, these parameters can be utilized for correction of data of any solutions.

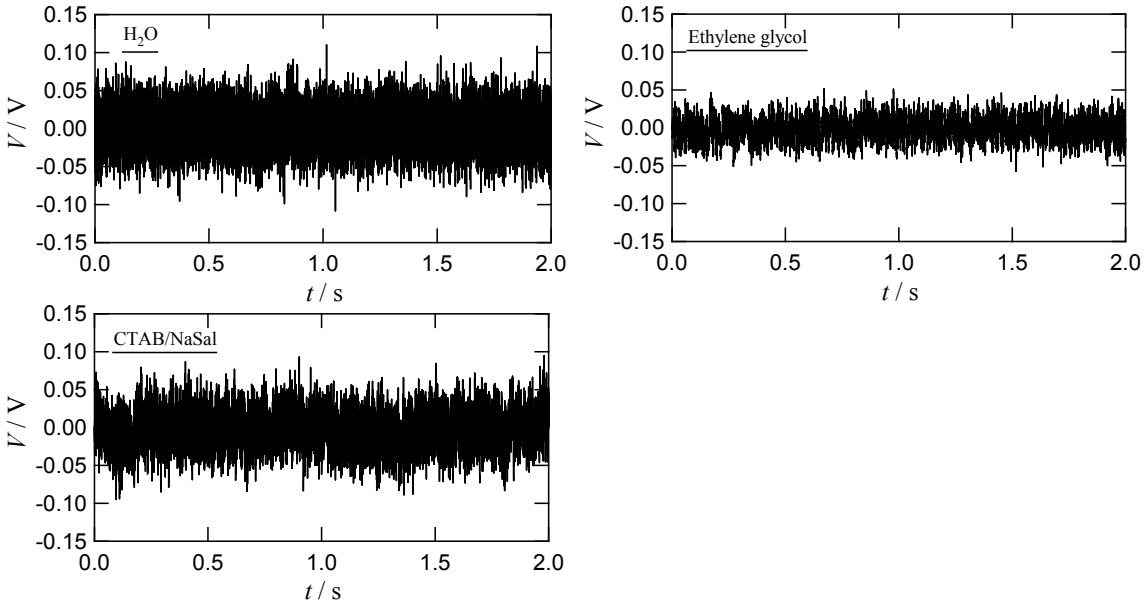

Figure IV-2. Time dependence of output voltage for H_2O, ethylene glycol, and CTAB/NaSal aqueous solution when sampling rate is 0.1ms.

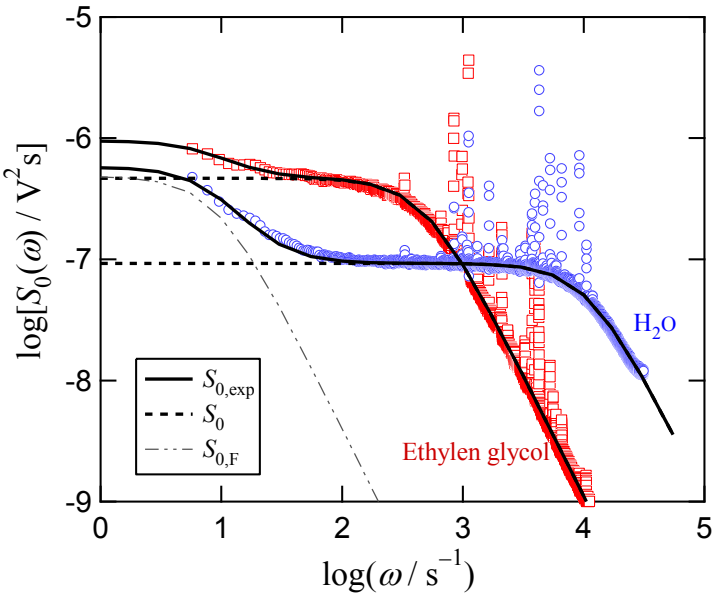

Figure IV-3. PSD of voltage for H_2O and ethyleneglycol. The thickest theoretical line is final theoretical curve $S_{0,exp}$ (eq IV-17). The broke line is theoretical PSD S_0 before considering fluctuation error (eqs IV-11 and IV-14). The thinnest dot-dash line is fluctuation term $S_{0,F}$ (eq IV-18).

Table IV-1. Determined apparatus constants β, K, A and λ_F.

Samples	β / m V^{-1}	K / N m^{-1}	A / V^2	λ_F / s
H_2O	3.0×10^{-7}	9.1×10^{-5}	2.2×10^{-6}	0.11
Ethylene glycol	7.2×10^{-7}	5.5×10^{-5}	2.2×10^{-6}	0.11

IV-4-2. LPT Measurement for Threadlike Micellar Solution.

CTAB/NaSal is well known to form threadlike micelles in aqueous solution and to show remarkable viscoelasticity.[18] The time dependence of $V(t)$ for an aqueous CTAB/NaSal solution was displayed in Figure IV-2. The PSD $S(\omega)$ for this solution was obtained by eqs IV-17 and 18 using the parameters β, A and λ_F determined for H_2O. The $S(\omega)$ is shown in Figure IV-4. This $S(\omega)$ deviates from a single relaxation, being different from that of H_2O. This is owing to the viscoelasticity of the solution, and the Langevin equation for this solution should be written as follow.[2]

$$m\frac{d^2x(t)}{dt^2} = f(t) - \int_{-\infty}^{t} \zeta(t-t')\frac{dx(t')}{dt}dt' - Kx(t) \qquad \text{(IV-20)}$$

Eq IV-20 is referred to as the generalized Langevin equation, which includes the delay friction function $\zeta(t)$ in the viscose term. This function $\zeta(t)$ includes information equivalent with G^*. In this study, I did not analysis $S(\omega)$ by using the eq IV-20 but the method mentioned in the theoretical background section via the generalized Maxwell model. The fitting curve of $S(\omega)$ obtained by eqs IV-3 and IV-6 – IV-9 is shown in Figure IV-4. Assuming appropriate parameters in eq IV-9, theoretical $S(\omega)$ was agreed with the experimental result successfully. Therefore complex modulus G^* for this sample is obtained by eq IV-9 using applied parameters.

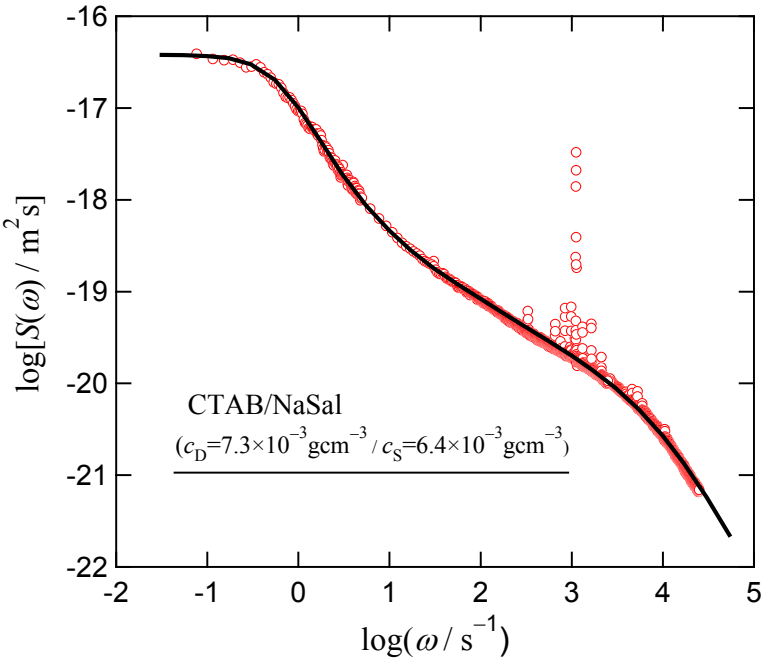

Figure IV-4. PSD for CTAB/NaSal aqueous solution.

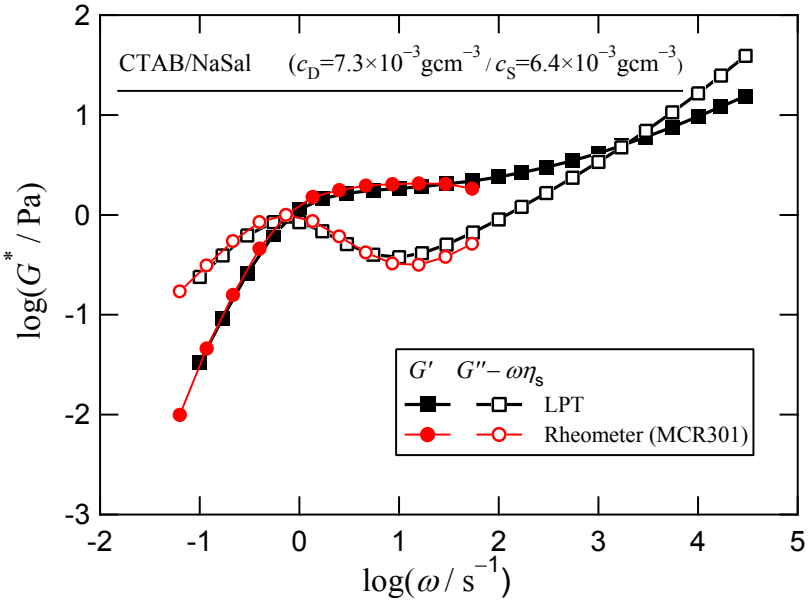

Figure IV-5. Complex modulus G^* for CTAB/NaSal aqueous solution measured by LPT and conventional rheometer.

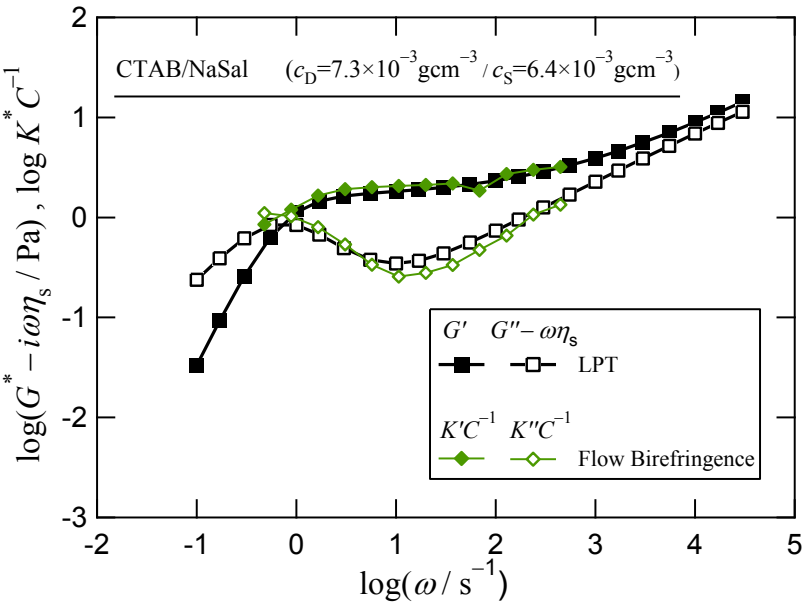

Figure IV-6. Complex modulus $G^*-i\omega\eta_s$ for CTAB/NaSal aqueous solution measured by LPT and the result of shear birefringence K^*C^{-1}.

The obtained complex modulus G^* was shown in Figure IV-5. The LPT rheometry serves the modulus over a wide frequency range which is same range of PSD. The G^* obtained by the LPT method agrees satisfactorily with the result by a conventional rheometer MCR 301. Because the rheometer has a resonance point at about $\omega \sim 50$ s^{-1} for this low viscoelastic solution, it was difficult to obtain G^* at $\omega > 50$ s^{-1} using this rheometer.

In order to confirm the accuracy of the LPT result in a wider frequency region, I compared the G^* of LPT with the result of birefringence measurement, which is affected less by the mechanical resonance at high frequencies (about $\omega < 1000$ s^{-1}) compared with MCR301. According to stress-optical rule (SOR) for polymer systems, the complex shear strain-optical coefficient K^* is proportional to G^*.[12] Using the stress optical coefficient C, I can write $K^* = CG^*$. In this study, I assume that the SOR holds for the threadlike micellar solution. The K^* measured by birefringence method for CTAB/NaSal solution was shown in Figure IV-6. Here, C was chosen to be -6.5×10^{-7} Pa^{-1}. The contribution of the solvent

viscosity η_s was subtracted from the G^* of LPT, because K^* does not include the contribution of solvent in this frequency region.[19] This $G^* - i\omega\eta_s$ corresponds well with K^*C^{-1} in $\omega < 500$ s^{-1}. Therefore, the result of LPT is reliable in this frequency region if the SOR is successful for threadlike micelle system.

Comparing spectra of LPT with the MCR 301 and the birefringence in Figure IV-5 and IV-6 carefully, the $G'' - \omega\eta_s$ disagree slightly in $15 \leq \omega / s^{-1} \leq 50$. Although this reason is not obvious, the result of the LPT rheometry might show an error in this region, because the tendency of disagreement is same between Figure IV-5 and IV-6. However, this disagreement was not observed for other solutions (cf Chapter V). Therefore, I judged that this slight disagreement is not significant and is owing to experimental error.

In the higher frequency region ($\omega > 500$ s^{-1}), the direct comparison with other measurement is difficult. However, the G^* in high frequency region ($\omega \geq 100$ s^{-1}) is reasonable qualitatively, because power-law relaxation behavior $G^* \sim a\omega^{0.5}$ which is similar to polymer system is observed. This power-law relaxation behavior indicates orientation relaxation of the sub-chain of threadlike micelle. Due to agreement of G'' with $K''C^{-1}$ of the power-law behavior in $100 \leq \omega / s^{-1} \leq 500$, it is reasonable that the exponent 0.5 of frequency dependence of G^* of LPT continues in also higher frequency region. Considering this, the quantitative accuracy of LPT measurement is sufficiently in high frequency region.

Here, I note the SOR for threadlike micelles. Actually, it have not been confirmed enough whether the SOR is satisfied for threadlike micelles in previous research. Similar birefringence research for CTAB/NaSal solution was carried out by using time dependence of flow birefringence.[20] In the time scale of their research ($t = 1/\omega > 0.3$ s), the SOR was satisfied for CTAB/NaSal solution. However, it has not been confirmed in the faster region. For example, other type of chain-like supramolecular is known to deviate from the SOR.[10] For this system, the viscoelasticity shows unique feature, which has two step relaxations. The two

relaxations (or one of them) are caused by specific behavior for the supramolecular, which is not observed for polymer system. The deviation from SOR for this supramolecular system is caused by two different values of C which the two relaxations have, respectively. Considering this, similar phenomenon can be observed for CTAB/NaSal system. However, CTAB/NaSal solution shows quite similar relaxation with polymer system except a single Maxwell relaxation in low frequency region. This indicates that the dynamics of threadlike micelle is very similar to polymer system. Therefore, it is reasonable that the SOR is satisfied for CTAB/NaSal system.

IV-5. Conclusion.

The apparatus for LPT rheometry was constructed using inversed microscope and Nd:YAG laser. The laser passing through an objective lens worked as optical tweezers which trapped an embedded probe particle in a solution. The displacement of the probe particle in sample solution was measured by using a divided photodiode. The power spectrum density (PSD) was calculated using the data of time dependence of the displacement of the particle.

Obtained PSDs for H_2O and ethylene glycol were analyzed by the Langevin equation for pure viscose liquid along with taking the fluctuation effect of laser into account, to obtain apparatus constants necessary for viscoelastic measurements. Moreover, I obtained viscoelastic modulus G^* for aqueous CTAB/NaSal solution over a wide frequency range ($10^{-1} \leq \omega / \mathrm{s}^{-1} \leq 3\times10^{4}$), using the generalized Maxwell model. The obtained G^* agreed with results measured by a conventional rheometer and also obtained from birefringence, confirming the reliability of the present LPT rheometer.

References.

1) Kimura, Y. *J. Phys. Soc. Jpn*. **2009**, *78*, 041005.

2) Mason, T. G.; Weitz, D. A. *Langmuir*. **1995**, *11*, 4256.

3) Crocker, J. C.; Grier, D. G. *J. Colloid Interface. Sci*. **1996**, *179*, 298.

4) Weeks, E. R.; Crocker, J. C.; Levitt, A. C.; Schofield, A.; Weitz, D. A. *Science*. **2000**, *287*, 627.

5) Buchanan, M.; Atakhorrami, M.; Palierne, J. F.; MacKintosh, F. C.; Schmidt, C. F. *Phys. Rev. E*. **2005**, *72*, 011504.

6) Pesce, G.; De Luca, A. C.; Rusciano, G.; Netti, P. A.; Fusco, S.; Sasso, A. *J. Opt. A: Pure Appl. Opt.* **2009**, *11*, 034016.

7) Schnurr, B.; Gittes, F.; MacKintosh, F. C.; Schmidt, C. F. *Macromolecules.* **1997**, *30*, 7781.

8) Yao, A.; Tassieri, M.; Padgett, M.; Cooper, J. *Royal Chem. Soc*. **2009**, *9*, 2568.

9) Pesce, G.; Sasso, A. Fusco, S. *Rev. Sci. Instr.* **2005**, *76*, 115105.

10) Hayashi, C.; Inoue, T. *Nihon Reoroji Gakkaishi.* **2009**, *37*, 205.

11) Doi, M.; Edwards, S. F.; *The Theory of Polymer Dynamics*. Clarendon: Oxford, **1986**.

12) Inoue, T. Uematsu, T. Osaki, K. *Macromolecules*. **2002**, *35*, 820.

13) Hayakawa, R.; Ito, K.; Kimura, Y.; Okano, K. *Hiheikoukei no Dainamikusu Nyumon*. Baihusya. **2006**.

14) Landau, L. D.; Lifshitz, E. M. *Statistical Physics*, 3rd ed. Pergamon Press. **1963**.

15) Ashkin, A.; Dziedzic, J. M.; Bjorkholm, J. E.; Chu, S. *Opt. Lett.* **1986**, *11*, 288.

16) Brizard, M.; Megharfi, M.; Mahé, E.; Verdier, C. *Rev. Sci. Instr.* **2005**, *76*, 025109.

17) Gittes, F.; Schmidt, C. F. *Opt. Lett.* **1998**, *23*, 7.

18) Shikata, T.; Hirata, H.; Kotaka, T. *Langmuir*. **1987**, *3*, 1081.

19) Ferry, J. D. *Viscoelastic Properties of Polymers*, 3rd ed.Wiley: New York. **1980**.

20) Shikata, T.; Dahman, S. J.; Pearson, D, S. *Langmuir*. **1994**, *10*, 3470.

Chapter V.

High Frequency Viscoelastic Measurements of Threadlike Micelles Composed of Nonionic and Cationic Surfactants in Aqueous Solutions

V-1. Introduction.

Threadlike micellar solutions have unique viscoelastic relaxation behavior,[1-13] which is characterized by two characteristic times. The first characteristic time is the rotational relaxation time τ_d of the whole micelle. If the dynamics of a threadlike micelle having contour length L could be regarded as that of a Gaussian chain, for example, $\tau_d \sim L^2$ is expected from the Rouse theory[14-17] for non-entangled systems, and $\tau_d \sim L^3$ from the tube theory[16,17] for entangled systems. The second characteristic time is the life time of micelles τ_{life} which is determined by the dynamic equilibrium of the breakage and reformation of micelle. Cates showed that if a threadlike micelle can break out with a fixed probability per unit length anywhere along its contour length L, $\tau_{life} \sim L^{-1}$.[11] This means that longer micelles have shorter life times. The important point is the two characteristic times (τ_d and τ_{life}) have different physical meanings and are determined "independently". The viscoelastic terminal relaxation time of threadlike micellar solutions is determined by the faster process.

Shikata et al investigated threadlike micelles composed of a cationic surfactant (cetyltrimethyl ammonium bromide, CTAB) and an organic salt (sodium salicylate, NaSal) in aqueous solutions.[1] They observed two types of viscoelastic relaxations which are dominated by τ_d or τ_{life}, depending on the NaSal concentration. The relaxation dominated by the τ_{life} at high NaSal concentrations was studied extensively,[1-3,10,11] and it turned out that the terminal relaxation is described by the single Maxwell model, which is entirely different from the viscoelastic relaxation of general polymer systems. On the other hand, at lower NaSal concentrations, the viscoelastic spectrum is similar to non-entangled or entangled polymer

systems, depending on the surfactant and NaSal concentrations. Therefore, this viscoelastic relaxation seems to be dominated by polymer-like dynamics. However, this similarity of viscoelastic spectra is observed in the only low frequency region which corresponds to the region from the rubbery plateau to the terminal flow, because the frequency range measured by conventional rheometer is limited ($10^{-2} \leq \omega / s^{-1} \leq 10^{2}$).

Cates et al. theoretically expected that the relaxation of threadlike micelles in the high frequency region is dominated by the polymer-like dynamics. Furthermore, they expected that the dynamics of the threadlike micellar system dominated by their τ_{life} in the low frequency region also corresponded to polymer-like one in the higher frequency than $1/\tau_{life}$.[11] In order to confirm their expectation experimentally, the linear viscoelastic measurement must be carried out over a wider frequency range which is not accessible by conventional rheometers.

The laser particle tracking (LPT) method which is mentioned in Chapter IV is a powerful tool. This apparatus is able to measure high frequency viscoelasticity for aqueous solutions up to $\omega \sim 3\times10^{4}$ s^{-1}.[18] In this chapter, I report the linear viscoelasticity of threadlike micelles composed of nonionic and cationic surfactants, measured by LPT rheometry. The obtained wideband spectrum for threadlike micellar solutions is compared with viscoelastic theories for non-entangled and entangled polymer systems to confirm whether or not the dynamics of the threadlike micelles corresponds to that of polymer systems.

V-2. Experimental Section.

V-2-1. Materials.

A nonionic surfactant hexaoxyethylene tetradecyl ether ($C_{14}E_6$, Nikko Chemicals Co. Ltd) and a cationic surfactant cetyltrimethyl ammonium bromide (CTAB, Wako Pure Chemical Industries, Ltd.) were used for the following viscoelastic measurements. The latter

sample was purified by the recrystallization method with acetone/methanol, while the former sample was used without further purification. The surfactant samples were dissolved in pure water purified by a Millipore Elix system, and sodium salicylate (NaSal, Wako Pure Chemical Industries, Ltd.) was added to the aqueous CTAB solution. In this study, mass concentrations of $C_{14}E_6$, CTAB, and NaSal in aqueous solution are represented by c, c_D, and c_S, respectively. Linear viscoelastic measurements were made on $C_{14}E_6$ solutions with c = 2.0×10^{-2} – 1.0×10^{-1} g cm^{-3}, and CTAB/NaSal solutions with c_D = 7.3×10^{-3} g cm^{-3} and c_S ranging from 1.3×10^{-3} g cm^{-3} to 6.4×10^{-3} g cm^{-3}. Less than 10^{-3} wt% of polystyrene probe particles of a diameter 1.0μm (Molecular Probes, F8821) was dispersed in all the sample solutions for LPT measurements.

V-2-2. Measurements.

The LPT measurement was carried out in the manner same as that of Chapter IV. The apparatus constant was determined just before each measurement. Viscoelastic measurements for the solutions without probe particles were also carried out with a conventional rheometer (MCR301).

V-3. Results.

V-3-1. Linear Viscoelastic Spectra for Aqueous $C_{14}E_6$ Solutions.

Figure V-1 displays the complex shear moduli for aqueous $C_{14}E_6$ solutions at various concentrations c. Filled and unfilled square symbols show the storage and loss moduli G' and $G''-\omega\eta_s$ measured by the LPT method, respectively. Here, the contribution of the solvent viscosity $\eta_s = 8.9\times10^{-4}$ Pa s is subtracted from G''. The linear viscoelastic spectra are obtained up to the high frequency $\omega \sim 3\times10^4$ s^{-1}. The validity of the result by the LPT measurement is confirmed by the result obtained by a conventional rheometer in a low frequency region ($\omega \leq$

30 s^{-1}), indicated by filled and unfilled circles. This agreement indicates that a tiny quantity of probe particles do not influence the viscoelastic property. For $C_{14}E_6$ solutions with $c \leq 3.6\times10^{-2}$ g cm^{-3}, reliable G^* data are not obtained by MCR301, because the value of G^* is too low (< 10^{-1} Pa) to measure linear viscoelasticity by the conventional rheometer. In contrast, the LPT rheometry can measure low G^* up to 10^{-3} Pa. This is another advantage of the LPT rheometry, in addition to the high frequency measurement.

In Figure V-1, the all viscoelastic spectra are expressed as $G' \propto \omega^2$ and $G''-\omega\eta_s \propto \omega$ in the low frequency region. Using the data in this region, I obtained the terminal relaxation time τ_w and the excess viscosity $\eta-\eta_s$. The results are listed in the third and fourth columns of Table V-1.

The two types of spectra are observed depending on the concentration. At the low concentrations (c = 0.020, 0.030 and 0.036 g cm^{-3}), the spectra of G' do not have the rubbery plateau. This behavior is similar to non-entangled polymer solutions. On one side, at c = 0.10 g cm^{-3}, the rubbery plateau is observed in $1000 < \omega/\ s^{-1} < 2000$. The rubbery plateau indicates entanglement of the threadlike micelle chains in this frequency region. For this concentration, I obtained the rubbery plateau modulus G_N to be 130 Pa defined from the G' of an inflection point.

In the high frequency region ($\omega \geq 10^4$ s^{-1}), all solutions shows a same behavior which described power-law relaxation scaled with an exponent of 0.5 as the eq V-1.

$$G' = G'' - \omega\eta_s \sim a\omega^{0.5} \qquad \text{(V-1)}$$

The value of a in the above equation was determined for each solution (cf. the sixth column of Table V-1). This concentration independent viscoelastic behavior of the threadlike micellar solution, which has not observed by the conventional rheometry, is similar to that of polymer solutions at high frequencies. For polymer solutions, the high frequency viscoelasticity reflects the orientation relaxation of the polymer chain segment.[16,17]

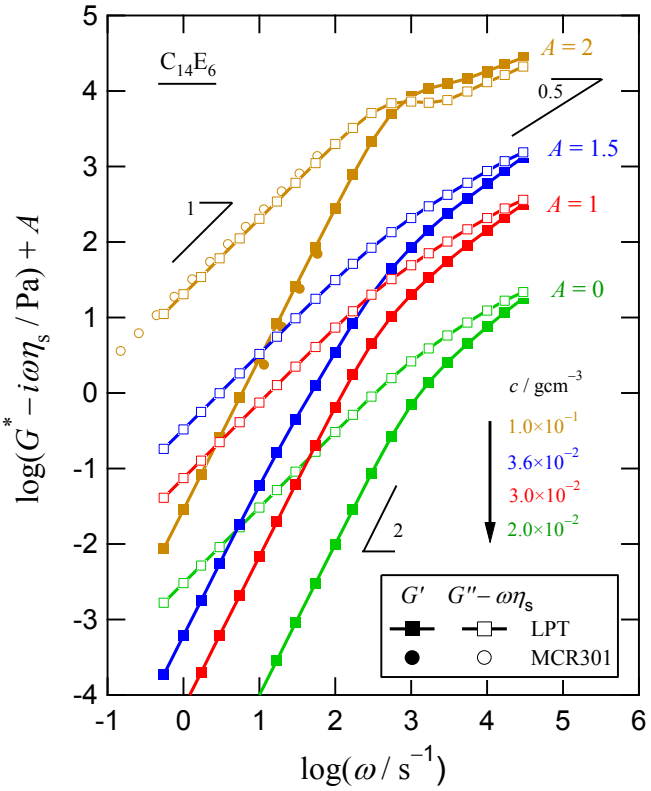

Figure V-1. Complex shear modulus G^*–i$\omega\eta_s$ measured by the LPT method for aqueous $C_{14}E_6$ solutions having various c. The filled and unfilled symbols represent G' and G''– $\omega\eta_s$, respectively. The viscous contribution of solvent $\omega\eta_s$ is reduced from G''.

Table V-1. Viscoelastic parameters estimated from the complex modulus G^*–i$\omega\eta_s$ for aqueous $C_{14}E_6$ solutions. The spectrum types are described in the next term.

c / 10^{-2} g cm^{-3}	C / 10^{-3} M	τ_w / 10^{-3} s^{-1}	$\eta - \eta_s$ / 10^{-2} Pa s	G_N / Pa	a / Pa s$^{0.5}$	Spectrum Type
10	210	1.5	19	130	1.2	(C)
3.6	75	1.8	1.1	–	0.27	(A)
3.0	63	0.94	0.80	–	0.20	(A)
2.0	42	0.36	0.33	–	0.12	(A)

V-3-2. Linear Viscoelastic Spectra for Aqueous CTAB/NaSal Solutions.

Figure V-2 shows, linear viscoelastic spectra for aqueous CTAB/NaSal solutions with c_D = 7.3 × 10^{-3} g cm^{-3} and different c_S. In the low frequency region, the terminal flow relaxation behavior is observed. I obtained the terminal relaxation time τ_w and the excess viscosity $\eta-\eta_s$ for these solutions (the third and fourth columns of Table V-2). The τ_w and $\eta-\eta_s$ increase with increasing c_S. Particularly, these values increase drastically between c_S = 1.6 and 1.9×10^{-3} g cm^{-3}. The τ_w for CTAB/NaSal solutions are longer than that of $C_{14}E_6$ solutions except that for c_S = 1.3×10^{-3} g cm^{-3}. The values of $\eta-\eta_s$ for CTAB/NaSal solutions are smaller than that of $C_{14}E_6$ solutions in $c_S \leq 1.6\times10^{-3}$ g cm^{-3}, but larger in $c_S \geq 1.9\times10^{-3}$ g cm^{-3}.

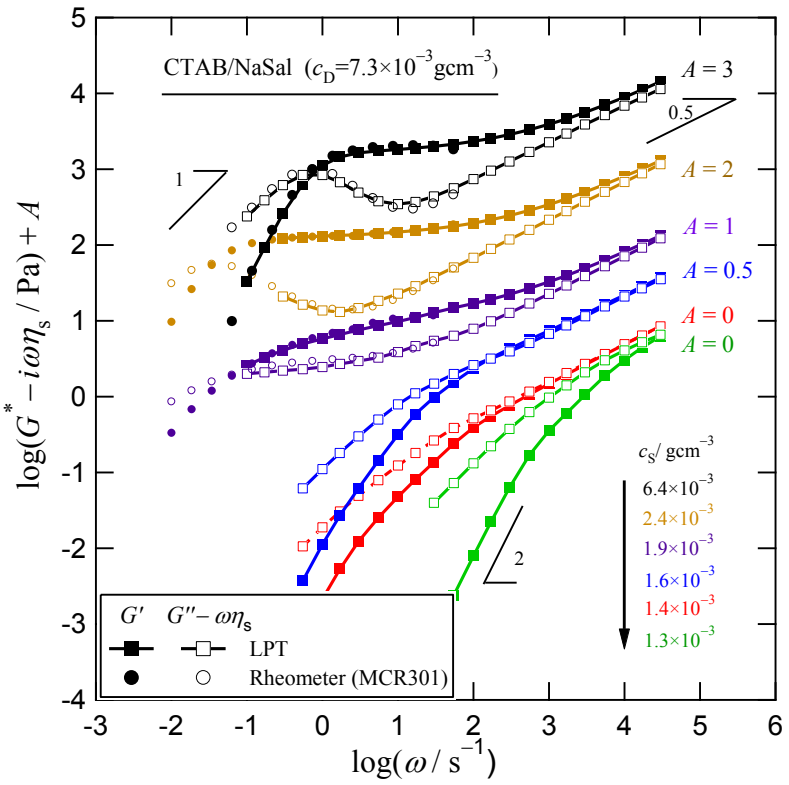

Figure V-2. Complex shear modulus G^*–i$\omega\eta_s$ measured by the LPT method for aqueous CTAB/NaSal solutions having various c_S. The filled and unfilled symbols represent G' and $G''-\omega\eta_s$, respectively. The viscous contribution of solvent $\omega\eta_s$ is reduced from G''.

Also for CTAB/NaSal solutions, the two types of spectra are observed depending on the c_S. At the low c_S (= 1.3, 1.4 and 1.6×10^{-3} g cm^{-3}), the spectra of G' do not have the rubbery plateau, which is similar behavior with non-entangled polymer solutions. On the other hand, at the high c_S (= 1.9, 2.4 and 6.4×10^{-3} g cm^{-3}), the clear rubbery plateau is observed. For this concentration, the entanglement of threadlike micelles is indicated, and I obtained the rubbery plateau modulus G_N defined from the G' of an inflection point. These values are shown in Table V-2.

Comparing the spectra having the rubbery plateau (c_S = 1.9, 2.4 and 6.4×10^{-3} g cm^{-3}) carefully, the terminal relaxation (in $\omega < 1$ s^{-1}) of $c_S = 1.9\times10^{-3}$ g cm^{-3} is distinguished from the others. At $c_S = 1.9\times10^{-3}$ g cm^{-3}, the relaxation time distribution is broad, while the other solutions having higher c_S (=2.4 and 6.4×10^{-3} g cm^{-3}) showed a sharp relaxation behavior which described by the single Maxwell model from rubbery plateau to terminal flow region.[1] The former resembles the spectrum of entangled polymer systems. Therefore the relaxation is dominated by the τ_d which is faster than the τ_{life}. On the other hand, the latter is dominated by the τ_{life} which is faster than the τ_d.

Considering above, the viscoelastic spectra is classified by three types as follows.

(A) The spectrum without the rubbery plateau. (similar to non-entangled polymers)

(B) The spectrum with the rubbery plateau and broad terminal relaxation. (similar to entangled polymers)

(C) The spectrum with the rubbery plateau and sharp terminal relaxation which described by the single Maxwell model. (not similar to polymers)

This classification was applied for also $C_{14}E_6$ solutions. The result of the classification is shown in the last column of Table V-1 and V-2. The terminal flow relaxation of (C) is dominated by the τ_{life}.

In the high frequency region ($\omega \geq 10^4$ s^{-1}), the spectra obey the power-law relaxation scaled with an exponent of 0.5 as the eq V-1. As in the case of the aqueous $C_{14}E_6$ solutions, this behavior is independent of the spectra types. The determined values of a are listed in the Table V-2.

Table V-2. Viscoelastic parameters estimated from the complex modulus G^*–i$\omega\eta_s$ for aqueous CTAB / NaSal solutions with fixed $c_D = 7.3 \times 10^{-3}$ g/cm^3 ($C_D = 0.02$ M) and different c_S.

c_S / 10^{-3} g cm^{-3}	C_S / 10^{-3} M	τ_w / 10^{-3} s^{-1}	$\eta - \eta_s$ / 10^{-2} Pa s	G_N / Pa	a / Pa s$^{0.5}$	Spectrum Type
6.4	40	1300	–	1.9	0.075	(C)
2.4	15	29000	–	1.5	0.072	(C)
1.9	12	42000	–	1.4	0.072	(B)
1.6	10	130	3.8	–	0.072	(A)
1.4	9	130	2.0	–	0.050	(A)
1.3	8	0.59	0.15	–	0.043	(A)

V-4. Discussion.

V-4-1. Non-entangled System – Type A.

For aqueous $C_{14}E_6$ solutions at $c \leq 3.6\times10^{-2}$ g cm^{-3} and aqueous CTAB/NaSal solutions at $c_S \leq 1.6\times10^{-3}$ g cm^{-3}, the shape of G^* is similar to that for non-entangled polymer solutions (the spectrum type A). The terminal relaxation time distribution in these micellar systems is broader than that of the monodisperse polystyrene solution.[17,19,20] This broadness is owing to the molar mass distribution of the threadlike micelles (cf. Chapter I).

When $\tau_d << \tau_{life}$, the viscoelasticity of threadlike micellar solutions may be identified with that of polymer solutions. In the non-entangled dilute regime, the viscoelastic behavior

of polymer solutions can be described with the Rouse-Zimm (RZ) theory.[19] Taking into account of the molar mass distribution, G^* is express as.

$$G^*_{\mathrm{RZ}} = \sum_{M=0}^{\infty}\left(x_{\mathrm{M}} \frac{cRT}{M} \sum_{p=1}^{N} \frac{\mathrm{i}\omega\tau_{\mathrm{p}}}{1+\mathrm{i}\omega\tau_{\mathrm{p}}} \right) \tag{V-2}$$

$$\tau_{\mathrm{p}} = \frac{\tau_{\mathrm{R}}}{p^{\alpha}} \tag{V-3}$$

Here, R, T, and N are the gas constant, temperature, and the number of viscoelastic segments per chain, respectively, x_{M} is the mole fraction of the component with the molar mass M, and c is the mass concentration of the micelle. The relaxation time τ_{p} is the relaxation time of the p-th normal mode and τ_{R} is the longest Rouse-Zimm relaxation time. The exponent α varies with the solvent and concentration. In the semi-dilute regime, α should be chosen to be 2 (the Rouse model) to describe experimental G^*. Furthermore, the α is the inverse of the exponent in the frequency dependence of G^* at high frequencies. For these micellar systems, the observed exponent was 0.5 (cf. eq V-1), therefore I can chose α = 2. According to the thermodynamic theory of threadlike micelles, the molar mass of the micelles follows the most probable distribution ($M_{\mathrm{w}}/M_{\mathrm{n}} = 2$), which is represented by eq V-4.[21]

$$x_{\mathrm{M}} = \frac{1}{M_{\mathrm{n}}} \exp\left(-\frac{M}{M_{\mathrm{n}}} \right) = \frac{2}{M_{\mathrm{w}}} \exp\left(-\frac{2M}{M_{\mathrm{w}}} \right) \tag{V-4}$$

Here, M_{w} and M_{n} are the weight and number average molar masses, respectively.

The eqs V-2 – V-4 describes viscoelastic spectra of polymer solution in the dilute regime. However, it is known that this theory used the true molar mass in eq. V-4 does not fit the experimental data in the semi-dilute regime. In this case, to fit the theory to experimental spectra, one must use an apparent molar mass $M_{\mathrm{w,app}}$ instead of true M_{w} in eq V-4.[22] The $M_{\mathrm{w,app}}$ is larger than the true M_{w}, depending on the concentration.

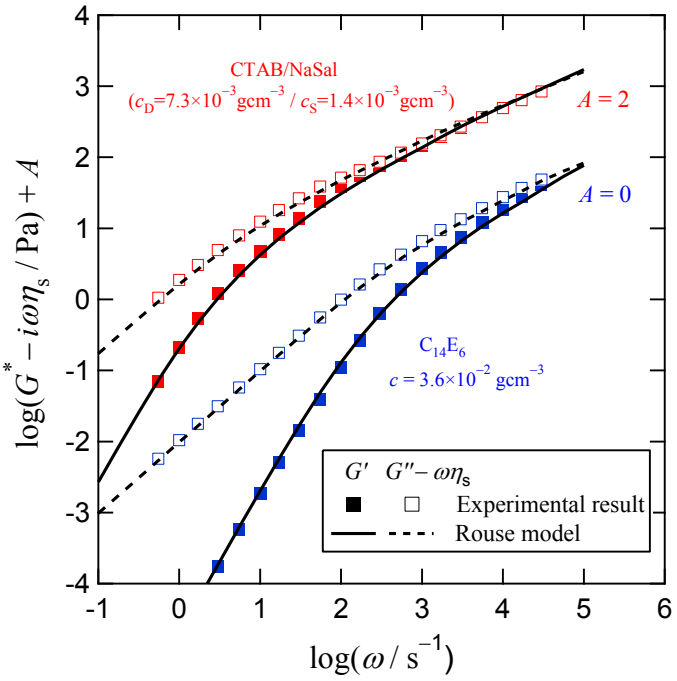

Figure V-3. Complex shear modulus G^*–i$\omega\eta_s$ measured by LPT for $C_{14}E_6$ solution; c = 3.6×10^{-2} g cm^{-3} and CTAB/NaSal solution; c_S = 1.4×10^{-3} g cm^{-3}. The solid and broken line represent G' and G''– $\omega\eta_s$ of Rouse model (eqs V-2 – V-4), respectively.

In eq V-3, τ_R can be identified with τ_w determined above from the low frequency G^* data. The concentration c for the CTAB/NaSal system is calculated on the assumption that the micelle is composed of 1:1 complex of CTA^+ and Sal^-,[2] that is, the excess Sal^- is not involved in the threadlike micelle but exist as the free Sal^- ion. Therefore $c = c_{CTA} + c_{Sal}$ when $Sal^- < CTA^+$. I use this c for the CTAB/NaSal system also in the following discussion (the calculated c is listed in Table V-3). Therefore, the free parameter in the above equations to calculate G^*_{RZ} is only the apparent molar mass $M_{w,app}$.

Figure V-3 shows results of fitting by the Rouse theory (eqs V-2– V-4) to the viscoelastic data of the two threadlike micellar solutions obtained by LPT: a $C_{14}E_6$ solution of c = 3.6×10^{-2} g cm^{-3} and a CTAB/NaSal solution of c_S = 1.4×10^{-3} g cm^{-3}. The experimental results are reproduced by the Rouse model successfully. The Rouse model was also fitted to

the experimental result for the other non-entangled threadlike micellar solutions. Values of $M_{w,app}$ chosen at the fitting with the Rouse model are summarized in Table V-3 and plotted as unfilled circles in the Figure V-4.

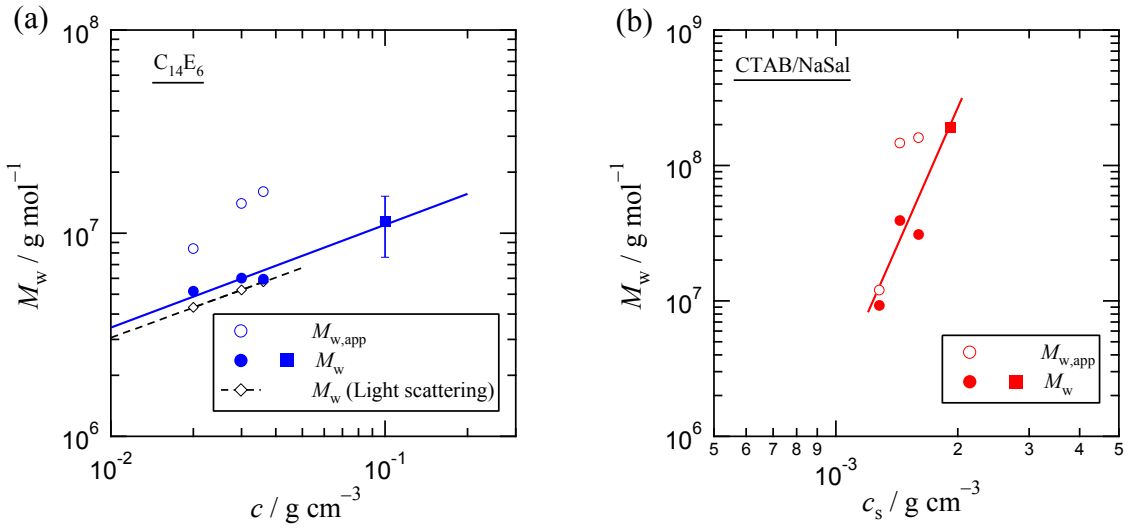

Figure V-4. Weight average molar mass for threadlike micelles of (a) $C_{14}E_6$ and (b) CTAB/NaSal solutions. The unfilled and filled circles, are respectively the $M_{w,app}$ and the corrected M_w estimated by using Rouse model for the type A spectra. The filled squares are the M_w estimated by comparison with entangled polymers. The error bar represents $4 \leq M_w/M_e \leq 8$. The unfilled diamonds in the panel (a) indicate M_w determined by Einaga et al.[23] from light scattering measurements.

A previous study[22] demonstrated that the $M_{w,app}$ determined by the linear viscoelasticity for semi-dilute tricresyl phosphate (TCP) solutions of polystyrene (PS) obeyed the following relation with the true weight average molar mass M_w, being independent of the M_w (cf. Appendix) .

$$\frac{M_{w,app}}{M_w} = 1 + 0.81\left(\frac{c}{c^*}\right)^{1.3} \qquad \text{(V-5)}$$

where c^* is the overlap concentration calculated by the following equation using the intrinsic

viscosity [η].

$$c^* = \frac{2.5}{[\eta]} \tag{V-6}$$

The intrinsic viscosity [η] at a finite concentration c may be determined using the following equation[24]

$$[\eta] = \frac{\left[2\left(\eta_{sp} - \ln\left(\eta_{sp} + 1\right)\right)\right]^{1/2}}{c} \tag{V-7}$$

where η_{sp} is the specific viscosity [= ($\eta - \eta_s$) / η_s] being calculated from $\eta - \eta_s$ listed in Table V-1and V-2.

Assuming that eqs V-5 – V-7 are applicable also to the threadlike micellar systems, I estimated the true molar mass M_w at each c from $M_{w,app}$. The results for $C_{14}E_6$ solutions are plotted in Figure V-4(a) by filled circles at $c \leq 0.036$ g/cm^3, which are close to the unfilled diamonds obtained from light scattering measurements by Einaga et al.[23] This agreement means that the Rouse model used above (eqs V-2 – V-4) is suitable to describe the viscoelastic behavior of the threadlike micellar solution. In other words, the dynamics of the threadlike micelle can be identified with that of the polymer system, for these solutions showing the type A spectrum.

The true weight average molar mass M_w was also obtained for the CTAB/NaSal micelle as a function of c_S from M_w estimated by viscoelasticity. The results of M_w as well as $M_{w,app}$ are shown in Figure V-4(b) by filled and unfilled circles, respectively. The M_w of the CTAB/NaSal micelle depends on c_S strongly.

Table V-3. Viscoelastic properties calculated by using the parameters in Table1.

Aqueous $C_{14}E_6$ solution					
c / 10^{-2} g cm^{-3}	M_e / 10^6 g mol^{-1}	$M_e c$ / 10^5 g^2 mol^{-1} cm^{-3}	$[\eta]$ / 10^2 / g^{-1} cm^3	$M_{w,app}$ / 10^7 g mol^{-1}	M_w / 10^7 g mol^{-1}
10	1.9	1.9	–	–	1.1 (= $6M_e$)
3.6	–	–	1.2	1.6	0.59
3.0	–	–	1.2	1.4	0.60
2.0	–	–	1.0	0.84	0.50
Aqueous CTAB / NaSal solution					
c_S / 10^{-3} g cm^{-3}	c (=c_{CTA}+ c_{Sal}) / 10^{-3} g cm^{-3}	M_e / 10^6 g mol^{-1}	$M_e c$ / 10^5 g^2 mol^{-1} cm^{-3}	$[\eta]$ / 10^2 / g^{-1} cm^3	$M_{w,app}$ / 10^7 g mol^{-1}	M_w / 10^7 g mol^{-1}
6.4	8.4	11	0.94	–	–	–
2.4	7.7	13	0.99	–	–	–
1.9	7.3	13	0.95	–	–	19 (=$15M_e$)
1.6	7.1	–	–	13	16	3.1
1.4	6.9	–	–	9.2	14	3.9
1.3	6.8	–	–	1.7	1.2	0.93

V-4-2. Entangled System – Types B and C.

When threadlike micellar solutions in the entanglement regime have much longer τ_{life} than the reptation relaxation time, the molar mass between the entanglements M_e can be calculated by using the rubbery plateau modulus G_N.

$$M_e = \frac{cRT}{G_N} \qquad \text{(V-8)}$$

Values of M_e determined in such a way are summarized in Table V-3. Because G_N is proportional to c^2, M_e should be inversely proportional to c. Therefore, $M_e c$ must be

independent of c, and may be identified with $M_e\rho$ at bulk of the threadlike micelle ($\equiv M_{e,bulk}\rho$), where ρ is the bulk density of the threadlike micelle. For CTAB/NaSal solutions, the M_ec is independent of c_S. On the other hand, the value of M_ec for the $C_{14}E_6$ solution with c = 0.10 gcm^{-1} is about twice as large as that of CTAB/NaSal solutions. According to Fetters et al,[25] $M_{e,bulk}$ is proportional to the square of the packing parameter p ($\propto (M_ec)^{1/2}$), which is defined by

$$p \cong d^2/l_K \qquad \text{(V-9)}$$

where, d and l_K are the cross-sectional diameter and the Kuhn segment length of the threadlike micelle, respectively. Therefore, one can expect that $d^2/l_K(M_ec)^{1/2}$ is identical for the $C_{14}E_6$ and CTAB/NaSal micelles. Einaga et al.[23]determined l_K and d for the $C_{14}E_6$ threadlike micelle to be 7.0 nm, and 2.4 nm, respectively, by light scattering, while l_K for CTAB/NaSal threadlike micelle was estimated to be 14 nm by nonlinear rheology.[3] From these literature values along with M_ec determined above, d for the CTAB/NaSal micelle was calculated to be 3.1 nm. This d value is in the reasonable order of magnitude for the CTAB/NaSal micelle, indicating that the rubbery plateau region can be described by the entanglement of threadlike micelles as ordinary polymer systems.

Figure V-5 compares G^* of the CTAB/NaSal solution of c_S = 1.9×10^{-3} g cm^{-3} (the spectrum type B) with that of bulk polystyrene (PS) with M_w = 2.5×10^5 g mol^{-1} and M_w/M_n = 1.92.[22] The viscoelastic measurement for the PS sample was carried out at temperature T = 120~180 ºC, and the spectrum of PS at the reference temperature T_r = 180 ºC was obtained by subtracting the contribution of the glass mode G_{glass} of PS[17,26], and shifting the vertical axis with G_N. In addition, the G^* of PS were shifted along the frequency axis so that the iso-friction state is achieved. The iso-frictional state can be realized by having same value of a in the power-law region, $G' = a\omega^{0.5}$. Judging from a good agreement in G^* between both systems in Figure V-5, the relaxation dynamics of the entangled threadlike micelle is very

similar to that of polymer system. According to the universal rule of the entanglement behavior in polymer systems, the terminal flow relaxation time depends on the number of entanglement points per chain, represented as M_w/M_e.[27] If no special interactions (for example hydrogen-bonding or hydrophobic interaction etc.) work between polymer chains, the molar mass dependence of τ_w can be described with eq V-8 in the iso-friction state.

$$\tau_{w,iso} \sim \left(\frac{M_w}{M_e} \right)^{3.4} \tag{V-10}$$

The agreement of the spectra of CTAB/NaSal and PS system means that the values of M_w/M_e are comparable each other. Quoting the value of M_e of PS in melt (1.7×10^4 g mol^{-1})[28], the value of M_w/M_e of this PS sample is 14.5. Therefore, M_w of CTAB/NaSal threadlike micelle was calculated using M_e (= 1.3×10^7 g mol^{-1}) which was determined by G_N. Actually, τ_w is slightly different between these systems in Figure V-5. This indicates that the value of M_w/M_e of CTAB/NaSal is slightly larger than 14.5. This error can be corrected by eq V-10. Finally, I obtained $M_w = 1.9\times10^8$ g mol^{-1} for CTAB/NaSal solution of $c_S = 1.9\times10^{-3}$ g cm^{-3} using the corrected value of M_w/M_e (=15). This result is plotted in Figure V-4. The c_S dependence of M_w is significant ($M_w \sim c_S^{6.8}$). This means that the effect of the added NaSal is very effective to grow the CTAB threadlike micelle. As the result of this c_S dependence, temporary network gel is constructed at higher c_S for aqueous CTAB/NaSal solution.

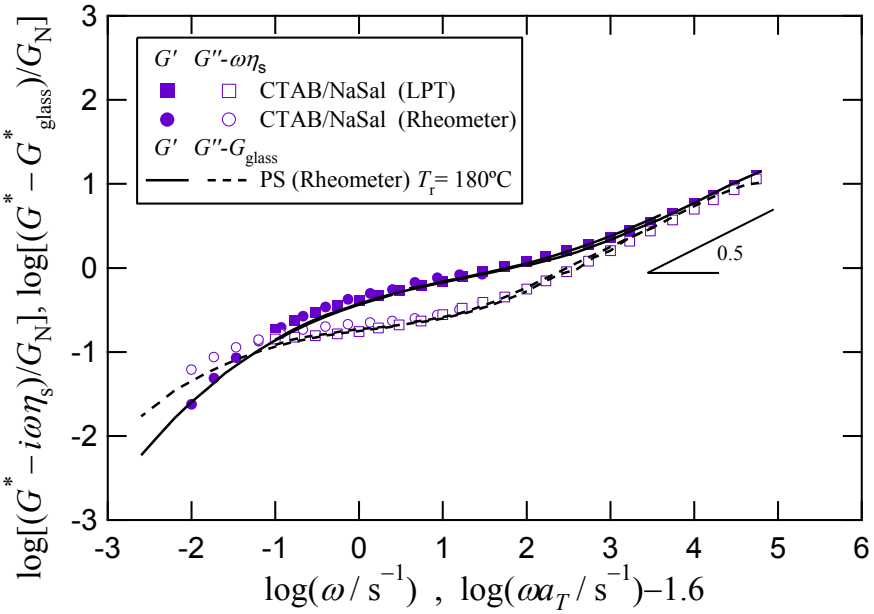

Figure V-5. Complex shear modulus G^*–i$\omega\eta_s$ for the CTAB/NaSal of c_S = 1.9×10^{-3} g cm^{-3} (filled and unfilled circles) with a comparison to G^*–G_{glass} for polystyrene (M_w = 2.5×10^5 g mol^{-1}, M_w /M_n = 1.92, solid and dotted curves).

In Figure V-6, I compares the storage modulus G' of $C_{14}E_6$ solution of c = 1.0×10^{-1} g cm^{-3} (the spectrum type C) and PS/tricresyl phosphate (TCP) solution in the same manner as in Figure V-5. According to eq V-8, M_e is changed by dilution. I measured viscoelasticity for PS/TCP solution of c = 5.8×10^{-1} and 2.8×10^{-1} g cm^{-3} at T_r = 10 ºC and 115 ºC, respectively, which has the value of M_w/M_e = 8 and 4, respectively. The spectrum of $C_{14}E_6$ solution was not agreed with these PS/TCP solutions in the terminal flow region because these the relaxation of $C_{14}E_6$ micelle is dominated by τ_{life}. Therefore, comparison of τ_w is nonsense for the solution of type C. However, in $\omega > 1/\tau_w \sim 10^3$ s^{-1}, spectra comparison may be possible. In the region of $\omega \geq 10^4$ s^{-1}, G^*–i$\omega\eta_s$ of $C_{14}E_6$ solution agrees well with G^*–G_{glass} of both PS/TCP solution. This means that the spectrum in the high ω region is independent of the value of M_w/M_e. In the case of M_w/M_e < 10, a complete rubbery plateau is not observed as Figure V-6, and G_N increases with increasing the value of M_w/M_e. Therefore, I focused the value of G' around ω =

1.5×10^{3} s^{-1} (near the arrow in Figure V-6). In this region, $C_{14}E_6$ solution has middle value of G_N between that of $c = 2.8\times10^{-1}$ and 5.6×10^{-1} g cm^{-3} of PS/TCP solution. This means that the value of M_w/M_e of $C_{14}E_6$ solution is between 4 and 8. Therefore, assuming the value of M_w/M_e of $C_{14}E_6$ solution is 6, M_w was estimated at 1.1×10^{7} g mol^{-1}. This result is plotted in Figure V-4 by a filled square with the error bar, and the square root c dependence of M_w, expected by micellar theory,[21,29] is obtained for the $C_{14}E_6$ micelle.

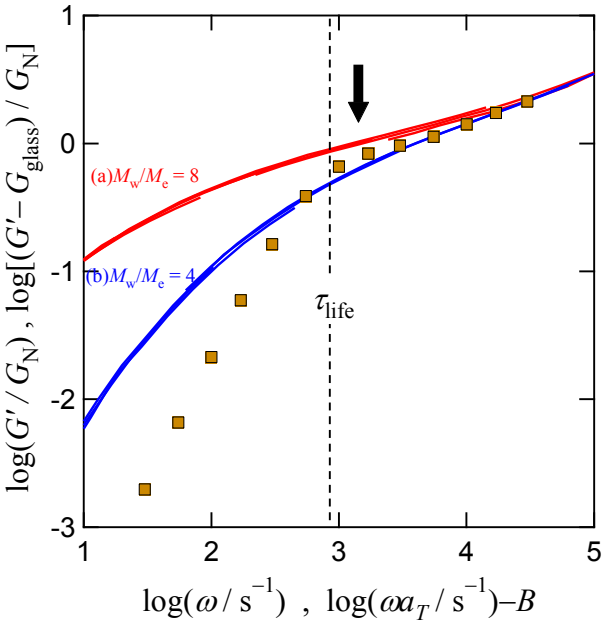

Figure V-6. Storage shear modulus G' for the $C_{14}E_6$ solution of $c = 1.0\times10^{-1}$ g cm^{-3} (filled square) with a comparison to $G' - G_{glass}$ for PS/TCP solution (a) $c = 5.6\times10^{-1}$, $B = 0.5$, $M_w/M_e = 8$, (b) 2.8×10^{-1} g cm^{-3}, $B = 2.8$, $M_w/M_e = 4$. PS is the same sample with that in ref 22.

V-4-3. Viscoelastic Behavior of High Frequencies.

At the high frequency end, G' shows a power law dependence, and the molar mass M_{seg} of the Rouse segment can be estimated from the plateau modulus G'_∞ in the high frequency region by[26]

$$M_{seg} = \frac{cRT}{G'_\infty} \qquad \text{(V-11)}$$

This M_{seg} is equal to the Kuhn segment length l_K multiplied by the molar mass per unit contour length M_L. Using the values of l_K estimated in the previous section (l_K =7.0 nm and 14 nm for the $C_{14}E_6$ and CTAB/NaSal micelles, respectively), and literature values for M_L (2.7×10^3 g mol^{-1} nm^{-1} for $C_{14}E_6$ and 8.9×10^3 g mol^{-1} nm^{-1} for CTAB/NaSal[4,23]), M_{seg} was estimated to be 1.8×10^4 and 1.2×10^5 g mol^{-1} for $C_{14}E_6$ and CTAB/NaSal micelles, respectively

For the threadlike micellar solutions examined in this study, the plateau of G' in the high frequency region was not observed due to the limitation of the frequency examined. Here, I determined the maxima of M_{seg} from the value of G' at $\omega = 3.0\times10^4$ s^{-1}for $C_{14}E_6$ and CTAB/NaSal solutions to be 8.9×10^5 g mol^{-1} and 1.3×10^6 g mol^{-1}, respectively. These results are still considerably larger than M_{seg}. Therefore, the plateau region must be higher than $\omega = 3.0\times10^4$ s^{-1}.

As already mentioned above (see eq V-1), both G' and $G'' - \omega\eta_s$ for all threadlike micelle solutions examined obey the power law with an exponent of 0.5 in the high frequency region accessible by the LPT measurement in this study ($\omega \leq 3\times10^4$ s^{-1}). The similar power law was observed also for bulk and solutions of flexible polymers, and attributed to the orientation relaxation of the sub-chain of the Rouse chain. Even if the chain is entangled, the sub-chain shows orientation relaxation because the sub-chain is much smaller than the entanglement mesh size. The same power law dependence indicates that the dynamics of the threadlike micelles is the same as that of flexible polymers. Furthermore, the c and c_S independences of this power-law behavior mean that the sub-chain of micelles never changes by the concentrations.

According to the Rouse theory,[20] the coefficient a in eq V-1 is represented as

$$a = \frac{1.11cRT}{M}\tau_R^{0.5} \qquad \text{(V-12)}$$

$$\tau_R = \frac{{l_{\mathrm{seg}}}^2 {N_{\mathrm{seg}}}^2 \zeta_{\mathrm{seg}}}{6\pi^2 k_{\mathrm{B}} T} \tag{V-13}$$

Here, k_{B} is the Boltzmann constant. l_{seg}, N_{seg}, ζ_{seg} are the Rouse segmental length, the number of the Rouse segment per chain, and the friction coefficient per Rouse segment. Combining eqs V-12 and V-13, the following equation was obtained.

$$\zeta_{\mathrm{seg}} = \frac{6}{N_{\mathrm{A}} RT}\left(\frac{\pi a M_{\mathrm{L}}}{1.11c}\right)^2 \tag{V-14}$$

According to eq V-14, ζ_{seg} was determined by experimental result of a. The results are plotted against c in Figure V-7.

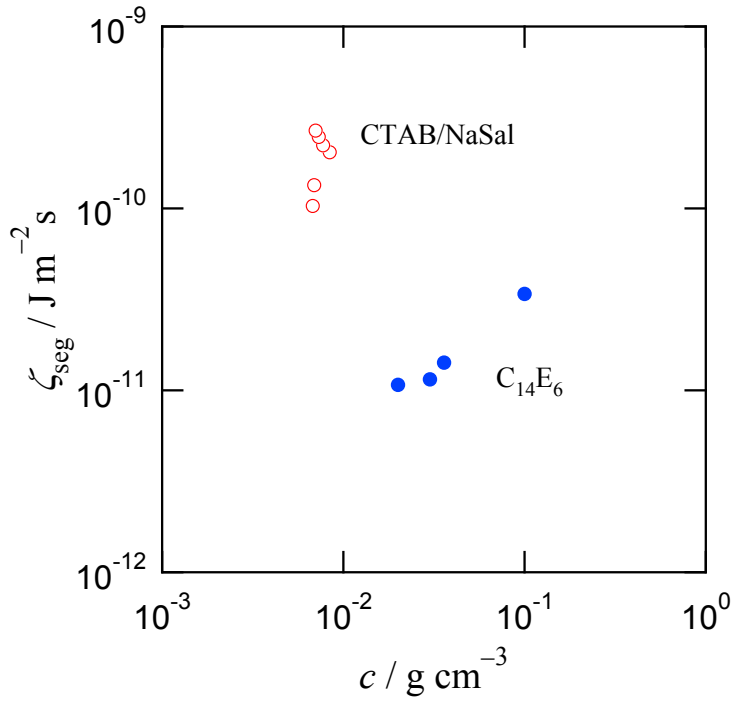

Figure V-7. Friction coefficient ζ_{seg} determined by experimental result of a via eq V-14 for $C_{14}E_6$ and CTAB/NaSal solutions.

The experimental ζ_{seg} values for the CTAB/NaSal micelle are larger than those for the $C_{14}E_6$ micelle. This may be owing to the larger values of l_{K} and d for the Rouse segment

of the CTAB/NaSal micelle, mentioned above. For the $C_{14}E_6$ micelle, the experimental ζ_{seg} increases with the concentration in Figure V-7. This may be caused by the screening effect of the intra-micellar hydrodynamic interaction, which becomes more important at higher c. However, since eq V-14 was derived from the Rouse theory, not considering the intra-micellar hydrodynamic interaction, the quantitative discussion should not be made on the c dependence of ζ_{seg} in Figure V-7.

V-5. Conclusion.

I performed linear viscoelastic measurements of threadlike micellar solutions composed of nonionic ($C_{14}E_6$) and cationic (CTAB/NaSal) surfactants by LPT rheometry. The viscoelastic spectra were successfully obtained in a wideband frequency region, $10^{-1} \leq \omega / \mathrm{s}^{-1} \leq 3\times10^{4}$.

For the low c and c_S solutions ($c \leq 3.6\times10^{-2}$ g cm^{-3} of $C_{14}E_6$ solutions and $c_S \leq 1.6\times10^{-3}$ g cm^{-3} of CTAB/NaSal solutions), non-entangled behavior was observed (the spectrum type A). The molar mass of the threadlike micelle was determined by using the Rouse model having the most probable distribution of the molar mass. The determined molar mass agreed with the result of the light scattering measurement, after correction of the finite concentration effect.

For the high c and c_S solutions ($c = 1.0\times10^{-1}$ g cm^{-3} of $C_{14}E_6$ solutions and $c_S \geq 1.9\times10^{-3}$ g cm^{-3} of CTAB/NaSal solutions), rubbery plateau region was observed in the higher frequency region than $1/\tau_{life}$. The viscoelastic behavior of these entangled solutions was classified into two types B and C. On one hand, the type B showed a broad terminal relaxation time distribution, and can be identified with the viscoelastic behavior of entangled polymer systems. On the other hand, the type C had a sharp terminal relaxation time distribution due to τ_{life}, but the spectrum higher than $1/\tau_{life}$ obeyed the polymer-like dynamics.

In the high frequency region, all solutions showed same behavior which described power-law relaxation scaled with an exponent of 0.5, being independent of the spectrum types. This concentration independence of the high frequency viscoelastic behavior of threadlike micellar solution was newly found by the LPT measurement in this study. This behavior reflects the orientation relaxation of segment of threadlike micellar chain.

Summarizing above, it was demonstrated that the dynamics of threadlike micelles is identical with that of polymer systems over the wide frequency region except the longer time region of type C.

Appendix.

Concentration dependence of the Apparent Molar Mass in Semi-dilute Regime.

Recent studies of G^* for polymer solution in semi-dilute regime can be described with the RZ theory if the additional slow mode G^*_{slow} is considered to include the effect of the inter-chain interaction.

$$G^* - G^*_{\text{glass}} = G^*_{\text{RZ}} + G^*_{\text{slow}} \qquad \text{(V-A1)}$$

For polymers having narrow molecular weight distribution in good solvents, the slow term can be described with the single Maxwell relaxation modulus.[31] Marruci et al.[32] attributed the slow term to the anisotropic diffusion of chain. For the case of polymers having most probable molar mass distribution, G^*_{slow} cannot be described with the single Maxwell relaxation modulus and a broad distribution of relaxation times is necessary for the better description as shown in Figure V-A1. As a result, G^* can be described with the RZ theory considering the molar mass distribution with the apparently larger molar mass $M_{\text{w,app}}$.[22]

$$G^* - G^*_{\text{glass}} = G^*_{\text{RZ}}\left(M_{\text{w}}\right) + G^*_{\text{slow}} \cong G^*_{\text{RZ}}\left(M_{\text{w,app}}\right) \qquad \text{(V-A2)}$$

The concentration dependence of the ratio $M_{\text{w,app}}/M_{\text{w}}$ for two PS solutions is shown in Figure V-A2. The empirical relationship between M_{w} and $M_{\text{w,app}}$ can be written as eq V-5 with

independent of molar mass of PS.[22] Eq V-5 is applicable up to $c/c^* \sim 10$.

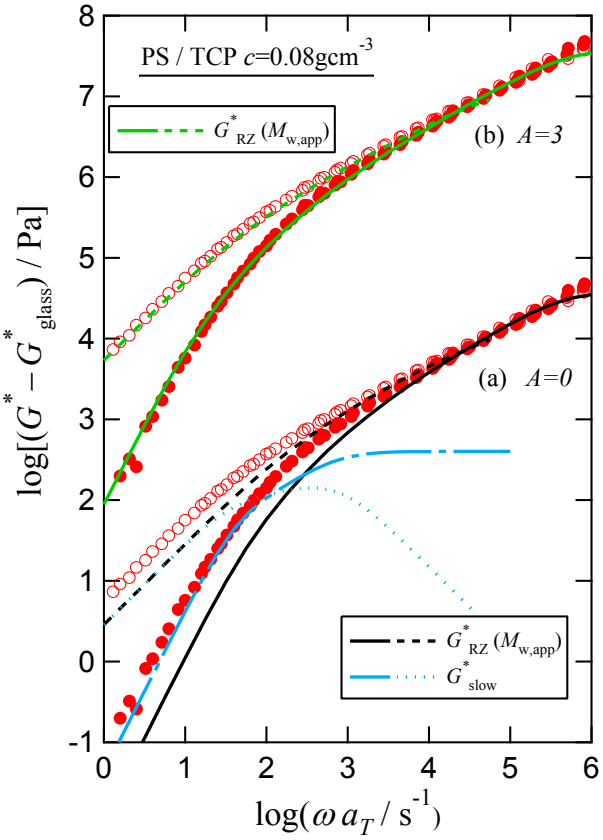

Figure V-A1. Complex modulus for PS/TCP solution in $c = 8.0\times10^{-2}$ g cm^{-3}. The PS is same sample in ref 22. Circles represent Experimental data of G^* subtracted the glassy mode ($G^*–G^*_{\mathrm{Glass}}$). This data was obtained by conventional rheometer (ARES-G2) at $T_r = 10$ ºC.

In this study, the true molar mass M_w of threadlike micelle was calculated using estimated $M_{w,app}$ and eq V-5. To use eq V-5, the $[\eta]$ value is necessary to calculate c^*. $[\eta]$ is usually determined by the extrapolation to zero concentration c with the Huggins and Fuoss–Mead plots. However, this procedure cannot be applicable to the threadlike micelles because the length of micelles varies with the concentration. Einaga et al estimated intrinsic viscosity of thread-like micelles formed by polyoxyethylene alkyl ether, C_iE_j in the finite concentration regime with using eq V-7 which is sometimes called as the Solomon-Ciuta

equation.[33] In a previous study, the reliability was examined of eq V-7 and found that this equation provide a good estimate of $[\eta]$ up to $c/c^* \sim 2$ for the case of good solvents.[24] Unfortunately, $[\eta]$ value of $C_{14}E_6$ was not reported although $[\eta]$ values of other various C_iE_j were reported. In this study, I estimated $[\eta]$ with using the viscosities in Table V-1 and V-2.

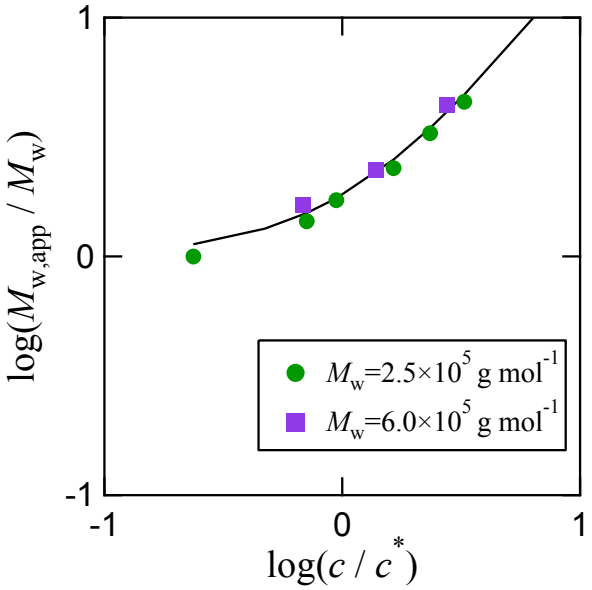

Figure V-A2. Concentration dependence of $M_{w,app}/M_w$. The molar mass of polystyrene was (1) $M_w = 2.5\times10^5$ g mol^{-1}, $M_w / M_n = 1.9$, (2) $M_w = 6.0\times10^5$ g mol^{-1}, $M_w / M_n = 1.8$. The approximate curve is represented by eq. V-5.

References.

1) Shikata, T.; Hirata, H.; Kotaka, T. *Langmuir*. **1987**, *3*, 1081.

2) Shikata, T.; Hirata, H.; Kotaka, T. *Langmuir*. **1988**, *4*, 354.

3) Inoue, T.; Inoue, Y.; Watanabe, H. *Langmuir*. **2005**, *21*, 1201.

4) Shikata, T.; Dahman, S. J.; Pearson, D. S. *Langmuir*. **1994**, *10*, 3470.

5) Takeda, M.; Kusano, T.; Matsunaga, T.; Endo, H. Shibayama, M. Shikata, T. *Langmuir*. **2011**, *27*, 1731.

6) Berret, J. F.; Appell, J.; Porte, G. *Langmuir*. **1993**, *9*, 2851.

7) Khatory, A.; Kern, F.; Lequeux, F.; Appell, J.; Porte, G.; Morie, N.; Ott, A.; Urbach, W. *Langmuir*. **1993**, *9*, 933.

8) Nakamura, K.; Shikata, T. *Macromolecules*. **2003**, *36*, 9698.

9) Cappelaere, E.; Cressely, R. *Rheol. Acta*, **2000**,*39*, 346.

10) Berret, J. F. *Langmuir*. **1997**, *13*, 2227.

11) Cates, M. E. *Macromolecules*. **1987**, *20*, 2289.

12) Cates, M. E.; Candau, S. J. *J. Phys.; Condens. Matter*. **1990**, *2*, 6869.

13) Candau, S. J.; Hirsch, E.; Zana, R.; Delsanti, M. *Langmuir*. **1989**, *5*, 1225.

14) Rouse, P. E. *J. Chem. Phys.* **1953**, *21*, 1272.

15) Zimm,B. H. *J. Chem. Phys.* **1956**, *24*, 269.

16) Doi, M.; Edwards, S. F. *The Theory of Polymer Dynamics*; Oxford Univ. Press: Oxford. 1986.

17) Ferry, J. D. *Viscoelastic Properties of Polymers*, 3rd ed.; Wiley: New York, 1980.

18) Morishima, K.; Inoue, T. *Nihon Reoroji gakkaishi*. **2010**, *38*, 195.

19) Osaki, K. *Nihon Reoroji gakkaishi*. **2002**, *30*, 165.

20) Osaki, K.; Inoue, T.; Uematsu, T. *J. Polym. Sci. B.; Polym. Phys.* **2000**, *38*, 3271.

21) Israelachivili, J. N. *Intermolecular and Surface Forces*, 2nd ed.; Academic Press: London, 1991.

22) Morishima, K.; Inoue, T. *Nihon Reoroji gakkaishi*. **2013**, *41*, 151.

23) Yoshimura, S.; Shirai, S.; Einaga, Y. *J. Phys. Chem. B.* **2004**, *108*, 15477.

24) Inoue, T.; Oba, N.; Urakawa, O. *Nihon Reoroji gakkaishi*. **2014**, *42*, 261.

25) Fetters, L. J.; Lohse, D. J.; Graessley, W. W. *J. Polym. Sci. B.; Polym. Phys.* **1999**, *37*, 1023.

26) Inoue, T.; Uematsu, T.; Osaki, K. *Macromolecules*. **2002**, *35*, 820.

27) Osaki. K.; Takatori, E.; Tsunashima, Y.; Kurata, M. *Macromolecules*. **1987**, *20*, 525.

28) Fetters, L. J.; Lohse, D. J.; Richter, D.; Witten, T. A.; Zirkel, A. *Macromolecules*. **1994**, *27*, 4639.

29) Sato, T. *Langmuir*. **2004**, *20*, 1095.

30) Yamakawa, H. *Helical Wormlike Chain in Polymer Solutions*, Springer-Verlag, Berlin and Heidelberg. 1997.

31) Osaki, K.; Inoue, T.; Uematsu, T. *J. Polym. Sci. B.; Polym. Phys.* **2001**, *39*, 211.

32) Marrucci, G.; Ianniruberto, G. *Chem. Eng. Sci*. **2001**, *56*, 5539.

33) Shirai, S.; Yoshimura, S.; Einaga, Y. *Polym. J*. **2006**, *38*, 37.

Chapter VI.

Summary

In this thesis, I developed methodology for characterizing structures and dynamics of various micelles. The first half of this thesis (Chapter II and III) dealt with the hydrophobe-uptake spherical and flower micelles, and the second half (Chapter IV and V) treated the dynamics of threadlike micelles over a wide frequency range.

In Chapter II, I characterized 1-dodecanol (DOH)-uptake spherical micelles composed of low molar mass surfactants, dodecylpyridinium chloride (DPC) and sodium dodecylsulfate (SDS), near the critical micelle concentration (CMC) by the combination of static and dynamic light scattering (SLS and DLS). The strong scattering due to the coexistence of huge colloidal particles of DOH near the CMC was eliminated from SLS and DLS data to characterize the structure and association-dissociation equilibrium behavior of the major DOH-uptake spherical micelles. The concentration dependence of the scattering intensity was described by the theory of association-dissociation equilibrium, and it turned out that DOH added to the solution was included in the hydrophobic core of the spherical micelle.

In Chapter III, I investigated the structure of the DOH-uptake micelle composed of the alternating amphiphilic copolymer of sodium maleate and dodecyl vinyl ether (MAL/C12) in an aqueous Borax solution, by combining SLS, DLS, and small angle X-ray scattering (SAXS). To explain all the scattering data consistently, I proposed the modified flower necklace model of which unit flower has an intermingled domain between the core and coronal domains. The comparison of this model with experimental SAXS and DLS data demonstrated that added DOH was included mostly in the intermingled domain and the number of unit flower micelles increased with increasing the DOH content. The micelle of MAL/C12 could include much more DOH than the spherical micelles of low molar mass

surfactants, SDS and DPC. This may be due to that the spherical micelles of SDS and DPC do not possess the intermingled domain unlike the MAL/C12 micelle.

Chapter IV dealt with a new method of a wideband viscoelastic measurement for aqueous micellar solutions. The apparatus for laser particle tracking (LPT) rheometry was constructed using inversed microscope and Nd:YAG laser. The power spectrum density (PSD) was obtained by using the displacement of a probe particle embedded in a sample solution. I calibrated the apparatus by fitting the experimental PSD for standard viscose liquids to the theoretical one which was calculated from the Langevin equation including the laser fluctuation contribution. The reliability of the apparatus was checked by comparing viscoelastic modulus obtained for a viscoelastic solution by this apparatus with that obtained by a conventional rheometer and also from birefringence at a lower frequency region.

In Chapter V, viscoelastic spectra for threadlike micellar solutions of hexaoxyethylene tetradecyl ether ($C_{14}E_6$) and of the cetyltrimethyl ammonium bromide/sodium salicylate mixture (CTAB/NaSal) were obtained by using the above LPT apparatus over a wide frequency range ($10^{-1} \leq \omega / \mathrm{s}^{-1} \leq 3\times10^{4}$). The wideband linear viscoelastic spectra obtained for different $C_{14}E_6$ and NaSal concentrations were classified into the following three relaxation types. Type A is similar to the spectrum of the non-entangle polymer system, type B similar to that of the entangle polymer system, and type C has a single Maxwell relaxation at a low frequency region.

The spectra of types A and B as well as of type C in a high frequency region were described by the polymeric viscoelastic theories of the Rouse model and the tube model. Comparing those spectra with the polymer theories, I estimated the molar mass of threadlike micelles for all types. The molar mass of the $C_{14}E_6$ threadlike micelle was favorably compared with the result of light scattering measurement. In the high frequency region, spectra of all types showed a common power-law relaxation, which reflects the orientation

relaxation of the viscoelastic segment of the threadlike micelle. Summarizing above, it was found that the dynamics of threadlike micelles is identical with that of polymer systems over the wide frequency region except the longer time region of type C.

List of Publications:

The contents of this thesis have been published or will be published in the following papers:

1) "An Apparatus for Dynamic Viscoelasticity Measurement Using Laser Particle Tracking".
   K, Morishima.; T, Inoue. *Nihon Reoroji Gakkaishi*. **2010**, *38*, 195-200.

2) "Light Scattering Study of Hydrophobe-Uptake Micellization of a Cationic Surfactant".
   K, Morishima.; T, Sato. *Langmuir*. **2014**, *30*, 11513-11519.

3) "Structure of Hydrophobe-Uptake Micelles Composed of Amphiphilic Alternating Copolymer in Aqueous Solution".
   K, Morishima.; T, Sato. in preparation for publication.

4) "High Frequency Viscoelastic Measurements of Threadlike Micelles Composed of Nonionic and Cationic Surfactants in Aqueous Solutions".
   K, Morishima.; T, Inoue; T, Sato. in preparation for publication.

Related Paper

5) "Linear Viscoelasticity of Polystyrene Solution Having a Wide Molar Mass Distribution around the Coil Overlapping Concentration".
   K, Morishima.; T, Inoue. *Nihon Reoroji Gakkaishi*. **2013**, *41*, 151-156.